

ABSTRACT

GAO, MING. Self-Assembled Three-Dimensional Nanoelectronics Systems with Neuromorphic Network Architectures (Under the direction of Dr. Thomas H. LaBean).

In recent years, biological brains have inspired development of neuromorphic computing with hardware architectures that mimic information processing structures of biological neural networks. Neuromorphic architectures have shown excellent capabilities in parallel computation and solving complex tasks and are seen as a next generation approach to the traditional von Neumann architecture. Nanowire networks, with memristive or other nonlinear electrical behaviors, are promising candidates for neuromorphic computing applications. At the same time, molecular self-assembly has been developed for fabrication of complex materials. Among them, DNA hydrogels are known for their simple fabrication process and ability to tailor specific architectures with desirable properties.

In this project, we built two-dimensional (2D) and three-dimensional (3D) nanowire networks inspired by neuromorphic architectures. We explored the synthesis, deposition, surface modification, and characterization of silver nanowires (AgNWs), and studied the integration of 3D AgNW networks in polymeric matrices. Beyond that, we applied self-assembly techniques as novel fabrication methods to organize 3D nanocircuits. We engineered, built, and characterized a variety of pure DNA hydrogels and DNA hydrogel/nanomaterial composites using carbon nanotubes and gold nanoparticles-based crosslinkers. We demonstrated the ability of hydrogel systems to self-assemble 3D percolating networks that exhibit interesting nonlinear electrical properties. We also demonstrated the tuning of viscoelasticity of hydrogel-based composites. Finally, we present potential applications and implications of this project in nanoelectronics and processing methods.

© Copyright 2021 by Ming Gao

All Rights Reserved

Self-Assembled Three-Dimensional Nanoelectronics Systems with Neuromorphic Network
Architectures

by
Ming Gao

A dissertation submitted to the Graduate Faculty of
North Carolina State University
in partial fulfillment of the
requirements for the degree of
Doctor of Philosophy

Materials Science and Engineering

Raleigh, North Carolina
2021

APPROVED BY:

Dr. Thomas H. LaBean
Chair of Advisory Committee

Dr. Joseph B. Tracy

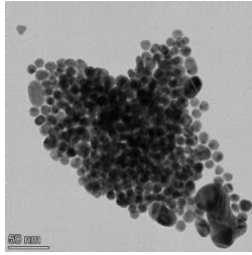
Dr. Lewis Reynolds

Dr. Lilian C. Hsiao

DEDICATION

To my parents and grandparents for their unconditional love and support.

To Endling the tabby, who has a heart of gold and brings me unparalleled joy and companionship.



BIOGRAPHY

Ming Gao was born in Liaoning, China in 1993. After completing the International Baccalaureate Diploma Program at Shanghai Pinghe School in 2012, Ming moved to the U.S. to attend the University of Minnesota, Twin Cities. During her undergraduate studies, she worked as a Research Assistant at the Soft Matter Laboratory under the guidance of Dr. Xiang Cheng. In May 2017, Ming graduated as the valedictorian of her class with a Bachelor of Materials Science and Engineering and two minors in Astrophysics and Leadership.

In the same year, Ming entered the Ph.D. program in Materials Science and Engineering at North Carolina State University. She joined the laboratory of Dr. Thomas LaBean and began her doctoral research. In May 2020, Ming obtained a Graduate Certificate in Technology Entrepreneurship and Commercialization. In Oct. 2020, she passed her preliminary defense and became a Ph.D. Candidate.

At her free time, Ming enjoys hiking and backpacking, playing the piano, handcrafting, traveling, long-distance running, and spending time with her cat, Endling.

ACKNOWLEDGMENTS

First and foremost, I am extremely grateful to Dr. Thomas LaBean for being an amazing advisor and supervisor. I am very thankful for his continuous support and mentorship, and the extra mile he would walk to ensure his graduate students have a wonderful experience during the challenging Ph.D. program. I would also like to thank my advisory committee members Drs. Joseph Tracy, Lewis Reynolds, and Lilian Hsiao for all their help and advice with this study. I am also grateful to have each of the current and former members of the LaBean research group, who have provided me invaluable help and insights on my projects. I especially would like to express my appreciation for Nikolay Frick, Dr. Abhichart Krissanaprasit, and Mahshid Hosseini. My gratitude extends to the Hsiao research group for sharing their instruments and resources, and the Finkelstein group and Moradi group for collaboration on projects.

I would also like to thank members and staffs of several NC State departments and facilities including but not limited to the Department of Materials Science and Engineering, Analytical Instrumentation Facility, Office of Research Commercialization, Jenkins MBA, NC State Libraries, NC State Wellness and Recreation, Student Health Services, Crafts Center, NC State Police, and Student Organizations. Last but not least, I appreciate all my family, friends, and mentors for believing in me and supporting me.

TABLE OF CONTENTS

LIST OF TABLES	vii
LIST OF FIGURES	viii
Chapter 1: Introduction and Project Overview	1
1.1 Vision and Inspiration	1
1.2 Background Dissertation Scope	5
1.3 Current Challenges and Opportunities	7
1.4 Dissertation Scope	9
1.4.1 Project Overview and Research Implications	9
1.4.2 Research Approaches and Objectives	10
Bibliography	14
Chapter 2: Silver Nanowire Synthesis and Characterization	19
2.1 Introduction and Background	19
2.1.1 Background	19
2.1.2 Silver Nanowire Fabrication	19
2.1.3 Project Overview	21
2.2 Silver Nanowire Synthesis	22
2.2.1 Influence of Reaction Temperature, Reaction Time, PVP Ratio, and Stirring Condition	22
2.2.2 Protocol for Silver Nanowire Synthesis with a Hot Plate	28
2.2.3 Protocol for Silver Nanowire Synthesis with a Thermostatic Bath	32
2.3 Characterization	32
2.3.1 Chemical Analysis	32
2.3.2 Microscope Imaging	34
2.4 Conclusions and Future Directions	38
Bibliography	40
Chapter 3: Two-Dimensional Silver Nanowire Networks on Glass Substrate	43
3.1 Introduction and Background	43
3.1.1 Two-Dimensional Silver Nanowire-Based Films	43
3.1.2 Fabrication Methods for Silver Nanowire-Based Films	43
3.1.3 Project Overview	45
3.2 Surface Modifications of Silver Nanowires	45
3.2.1 Silver Nanowire with and without PVP Coatings	45
3.2.2 Ag-Ag ₂ S Core-Shell Nanowires	46
3.3 Fabrication of Two-Dimensional Silver Nanowire Networks	48
3.4 Electrical Characterization	50
3.4.1 IV Curve Measurements of Silver Nanowire with and without PVP Coatings	50
3.4.2 IV Curve Measurements of Silver Nanowire and Silver-Silver Sulfide Core- Shell Nanowires	54
3.5 Conclusions and Future Directions	56
Bibliography	58

Chapter 4: Fabrication and Characterization of Nanowire-Polymer Composites	62
4.1 Introduction and Background	62
4.1.1 Background	62
4.1.2 Fabrication of Polymer-Based Composites	62
4.1.3 Project Overview	63
4.2 Three-Dimensional Nanowire-Polymer Composites	65
4.2.1 Nanowire Dispersion	65
4.2.2 Composite Integration.....	66
4.3 Method for Composite Fabrication	69
4.4 Characterization	71
4.5 Electrical Measurement	78
4.6 Conclusions and Future Directions	81
Bibliography	83
Chapter 5: DNA Hydrogel-Based Composites with Self-Assembled Percolating Networks	85
5.1 Introduction and Background	85
5.1.1 Background	85
5.1.2 DNA-Based Hydrogels	85
5.1.3 Carbon Nanotubes and Gold Nanoparticles.....	86
5.1.4 Project Overview	87
5.2 Design and Construction of DNA Hydrogels and DNA-Based Composites.....	89
5.2.1 Sequence Design of DNA Crosslinkers and Spacers.....	89
5.2.2 DNA-CNT Conjugates.....	92
5.2.3 DNA-AuNP Conjugates.....	94
5.2.4 Construction of Pure DNA Hydrogels and DNA Hydrogel Composites	96
5.3 Characterization of Conjugates and Hydrogels	98
5.4 Mechanical Studies	102
5.4.1 Rheological Properties of DNA Hydrogels	102
5.4.2 Microrheological Properties of DNA Hydrogels.....	109
5.5 Electrical Studies	114
5.6 Conclusions and Future Directions	118
Bibliography	121

LIST OF TABLES

Table 2.1	Variables and values examined in the parametric study of AgNW synthesis	24
Table 2.2	Reagent specifications for AgNW synthesis with a thermostatic bath	32
Table 4.1	Composite combinations—dispersed phase explorations in different continuous phases	64
Table 5.1	Sequences of ssDNA for the preparation of crosslinkers and spacers	90
Table 5.2	Concentrations and ratios of crosslinkers and spacers to prepare for hydrogels	96

LIST OF FIGURES

Figure 1.1	von Neumann architecture versus neuromorphic architecture (Adapted from Valle, 2018)	2
Figure 1.2	Schematic illustration of reservoir computing (Adapted from Duport, 2016)	3
Figure 1.3	IV curve characterization of Ag-Ag ₂ S core-shell nanoparticles, showing hard switching with pinched hysteresis loop (Adapted from Hadiyawarman, 2021)	4
Figure 1.4	Mechanisms of DNA hydrogel formation by (a) hybridization, (b) enzyme catalyzed assembly, and (c) entanglement of long DNA chains via polymerase chain amplification (Adapted from Gačanin, 2020)	7
Figure 1.5	Flowchart of the project	11
Figure 2.1	Absorption spectra of AgNW suspension in ethanol for two nanowire samples with either 50 or 200 nm average diameter (Adapted from Andres, 2015).....	20
Figure 2.2	Averaged AgNW lengths produced with different reaction temperature and time	28
Figure 2.3	Photos of AgNW synthesis setups with (a) hot plate approach and (b) thermostatic bath approach	29
Figure 2.4	AgNWs stored in ethanol after purification	31
Figure 2.5	Absorption spectrum of AgNWs after synthesis and purification, showing an absorption peak at ~390 nm.....	33
Figure 2.6	(a) An SEM image of AgNWs and its corresponding EDS element maps, and (b) EDS spectrum of the detected area	34
Figure 2.7	Optical images of AgNWs taken by (a) AmScope microscope with MU1000 digital camera at 40X magnification, showing synthesized long AgNWs and (b) Nikon Optiphot at 20X magnification showing short AgNWs	35
Figure 2.8	(a) An SEM image of AgNWs. Scale bar is 10 μ m. (b) A TEM image of AgNWs for diameter measurements. Scale bar is 200 nm.....	36
Figure 2.9	Using AgNWs synthesized at 170°C for 25 min for example, (a) the length distribution of AgNWs is measured by ImageJ from SEM images, and (b) the diameter distribution of AgNWs is measured from TEM images.	36
Figure 2.10	Stitched images of a single AgNW (a) from 10 TEM images and (b) from 5 TEM images for curvature calculation	38
Figure 3.1	(a) Scanning electron microscopy (SEM) and (b) transmission electron microscopy (TEM) images of Ag ₂ S NWs. Scale bars are 10 μ m and 1 μ m, respectively. Figure 3.1 (b) was taken by Mahshid Hosseini, used with permission	48
Figure 3.2	(a) EDS element mapping of Ag ₂ S NWs, and (b) EDS spectrum of the detected area	48
Figure 3.3	The spin coating setup	50
Figure 3.4	IV curve measurements of AgNW networks built by long AgNWs (a-b) with and (c-d) without PVP coatings. (a, c) were recorded with voltage pulses at ± 5 V, while (b, d) were recorded with pulses at ± 10 V. Legends show the pulse number	52
Figure 3.5	IV curve measurements of AgNW networks built by short AgNWs (a-b) with and (c-d) without PVP coatings. (a-b) The networks were deposited from	

	solution with the concentration of 1 mg/mL and (c-d) was from solution with concentration of 0.75 mg/mL. (a, c) were recorded with voltage pulses at ± 5 V, while (b, d) were recorded with pulses at ± 10 V. Legends show the pulse number	54
Figure 3.6	IV curves of a 2D network built by AgNWs and Ag ₂ S NWs. Legend shows the pulse number	55
Figure 4.1	(a) The mixture of dissolved polycaprolactone in chloroform and AgNW solution. Photo was taken before the solvents evaporated. (b) Final AgNW-polycaprolactone composite connected to an electrode array. 4 vol% AgNWs were embedded in the polycaprolactone matrix. (c) A AgNW-Ag ₂ S NW-polycaprolactone composite attached to an electrode array. 0.4 vol% AgNWs and 4 vol% Ag ₂ S NW were embedded in the polycaprolactone matrix.....	71
Figure 4.2	(a) SEM and (b) TEM images of Ag ₂ S NW. Scale bars are 10 μ m and 1 μ m, respectively. (c) Optimal microscopy and (d) SEM images of silver dendrites. Scale bars are 400 μ m and 10 μ m, respectively. (e) SEM image of the combination of AgNWs and Ag ₂ S NWs. Scale bar is 10 μ m.....	72
Figure 4.3	SEM images of the surfaces of (a) AgNW-polycaprolactone composite and (b) AgNW-nanocellulose composite. Scale bars are 20 μ m and 5 μ m, respectively. (c-d) SEM images of the cutting of AgNW-Ag ₂ S NW-polycaprolactone composite, showing long AgNWs and short Ag ₂ S NW network. Scale bars are 10 μ m.....	74
Figure 4.4	(a) Reconstructed 3D composite structure from micro-CT scans and (b) a nano-CT scan (118 μ m by 118 μ m) of a AgNW-Ag ₂ S NW-polycaprolactone composite.....	76
Figure 4.5	SEM images of a cryo-fractured hydrogel composite, showing AgNWs embedded in the agarose networks. Scale bars are 1 μ m	78
Figure 4.6	(a) IV curve measurements of a AgNW-Ag ₂ S NW-polycaprolactone sample comprising of 0.4 vol% AgNWs and 4 vol% Ag ₂ S NWs, measured with an electrode array shown in Figure 4.1 (c). Legend shows pulse number. (b) The corresponding triangle pulses scanning curves	80
Figure 4.7	IV curve measurements of a AgNW-Ag ₂ S NW-polycaprolactone sample comprising of 0.5 vol% AgNWs and 5 vol% Ag ₂ S NWs	80
Figure 5.1	Schematic illustrations of DNA-based hydrogel formation. (a-d) Various types of crosslinkers: (a) Y-shaped DNA tile, (b) X-shaped DNA tile, (c) DNA-CNT conjugate, (d) DNA-AuNP conjugate; (e) Spacers of different lengths: Ss, Sm, and Sl; (f) Pure DNA hydrogel constructed by combining Y-shaped or X-shaped DNA tiles with spacers, (g-h) DNA hydrogel composites: (g) DNA-CNT hydrogel, and (h) DNA-AuNP hydrogel	89
Figure 5.2	Structures of (a) Y-shaped DNA tiles, (b) X-shaped DNA tiles, and (c) spacers modeled by NUPACK software	92
Figure 5.3	Photos of (a) SWNT and (b) MWNT dispersions in DI water without (left) and with (right) DNA modification.....	94
Figure 5.4	Photo of 13 nm AuNPs after synthesis.....	95
Figure 5.5	UV-Vis spectrum of as-synthesized AuNPs	95
Figure 5.6	Structure composed of a Y-shaped DNA tile and a spacer modeled by NUPACK software.....	97

Figure 5.7	Photo of pure DNA hydrogels and DNA hydrogel composites constructed by SI with (from left to right) Y-shaped DNA tiles, X-shaped DNA tiles, DNA-SWNT conjugates, DNA-MWNT conjugates, and DNA-AuNP conjugates	98
Figure 5.8	TEM images of (a) as-synthesized AuNPs, (b) DNA-AuNP conjugates, (c) DNA-AuNP hydrogel; (d) DNA-SWNT conjugates, (e) DNA-SWNT hydrogel; and (f) DNA-MWNT conjugates on lacy film, (g) DNA-MWNT hydrogel on lacy film, and (h) a zoomed-in image of DNA-MWNT hydrogel, showing areas of the CNT wall wrapped by DNA and the bare wall without DNA wrapping. DNA binding between CNT junctions is also shown.....	99
Figure 5.9	The band of pure AuNPs (left) appears violet under visible light, while the band of DNA-AuNP conjugates (right) retains the red color and shows a much better mobility	101
Figure 5.10	G' , G'' vs. angular frequencies showing the rheological properties of (a) pure DNA hydrogels, (b) DNA-SWNT and DNA-MWNT hydrogels, and (c) DNA-AuNP hydrogels constructed with spacers of different lengths	103
Figure 5.11	G' , G'' vs. angular frequencies showing the rheological properties of (a) hydrogel composites constructed with DNA-SWNT conjugates, X- (or Y-) shaped DNA tiles, and SI; and (b) hydrogel composites constructed with DNA-MWNT conjugates, X- (or Y-) shaped DNA tiles, and SI	105
Figure 5.12	Comparison of G' of different types of hydrogels, measured at 100 rad/s and (b) 0.1 rad/s.....	109
Figure 5.13	Trajectory maps of (a) DNA-SWNT conjugates and (b) DNA-SWNT hydrogel. Average MSD vs. lag time of (c) DNA-SWNT conjugates, with a fitted slope of 0.683, and (d) DNA-SWNT hydrogel, with a fitted slope of 0.327.....	111
Figure 5.14	Trajectory maps of (a) DNA-MWNT conjugates and (b) DNA-MWNT hydrogel. Average MSD vs. lag time of (c) DNA-MWNT conjugates, with a fitted slope of 0.911, and (d) DNA-MWNT hydrogel, with a fitted slope of 0.558.....	112
Figure 5.15	Gold electrodes of 200 μm spacings (left) and 100 μm spacings (right) for electrical characterization	114
Figure 5.16	IV curves of dehydrated samples (a) DNA-SWNT conjugates (left) vs. DNA-SWNT hydrogel (right), (b) DNA-MWNT conjugates (left) vs. DNA-MWNT hydrogel (right), (c) DNA-AuNP conjugates (left) vs. DNA-AuNP hydrogel (right) measured across gold electrodes with 200 μm spacings. Legend shows pulse number.	115
Figure 5.17	IV curves of dehydrated samples (a) DNA-SWNT conjugates (left) vs. DNA-SWNT hydrogel (right), (b) DNA-AuNP conjugates (left) vs. DNA-AuNP hydrogel (right) measured across gold electrodes with 100 μm spacings. Legend shows pulse number.	116

CHAPTER 1

Introduction and Project Overview

1.1 Vision and inspiration

Even though computers can process information and analyze data much faster than human brains in many operations, human brains have their advantages in efficiency, error-tolerance, and certain operations that computers cannot compete with^[1]. The neural system from the human brain is an extremely complicated physical system with approximately 100 billion neurons^[2]. The neural circuitry formed by the synaptic connections between neurons continuously inspires researchers to reform the structure of computer hardware and to create revolutionary computing paradigms. With the extremely high degree of connectivity and the flexibility of connection and reconnection (i.e., rewiring), the biological brains are very powerful in processing information and storing memories. Therefore, the computational prowess of human brains exceeds that of artificial computer hardware when it comes to data transfer as well as processing dynamic, unstructured, and noisy information^[3-4].

In the meanwhile, the current von Neumann computer architecture (Figure 1.1) has limitations in parallel computation and solving complex nonlinear tasks due to its inherent clock cycle for sequential processing and data communication between the processing units and stored memory^[5]. Therefore, researchers started to explore unconventional computing methods inspired by biological neural networks to develop hardware systems suitable for parallel computing. As one of the emerging developments of unconventional computing, neuromorphic computing proposes hardware structures to intentionally imitate the computational structure of the biological brains to work more efficiently for these complex tasks and applications^[6-7]. While von Neumann

architecture has completely separate units for processing and memory, neurons and the synaptic connections between neurons are responsible for both memory and processing in the human brain by changing the synaptic weight^[8]. Neuromorphic network architecture provides the benefits of accelerating the computing speed and reducing the device size, which can further reduce energy consumption. Conceptually, computers with such architectures will also have lower requirements for cooling, as there will be less heat released from device operations. Overall, neuromorphic network is a promising candidate to solve complex problems with lower energy consumption and high information capacity.

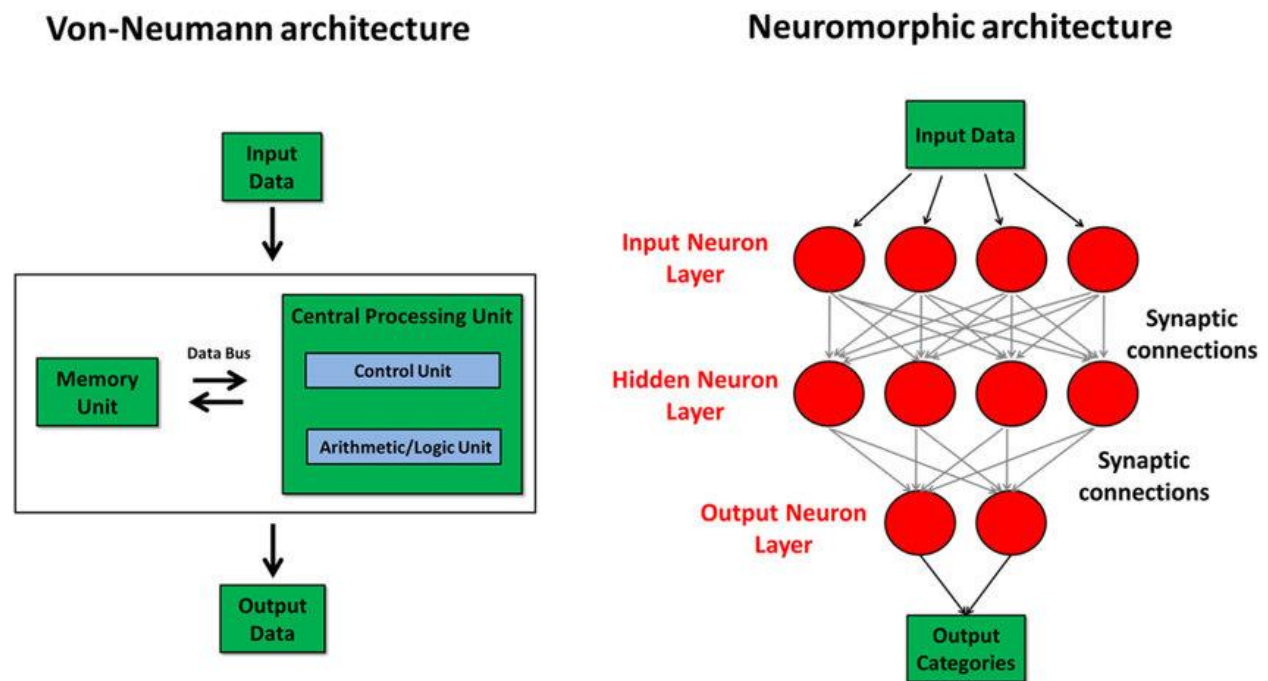


Figure 1.1 von Neumann architecture versus neuromorphic architecture (Adapted from Valle, 2018^[9]).

Among neuromorphic systems, artificial neural networks (ANNs) have shown promising computation capabilities toward applications in artificial intelligence, the Internet of Things, and

big data^[10]. However, ANNs still have disadvantages in solving relatively complex tasks, and oftentimes it is too time and energy consuming due to extensive training. As a result, reservoir computing (RC) was introduced as a low-power computational framework. RC comprises a reservoir layer, which is a nonlinear system with fixed dynamics, and a trainable output layer (Figure 1.2). The reservoir itself does not require a training/learning process, and the resulting outputs are only analyzed and adjusted by the output layer^[11]. Therefore, RC has shown higher computing performance and greater power savings for temporal pattern recognition and other data processing tasks^[12-13].

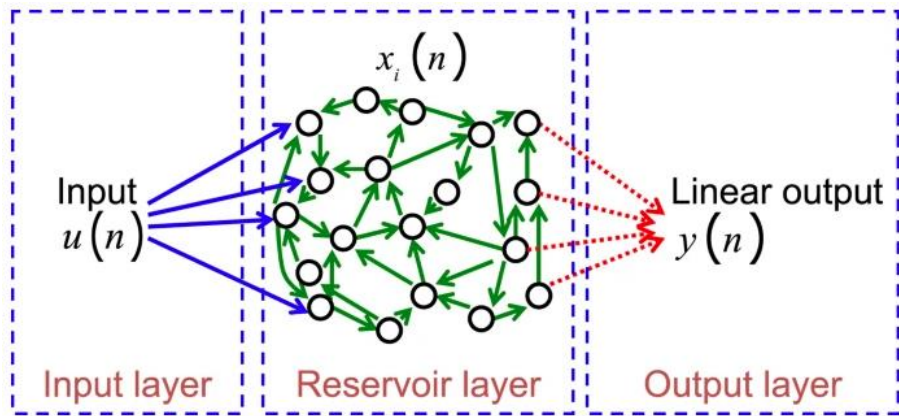


Figure 1.2 Schematic illustration of reservoir computing (Adapted from Duport, 2016^[14]).

To most efficiently realize RC in hardware, we need to have synapse-like electrical components with analog electrical behavior. Therefore, memristors became essential components to develop the RC architectures for neuromorphic computing^[10,15]. A memristor is a two-terminal passive component that exhibits nonlinear current-voltage (IV) relationship. Memristors exhibit a pinched hysteresis loop from IV characterization, which is the result of their charge-dependent resistance and memory characteristics^[16]. Self-assembled memristive nanowire networks are seen

as one of the closest hardware architectures that mimic biological neural networks. These networks also show excellent performance in neuromorphic information processing^[17]. Chalcogenide compounds such as silver sulfide (Ag_2S) have been proven to exhibit memristive behavior. For example, Hadiywarman *et al.* performed IV characterization on silver (Ag)- Ag_2S core-shell nanoparticles with supplied voltage in the range of -5 to 5 V^[18]. Hard switching with pinched hysteresis was observed, as the nanoparticle-based reservoir device transitioned from a high-resistance state to a low-resistance state. The resistive switching behavior indicates that the Ag- Ag_2S core-shell nanoparticles exhibited nonlinear and memristive behaviors, which is a result of ion migration and redox at the Ag and Ag_2S junction^[19-20]. Therefore, the Ag/ Ag_2S /Ag architecture is seen as a great candidate to build memristive networks toward the development of neuromorphic devices, including RC applications.

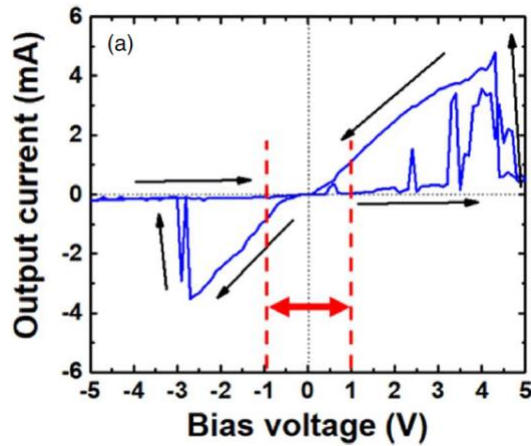


Figure 1.3 IV curve characterization of Ag- Ag_2S core-shell nanoparticles, showing hard switching with pinched hysteresis loop (Adapted from Hadiywarman, 2021^[18]).

1.2 Background

DNA self-assembly is a DNA nanotechnology that designs DNA molecules to realize the self-assembly of materials and thus to build nanostructures^[21-22]. This technique is used to assemble DNA molecules into motifs, which can be combined and connected to create two-dimensional (2D) or three-dimensional (3D) lattices^[23]. DNA self-assembly can be utilized to control the assembly of other materials into the system, which allows researchers to use the bottom-up approach to program the material properties and performance. It has the unique capability of precisely manipulating materials at the nano- and microscales and is an essential tool in the fields of nanoscience, nanotechnology, and materials science^[24,25,26]. DNA self-assembly is based on Watson-Crick complementary interaction, also known as basepairing, which allows the hybridization of complementary strands^[27]. The complementary hybridization of single-stranded DNAs (ssDNAs) enables the construction of basic DNA building units, and sticky end basepairing allows the construction of complex crystal structures. Researchers can design ssDNAs accordingly to program intermolecular interactions and thus to tailor 2D or 3D DNA-based structures.

DNA self-assembly was first proposed in the 1980s by Ned Seeman, which started to inspire the studies of connecting DNA branched junctions by basepairing to create predictable nanocrystals. Self-assembly can be a platform to guide and organize inorganic and other materials into customized 3D structures, which can be as precise as in the nanoscale. More recently, emerging studies started to show interests in creating working devices via self-assembled 3D crystals^[28-29]. Generally, common applications of DNA self-assembly include DNA walkers and machines, diagnostics, drug delivery, and biophysics^[30,31,32].

The most common strategies in DNA self-assembly are to construct DNA tiles, DNA origami, and DNA bricks. A DNA tile is a branching motif constructed by ssDNAs by strand

exchange. DNA tiles can be further assembled into more complex architectures through hybridization with themselves or other building units. It is a useful method to combine ssDNAs via sticky ends basepairing to form 2D or 3D arrays or networks^[33-34]. DNA origami is built from a long ssDNA folded into a specific, designed pattern with short “staple” strands at addressable points^[35-36]. A more recent strategy, a DNA brick, is a duplex constructed by ssDNA with four distinct domains that form staggered 3D structures and can also serve as a building unit^[37-38]. Both DNA origami and DNA bricks are significantly more complicated strategies than DNA tiles since more strands of different sequences are used to create the nanostructure. Therefore, we chose to design DNA-based tiles as our eventual strategy to build nanocircuits toward the development of nanoelectronics applications.

Finally, the DNA-based architectures can be incorporated into a hydrogel to assemble functional hydrogels with DNA architectures. DNA hydrogels can be constructed from entanglement or crosslinking mechanisms, with more details given in Figure 1.4. The structural and mechanical properties of DNA hydrogels can be easily tuned by adjusting the design and/or concentrations of DNA building blocks, such as branched DNA monomers^[46]. Therefore, these gels are highly programmable, and researchers can design the architectures to obtain desirable properties for specific applications. Besides, other nanomaterials, both organic and inorganic molecules, can be introduced into the system based on their physical or chemical interactions with DNA, so that the DNA architecture can be used as a scaffold to build DNA-based hydrogel composites^[39]. In addition, many studies on DNA hydrogels aim to design stimuli-responsive hydrogels, where the shape or formation of the gel responds to a transition in the environment such as light, pH value, and temperature^[40,41,42]. Applications of DNA hydrogels include biomedical applications such as cancer therapy and drug delivery, tissue engineering, and biosensing^[43-48].

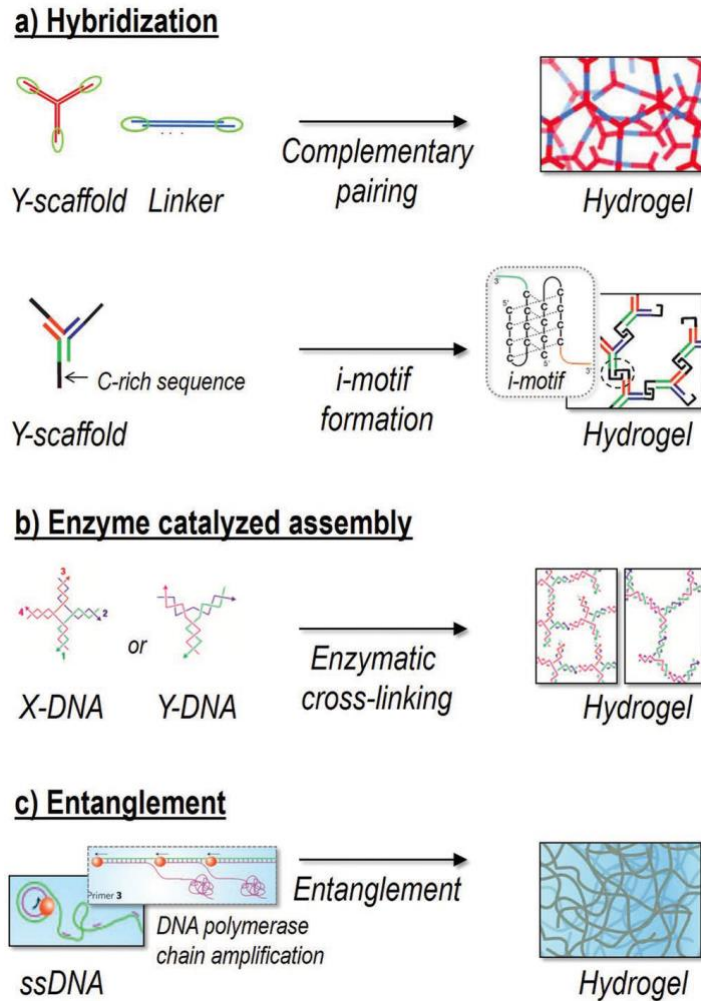


Figure 1.4 Mechanisms of DNA hydrogel formation by (a) hybridization^[44-45], (b) enzyme catalyzed assembly and DNA tiles^[46], and (c) entanglement of long DNA chains via polymerase chain amplification^[47] (Adapted from Gačanin, 2020^[48]).

1.3 Current challenges and opportunities

Currently, the most common approach for integrated circuit (IC) fabrication is photolithography processing, which is a layer-by-layer assembly method that transfers desirable patterns onto the surface of a semiconductor wafer^[49]. One challenge in lithography processing is to have a breakthrough in resolution, defined as the minimum dimension of the feature that can be

patterned on the wafer^[47]. Another challenge in lithography is to enhance the registration, which is defined as how accurately a successive mask can be overlaid with the previous pattern on the wafer. Resolution and registration together determine the precision and downscaling limitation of the IC design, which is known as the interconnect bottleneck that researchers and developers in electronic technologies eager to overcome^[50,51,52]. Besides, semiconductor lithography systems have the disadvantages of low throughput (i.e. low production rate at high resolution), extremely high cost of fabrication equipment, harsh processing conditions, and very strict requirements for the manufacturing facilities^[53,54,55]. Because of these limitations and disadvantages in lithography processing, it is highly desired to introduce a fabrication technique that has highly precise control in the nanoscale to construct architectures and complexes with desirable electrical behaviors.

One emerging opportunity that can overcome the limitations and disadvantages of lithography processing is DNA nanotechnology. Instead of researching the ability of DNA in storing and transmitting genetic information in biological systems, DNA nanotechnology uses synthetic nucleic acid-based structures as a structural engineering material and specifically designs DNA structures for technological applications^[21,56]. DNA nanotechnology shows unparalleled precision and programmability in building supramolecular structures, as DNA self-assembly has the ability to integrate other materials to create nanoelectronics circuits^[57,58,59,60]. Therefore, DNA self-assembly is a very promising technique that can change the history of human manufacturing, especially in fabricating electronic systems that are traditionally produced by lithographic methods.

The state-of-the-art integration and organization of nanoparticles using DNA self-assembly mainly focuses on linear or planar control with DNA templates^[27]. Although the arrangement of component materials such as nanoparticles can be well controlled, few studies research the assembling of large and aperiodic 3D structures. Therefore, there are opportunities in exploring

the construction of large and complex DNA-based nanostructures and systems that also have practical applications. Challenges in this topic include the improvement of stability, scalability, complexity, and functionality of such structures.

1.4 Dissertation scope

1.4.1 Project overview and research implications

The goal of our project was to develop 3D network structures and functional devices in the micro- and nanoscales using DNA self-assembly technique as well as stochastic assembly within polymeric matrices. We aimed to program and direct the construction of 2D and 3D neuromorphic network nanocircuits and to tailor their properties toward applications in nanoelectronics and unconventional computing. We explored and combined various types and forms of materials such as metallic nanoparticles and nanowires, nanotubes, oligonucleotides, and polymers. We demonstrated the strategies of using DNA self-assembly to organize nanocircuits and functional components using active nanoparticles and nanotubes, and we demonstrated the potential of DNA nanotechnology in creating precise and complex circuitry.

Our project focused on the fundamentals of materials science, including materials synthesis, DNA nanotechnology, nanofabrication, composite fabrication processes, materials characterization, as well as characterization of performance. It was a multi-disciplinary study that combined physics, chemistry, biochemistry, materials science, nanoscience and technology, electrical engineering, and mechanical engineering. We expected that the findings of this project can inspire the fabrication of integrated circuits, optoelectronics, and other nano- and microelectronic elements and devices based on wet-chemistry processing. By using DNA self-assembly to tailor templates to integrate active components into a nanoelectronic system, we

effectively addressed several disadvantages of traditional photolithographic processes, which include the requirements of very expensive instruments and access to a cleanroom facility with large space and dim lights. It also addressed the problems that photolithographic procedures can only build structures unidirectional and work layer-by-layer, which limits the design of the architectures and also requires high accuracy for every process to ensure the full functioning of the final device^[61-62]. Besides, our approach broke the limitation of nanoelectronics for biological applications, as it is more suitable and compatible with biological systems compared to the current fabrication strategies. Overall, this research may become a promising solution for sustainable and greener manufacturing in the electronic and energy industries in 5 to 15 years. The results of this study can also be important to researchers and developers in hardware architecture and design, which may allow continued scaling of Moore's Law. Our research has potential applications toward functional devices and systems such as logic circuits, sensing, communications, and molecular-scaled IC chips.

1.4.2 Research approaches and objectives

As shown in Figure 1.5, our approach for this project was to first determine the optimal synthesis protocols to produce silver nanowires that have the ideal physical properties to us. The resulting nanowires were the essential building materials for the networks later in the project. Then, our next approach was to construct and characterize 2D nanowire networks before moving forward to construct 3D composites by embedding the nanowire networks in various polymeric matrices. Finally, our third approach was to apply DNA-guided chemistry to program the construction of large nanostructures using nanoparticles and nanotubes. We built DNA-based hydrogel composites based on the fundamental physical interactions between DNA strands and nanomaterials as well as sticky end basepairing.

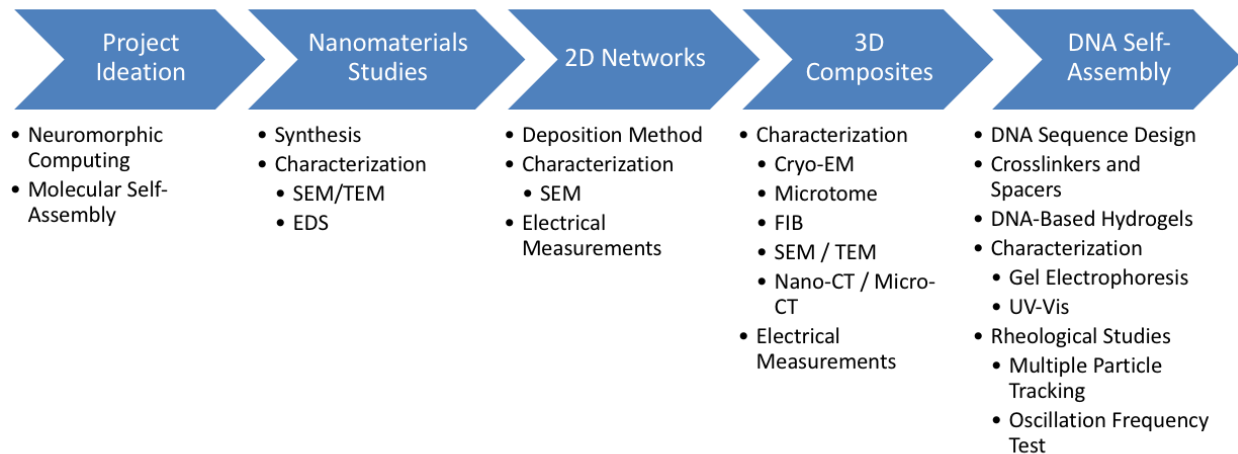


Figure 1.5 Flowchart of the project.

First of all, we focused on the component materials in the first phase of the project. We specifically studied the synthesis and characterization of silver nanowires (AgNWs) with different surface functionalities, which are reported later in Chapter 2. We focused on tuning the synthesis parameters to fabricate component materials that have the ideal dimensions and surface chemistry to us, so that they can serve as the dispersed phase materials in the following phase of the project. The dimensional information and characterization of synthesized nanowires collected from this phase of the project also provided valuable information and feedback for the second phase of the project and for the computational studies in our research group that helped to identify simulation parameters.

In the second phase of the project, we explored the 2D and 3D hybrid nanostructures that are promising candidates for neuromorphic computing hardware. Specifically, we designed, fabricated, and characterized memristive devices of novel structures using the bottom-up approach. We first studied different deposition methods to fabricate homogeneous AgNW-based networks. We then explored simple fabrication methods that are inexpensive and environmentally-friendlier

than the current processing methods for composites with embedded 3D nanowire networks. Besides, we also explored various characterization techniques for 2D and 3D networks and applied both destructive and non-destructive strategies to reveal the morphologies of the functional components as well as the surfaces of the 3D composite materials. In addition, we investigated the basic electrical properties, such as nonlinearity and electronic transport as a function of the electric field, of the resulting nanoelectronic systems. The results from this phase of the project are reported later in Chapters 2 and 3.

In the third and last phase of the project, we demonstrated using molecular recognition to control and fabricate materials at the nanoscale. We used DNA strands as a building material to organize and self-assemble nanotubes and inorganic nanoparticles to construct percolating nanocircuits toward the development of molecular electronics. We designed various types of complementary crosslinkers and spacers that hybridize to form DNA-based hydrogels. For some types of crosslinkers, we attached ssDNAs on the surfaces of gold nanoparticles and wrapped ssDNAs around carbon nanotubes to integrate these materials into the hydrogel systems. We also applied characterization tools such as oscillation frequency test, multiple particle tracking, and current-voltage curve measurement to study the mechanical and electrical properties of the gels. We proved that DNA self-assembly is a highly promising strategy in nanofabrication for low-power and programmable nanoelectronics applications. Compared to the current photolithography procedures, the bottom-up self-assembly approach is faster, easier, and cheaper in creating circuitry and nanoelectronic devices. We also showed the potential of DNA self-assembly in precise and accurate 3D integration of supramolecular complex structures. This phase of the project is reported in Chapter 5 and has been published in Gao, 2021^[63].

The conclusions and future directions regarding each phase of the project are discussed separately at the end of each of the following chapters.

Bibliography

- [1] Yang, R. Review of Resistive Switching Mechanisms for Memristive Neuromorphic Devices. *Chinese Phys. B* **2020**, *29*, 097305.
- [2] Herculano-Houzel, S. The Remarkable, Yet not Extraordinary, Human Brain as a Scaled-up Primate Brain and its Associated Cost. *PNAS* **2012**, *109*, 10661-10668.
- [3] Kuncic, Z.; Kavehei, O.; Zhu, R.; Loeffler, A.; Fu, K.; Hochstetter, J.; Li, M.; Shine, J.M. *et al.* Neuromorphic Information Processing with Nanowire Networks. *IEEE International Symposium on Circuits and Systems (ISCAS)*, **2020**, 1-5.
- [4] Chakraborty, I.; Jaiswal, A.; Saha, A.K.; Gupta, S.K.; Roy, K. Pathways to Efficient Neuromorphic Computing with Non-Volatile Memory Technologies. *Appl. Phys. Rev.* **2020**, *7*, 021308.
- [5] Park, H.-L.; Lee, Y.; Kim, N.; Seo, D.-G.; Go, G.-T.; Lee, T.-W. Flexible Neuromorphic Electronics for Computing, Soft Robotics, and Neuroprosthetics. *Adv. Mater.* **2020**, *32*, 1903558.
- [6] Zidan, M.A.; Strachan, J.P.; Lu, W.D. The Future of Electronics based on Memristive Systems. *Nat. Electron.* **2018**, *1*, 22-29.
- [7] Wang, Z.; Joshi, S.; Savel'ev, S.E. Jiang, H.; Midya, R.; Lin, P.; Hu, M.; Ge, N.; Strachan, J.P. *et al.* Memristors with Diffusive Dynamics as Synaptic Emulators for Neuromorphic Computing. *Nature Mater.* **2017**, *16*, 101-108.
- [8] Gkoupidenis, P.; Schaefer, N.; Garlan, B.; Malliaras, G.G. Neuromorphic Functions in PEDOT:PSS Organic Electrochemical Transistors. *Adv. Mater.* **2015**, *27*, 7176-7180.
- [9] Valle, J.D.; Ramirez, J.G.; Rozenberg, M.; Schuller, I.K. Challenges in Materials and Devices for Resistive-Switching-based Neuromorphic Computing. *J. Appl. Phys.* **2018**, *124*, 211101.
- [10] Choi, S.; Yang, J.; Wang, G. Emerging Memristive Artificial Synapses and Neurons for Energy-Efficient Neuromorphic Computing. *Adv. Mater.* **2020**, 2004659.
- [11] Tanaka, G.; Yamane, T.; Héroux, J.B.; Nakane, R.; Kanazawa, N.; Takeda, S.; Numata, H.; Nakano, D.; Hirose, A. Recent Advances in Physical Reservoir Computing: A Review. *Neural Networks* **2019**, *115*, 100-123.
- [12] Goudarzi, A.; Banda, P.; Lakin, M.R.; Teuscher, C.; Stefanovic, D. A Comparative Study of Reservoir Computing for Temporal Signal Processing. arXiv:1401.2224 [cs.NE]
- [13] Schumidhuber, J. Deep Learning in Neural Networks: An Overview. *Neural Networks* **2015**, *61*, 85-117.

- [14] Duport, F.; Smerieri, A.; Akrou, A.; Haelterman, M.; Massar, S. Fully Analogue Photonic Reservoir Computer. *Sci. Rep.* **2016**, *6*, 22381.
- [15] Li, Y.; Wang, Z.; Midya, R.; Xia, Q.; Yang, J.J. Review of Memristor Devices in Neuromorphic Computing: Materials Sciences and Device Challenges. *J. Phys. D: Appl. Phys.* **2018**, *51*, 503002.
- [16] Domaradzki, J.; Wojcieszak, D.; Kotwica, T.; Mankowska, E. Memristors: A Short Review on Fundamentals, Structures, Materials and Applications. *Int. J. Electron. C.* **2020**, *66*, 373-381.
- [17] Milano, G.; Luebben, M.; Ma, Z.; Dunin-Borkowski, R.; Boarino, L.; Pirri, C.F.; Waser, R.; Ricciardi, C.; Valov, I. Self-Limited Single Nanowire Systems Combining All-in-One Memristive and Neuromorphic Functionalities. *Nature Communications* **2018**, *9*, 1-10.
- [18] Hadiywarman; Usami, Y.; Kotooka, T.; Azhari, S.; Eguchi, M.; Tanaka, H. Performance of Ag-Ag₂S Core-Shell Nanoparticle-Based Random Network Reservoir Computing Device. *Jpn. J. Appl. Phys.* **2021**, *60*, SCCF02.
- [19] Eguchi, M.; Tanaka, H. Control of the Neuromorphic Learning Behavior based on the Aggregation of Thiol-Protected Ag-Ag₂S Core-Shell Nanoparticles. *Japanese Journal of Applied Physics* **2019**, *59*, 015001.
- [20] Gubicza, A.; Manrique, D.Z.; Posa, L.; Lambert, C.J.; Mihaly, G.; Csontos, M.; Halbritter, A. Asymmetry-Induced Resistive Switching in Ag-Ag₂S-Ag Memristors Enabling a Simplified Atomic-Scale Memory Design. *Sci. Rep.* **2016**, *6*, 30775.
- [21] Rangnekar, A.; LaBean, T.H. Building DNA Nanostructures for Molecular Computation, Templated Assembly, and Biological Applications, *Acc. Chem. Res.* **2014**, *47*, 1778–1788.
- [22] Wang, P.; Chatterjee, G.; Yan, H.; LaBean, T.H.; Turberfield, A.J.; Castro, C.E.; Seelig, G., Ke, Y. Practical Aspects of Structural and Dynamic DNA Nanotechnology. *MRS Bulletin* **2017**, *42*, 889-896.
- [23] Seeman, N.; Sleiman, H.F. DNA Nanotechnology. *Nat. Rev. Mater.* **2018**, *3*, 17068.
- [24] Mirkin, C.A.; Letsinger, R.L.; Mucic, R.C. Storhoff, J.J. A DNA-Based Method for Rationally Assembling Nanoparticles into Macroscopic Materials. *Nature* **1996**, *382*, 607-609.
- [25] Yang, H.; McLaughlin, C.K.; Aldaye, F.A.; Hamblin, G.D.; Rys, A.Z.; Rouiller, I.; Sleiman, H.F. Metal–Nucleic Acid Cages. *Nature Chem.* **2009**, *1*, 390-396.
- [26] Aldaye, F.A.; Sleiman, H.F. Sequential Self-Assembly of a DNA Hexagon as a Template for the Organization of Gold Nanoparticles. *Angew. Chem. Int. Ed.* **2006**, *45*, 2204-2209.
- [27] Seeman, N.C. Nucleic Acid Junctions and Lattices. *J. Theor. Biol.* **1982**, *99*, 237-247.

- [28] Wang, X.; Sha, R.; Kristiansen, M.; Hernandez, C.; Hao, Y.; Mao, C.; Canary, J.W.; Seeman, N.C. An Organic Semiconductor Organized into 3D DNA Arrays by “Bottom-up” Rational Design. *Angew. Chem. Int. Ed.* **2017**, *56*, 6445.
- [29] Hao, Y.; Kristiansen, M.; Sha, R.; Birktoft, J.J.; Hernandez, C.; Mao, C.; Seeman, N.C. A Device That Operates within a Self-Assembled 3D DNA Crystal. *Nat. Chem.* **2017**, *9*, 824-827.
- [30] Yan, X.; Huang, S.; Wang, Y.; Tang, Y.; Tian, Y. Bottom-Up Self-Assembly Based on DNA Nanotechnology. *Nanomaterials* **2020**, *10*, 2047.
- [31] Jorge, A.F.; Eritja, R. Overview of DNA Self-Assembling: Progresses in Biomedical Applications. *Pharmaceutics* **2018**, *10*, 268.
- [32] Li, Z.; Wang, J.; Li, Y.; Liu, X.; Yuan, Q. Self-Assembled DNA Nanomaterials with Highly Programmed Structures and Functions. *Mater. Chem. Front.* **2018**, *2*, 423-436.
- [33] Lin, C.; Liu, Y.; Rinker, S.; Yan, H. DNA Tile Based Self-Assembly: Building Complex Nanoarchitectures. *Chem. Phys. Chem.* **2006**, *7*, 1641-1647.
- [34] Parikka, J.M.; Sokołowska, K.; Markešević, N.; Toppari, J.J. Constructing Large 2D Lattices Out of DNA-Tiles, *Molecules* **2021**, *26*, 1502.
- [35] Rothemund, P. Folding DNA to Create Nanoscale Shapes and Patterns. *Nature* **2006**, *440*, 297–302.
- [36] Brown, S.; Majikes, J.; Martínez, A.; Girón, T.M.; Fennell, H.; Samano, E.C.; LaBean, T.H. An Easy-to-Prepare Mini-Scaffold for DNA Origami. *Nanoscale* **2015**, *7*, 16621-16624.
- [37] Ke, Y.; Ong, L.L.; Shih, W.M.; Yin, P. Three-Dimensional Structures Self-Assembled from DNA Bricks. *Science* **2012**, *338*, 1177-1183.
- [38] Wei, B.; Dai, M.J.; Yin, P. Complex Shapes Self-Assembled from Single-Stranded DNA Tiles. *Nature* **2012**, *485*, 6223-626.
- [39] Bush, J.; Hu, C.-H.; Veneziano, R. Mechanical Properties of DNA Hydrogels: Towards Highly Programmable Biomaterials. *Appl. Sci.* **2021**, *11*, 1885.
- [40] Cheng, E.; Xing, Y.; Chen, P.; Yang, Y.; Sun, Y.; Zhou, D.; Xu, L.; Fan, Q.; Liu, D. A pH-Triggered, Fast-Responding DNA Hydrogel. *Angew. Chem. Int.* **2009**, *48*, 7660-7663.
- [41] Shi, J.; Shi, Z.; Dong, Y.; Wu, F.; Liu, D. Responsive DNA-Based Supramolecular Hydrogels. *ACS Appl. Bio. Mater.* **2020**, *3*, 2827-2837.
- [42] Kahn, J.S.; Hu, Y.; Wilner, I. Stimuli-Responsive DNA-Based Hydrogels: From Basic Principles to Applications. *Acc. Chem. Res.* **2017**, *50*, 680-690.

- [43] Zhou, L.; Jiao, X.; Liu, S.; Hao, M.; Cheng, S.; Zhang, P.; Wen, Y. Functional DNA-Based Hydrogel Intelligent Materials for Biomedical Applications. *J. Mater. Chem. B*. **2020**, *8*, 1991.
- [44] Xing, Y.; Cheng, E.; Yang, Y.; Chen, P.; Zhang, T.; Sun, Y.; Yang, Z.; Liu, D. Self-Assembled DNA Hydrogels with Designable Thermal and Enzymatic Responsiveness. *Adv. Mater.* **2011**, *23*, 1117-1121.
- [45] Cheng, E.; Xing, Y.; Chen, P.; Yang, Y.; Sun, Y.; Zhou, D.; Xu, L.; Fan, Q.; Liu, D. A pH-Triggered, Fast-Responding DNA Hydrogel. *Angew. Chem. Int.* **2009**, *48*, 7660-7663.
- [46] Um, S.H.; Lee, J.B.; Park, N.; Kwon, S.Y.; Umbach, C.C., Luo, D. Enzyme-Catalysed Assembly of DNA Hydrogel. *Nat. Mater.* **2006**, *5*, 797-801.
- [47] Lee, J.B.; Peng, S.; Yang, D.; Roh, Y.H.; Funabashi, H.; Park, N.; Rice, E.J.; Chen, L.; Long, R.; Wu, M.; Luo, D. A Mechanical Metamaterial Made from a DNA Hydrogel. *Nat. Nanotechnol.* **2012**, *7*, 816-820.
- [48] Gačanin, J.; Synatschke, C.V.; Weil, T. Biomedical Applications of DNA-Based Hydrogels. *Adv. Funct. Mater.* **2020**, *30*, 1906253.
- [49] van Assenbergh, P.; Meinders, E.; Geraedts, J.; Dodou, D. Nanostructure and Microstructure Fabrication: From Desired Properties to Suitable Processes. *Small* **2018**, *14*, 1703401.
- [50] Ouyang, S.; Xie, Y.; Wang, D.; Zhu, D.; Xu, X.; Tan, T.; Fong, H.H. Surface Patterning of PEDOT:PSS by Photolithography for Organic Electronic Devices. *J. Nanomater.* **2015**, *2015*, 603148.
- [51] Adrega, T.; Lacour, S.P. Stretchable Gold Conductors Embedded in PDMS and Patterned by Photolithography: Fabrication and Electromechanical Characterization. *J. Micromech. Microeng.* **2010**, *20*, 055025.
- [52] Schmaltz, T.; Sforazzini, G.; Reichert, T.; Frauenrath, H. Self-Assembled Monolayers as Patterning Tool for Organic Electronic Devices. *Adv. Mater.* **2017**, *29*, 1605286.
- [53] Liu, H.; Zhang, G.; Zheng, X.; Chen, F.; Duan, H. Emerging Miniaturized Energy Storage Devices for Microsystem Applications: From Design to Integration. *Int. J. Extrem. Manuf.* **2020**, *2*, 042001.
- [54] Hasan, R.M.M.; Luo, X. Promising Lithography Techniques for Next-Generation Logic Devices. *Nanomanuf. Metrol.* **2018**, *1*, 67-81.
- [55] Bosworth, J.K.; Ober, C.K. Top-Down versus Bottom-Up Patterning of Polymers. *Polymer Science: A Comprehensive Reference*, **2012**, 9-15.

- [56] Majikes, J.M.; Ferraz, L.C.C.; LaBean, T.H. pH-Driven Actuation of DNA Origami via Parallel I-Motif Sequences in Solution and on Surfaces. *Bioconjugate Chem.* **2017**, *28*, 1821-1825.
- [57] Vargas-Baca, I.; Mitra, D.; Zulyniak, H.J.; Banerjee, J.; Sleiman, H.F. Solid-Phase Synthesis of Transition Metal Linked, Branched Oligonucleotides. *Angew. Chem. Int. Ed.* **2001**, *40*, 4629-4632.
- [58] Klinkova, A.; Choueiri, R.M.; Kumacheva, E. Self-Assembled Plasmonic Nanostructures. *Chem. Soc. Rev.* **2014**, *43*, 3976-3991.
- [59] Li, H.; Carter, J.D.; LaBean, T.H. Nanofabrication by DNA Self-Assembly. *Mater. Today* **2009**, *12*, 24-32.
- [60] Estrich, N.A.; Hernandez-Garcia, A.; de Vries, R.; LaBean, T.H. Engineered Diblock Polypeptides Improve DNA and Gold Solubility during Molecular Assembly. *ACS Nano* **2017**, *11*, 831-842.
- [61] Martinez-Duarte, R.; Madou, M.J. SU-8 Photolithography and Its Impact on Microfluidics; *CRC Press* **2011**; 231-268.
- [62] Choi, S.; Park, J.K. Two-Step Photolithography to Fabricate Multilevel Microchannels. *Biomicrofluidics* **2010**, *4*, 46503.
- [63] Gao, M.; Krissanaprasit, A.; Miles, A.; Hsiao, L.C.; LaBean, T.L. Mechanical and Electrical Properties of DNA Hydrogel-Based Composites Containing Self-Assembled Three-Dimensional Nanocircuits, *Appl. Sci.* **2021**, *11*, 2245.

CHAPTER 2

Silver Nanowire Synthesis and Characterization

2.1 Introduction and background

2.1.1 Background

Silver nanowires (AgNWs) are seen as one of the most promising one-dimensional nanomaterials for nanoelectronic application, including soft, transparent, and stretchable electrodes, wearable electronics, solar cells, and sensors^[64,65,66]. AgNWs are especially attractive for their one-dimensional nanostructures, high electrical conductivity, mechanical flexibility, and optical transparency. These properties make AgNWs an ideal candidate to be integrated into conductive or semiconductive nanocomposites, especially for flexible transparent conductive film applications^[67-68]. The properties and performance of AgNW-based composites are adjustable and depend heavily on their dimensions and morphologies. Therefore, having precise control of the nanowire dimensions has frequently been of the core of studies on this topic^[69-70].

2.1.2 Silver nanowire fabrication

The fabrication of metallic nanowires has attracted a large audience in recent years with the development of electrodes for thin film applications. Common metallic nanomaterials that can be synthesized in the wire shape include copper^[71-72], gold^[73-74], and silver^[75-76].

Reported routes to synthesize AgNWs include polyol process, hydrothermal method, microwave-assisted approach, electrochemical technique, UV irradiation technique, and template technique^[77,78,79,80,81]. Of all these synthesis approaches, the solution-based polyol process is most commonly used because it is convenient, low-cost, and comparatively safe. The polyol process also does not require special equipment or instrumentation and is most suitable to be scaled up for

mass production. The polyol route was first developed by the Xia group^[82-83]. Briefly, it is achieved by the reduction of metallic salt by a polyol while controlling the crystallization to be unidimensional growth of isotropic nanoparticles into anisotropic confinement^[84-85]. Based on this strategy, Andres *et al.* reported a rapid method to synthesize AgNWs of high aspect ratios under an hour with the polyol approach^[143], where they used ethylene glycol to reduce the metal precursor in the presence of a nucleating agent and a capping agent poly(vinylpyrrolidone) (PVP). It is one of the quickest reported synthesis methods that can produce AgNWs of high aspect ratios. Andres *et al.* demonstrated that well synthesized AgNWs with an average diameter of 50 nm and 200 nm should both show a broad absorption peak between 390 nm and 425 nm at the UV-Vis absorption spectrum (Figure 2.1)^[86]. They also showed that AgNWs synthesized with this method have excellent performance in many applications, such as organic photovoltaics.

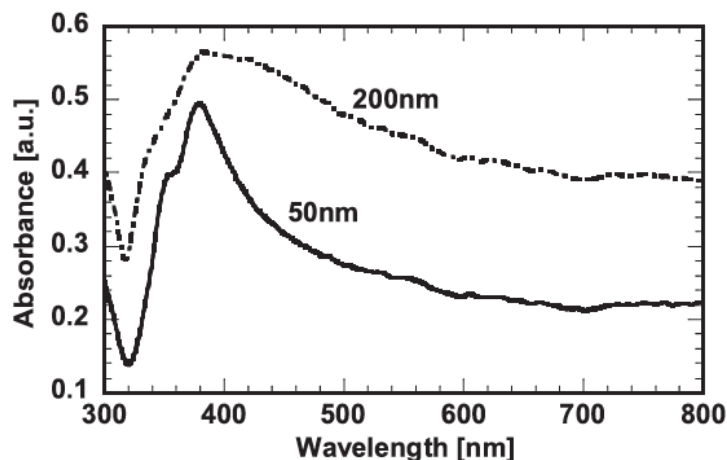


Figure 2.1 Absorption spectra of AgNW suspension in ethanol for two nanowire samples with either 50 or 200 nm average diameter (Adapted from Andres, 2015^[143]).

2.1.3 Project Overview

The electrical conductivity of AgNW networks is greatly influenced by the resistance at nanowire junctions. Based on the studies of electrical transport within nanowire networks, longer AgNWs help to construct percolation paths, as there are fewer wire junctions with long nanowires when keeping the volume fraction of conducting materials constant^[87-88]. Therefore, for our purpose of building percolating paths with AgNW networks, we would like to apply AgNWs of the highest aspect ratios that we can feasibly and reproducibly fabricate. At the same time, we also aim to compare the properties and performance of networks built with nanowires of different lengths. Therefore, a robust synthesis method that can produce AgNWs of different ranges of lengths is highly desired. Although many previous studies have reported synthesis protocols to obtain AgNWs of different dimensions, from as short as several micrometers to as long as a few hundred micrometers, they utilized different reagents and synthesis procedures that lead to different chemical residues in the product solutions^[64,89]. For our further studies of AgNW networks, it is important for us to make sure the synthesized nanowires have the same surface conditions. Therefore, we would like to formulate a robust synthesis protocol in this project that allows us to systematically control the dimensions of AgNWs by tuning several major reaction parameters.

After investigating both the hydrothermal method and the polyol approach for AgNW synthesis, we chose to use an adapted polyol approach where silver nitrate is reduced in ethylene glycol with the presence of PVP and CuCl₂. The polyol approach allows us to synthesize AgNWs at a low cost, with basic laboratory supplies, while preventing potential safety issues that could arise from high pressure and ultra-high temperature during the hydrothermal procedures^[90]. One objective of this project is to further explore and improve the current one-step synthesis methods

reported by Andres *et al.* to rapidly grow AgNWs of different ranges of lengths. Although there are studies that use a successive multistep method to synthesize ultra-long AgNWs^[91-92], we would like to avoid ultra-long nanowires, which is generally defined as AgNWs with over 100 μm lengths, so that we can eventually apply molecular self-assembly techniques to integrate nanowires with self-assembled materials. It is more challenging to apply DNA self-assembly to build stable architectures with materials much larger in scales. Due to this reason, we are also aiming to produce nanowires with an average diameter below 150 nm.

Here, we report a parametric study and modification of AgNW synthesis to achieve nanowires with different lengths and aspect ratios. We especially studied the influence of temperature during different reaction phases, reaction time, stirring time, and PVP chain length on the final dimensions of AgNW products. The reported one-pot one-step polyol-mediated method can efficiently and consistently synthesize AgNWs with minimal impurities. Several tips and cautions are also advised as described in this chapter in order to support a robust production. Chemical analysis of the final product has been conducted by energy-dispersive X-ray spectroscopy (EDS) and ultraviolet-visible spectroscopy (UV-Vis), and the physical appearance and dimensions of the nanowires have been imaged and collected by transmission electron microscopy (TEM) and scanning electron microscopy (SEM).

2.2 Silver nanowire synthesis

2.2.1 Influence of reaction temperature, reaction time, PVP chain length, and stirring condition

Based on previous studies, the most important conditions during AgNW synthesis that determine the final length of AgNWs are the reaction time, temperature, stirring time, and the

molecular weight (chain length) of PVP^[62]. In order to further investigate the influence of these conditions on the synthesized AgNWs and to determine the parameters that yield AgNWs with high aspect ratios, the following parameters (Table 2.1) were tested. In short, each of the four parameters were experimented with the listed conditions while keeping the other three parameters constant, to specifically determine the optimal condition for each of the reaction parameters. As the most important parameter, the reaction temperature was examined from 155°C to 185°C. We also performed temperature ramping (i.e. different temperature setting at different phases of the reaction) to see if the influence of reaction temperature is stage-specific during AgNW synthesis. Second, the reaction times between 20 min to 45 min were tested. The reaction time counted from the moment that the precursor is completely added to the reaction flask to the moment that heating is stopped and that the flask is quenched in room temperature water to stop the reaction. Thirdly, the optimal ratio of PVP of different chain lengths (molecular weights) was tested. While the total mass of PVP added to the reaction was kept constant, the mass ratio of the two different types of PVP was adjusted. Last not but least, the time of stirring with a magnetic bar was experienced to see whether or not stirring influences the lengths of AgNWs. In Table 2.1, 0% indicates no stirring for the entire reaction, 50% indicates stirring for the first half of the reaction time, and 100% shows stirring throughout the entire reaction.

Table 2.1. Variables and values examined in the parametric study of AgNW synthesis.

Temperature	Reaction time	PVP ratio*	Stirring†
155 °C	20 min	2:1	0%
160 °C	25 min	1:1	20%
165 °C	30 min	1:2	33%
170 °C	35 min	1:3	50%
175 °C	40 min	1:4	66%
180 °C	45 min	1:5	100%
185 °C			

* Mass ratio of PVP (average molecular weight ~55,000) to PVP (average molecular weight ~360,000).

† Percentage of total reaction time that the solution is being stirred with a magnetic bar, counted from the beginning of the reaction.

It was previously proposed that the formation of AgNWs involves three steps: nucleation, evolution of nuclei to form seeds, and growth of seeds into nanocrystals^[93]. The final form of synthesized nanostructures is controlled by the thermodynamics and kinetics of each step, which involves diffusion and surface energy minimization^[86]. The nucleating agent in the synthesis significantly influences the morphology of seeds, which governs the shape of final nanocrystal products. Common nucleating agents for AgNW synthesis are chloride salts such as NaCl, FeCl₃ and CuCl₂^[94]. We chose to use CuCl₂ as the nucleating agent since they have been reported to support the fabrication of longer AgNWs. After testing various combinations of the reaction conditions listed in Table 2.1, we concluded that the reaction time needs to be at least 40 min for which the flask is at an sufficient temperature of 175°C to produce long AgNWs. We also found that the optimal mass ratio of PVP (~55,000) to PVP (~360,000) is at 1:3. Our parametric study showed that stirring does not have a very significant influence on the length of the final AgNW product compared to the other parameters, although it slightly helps to grow long AgNWs when stirring is stopped at the beginning of the growth phase of the reaction.

First of all, the reaction temperature needs to reach and be kept at 175°C to grow long AgNWs, and a lower temperature can not support the growth of AgNWs over 60 μm. When the reaction temperature is at 160°C, the average AgNW length is below 30 μm. And when the reaction temperature is lower than 160°C, silver ions do not effectively grow into the wire shape, and they appear as nanoparticles when characterized by electron microscopes. In addition, PVP will form a foaming supernatant layer on the surface of the solution if the reaction temperature is higher than 180°C. Although the AgNWs in the solution will still be good to use, the yield of AgNWs will decrease significantly since the foaming supernatant needs to be extracted and discarded. Therefore, the optimum reaction temperature to grow long AgNWs is in the range of 175-180°C. A lower temperature of 160-175°C supports the growth of short AgNWs, where the average lengths are listed in Figure 2.2. During synthesis, a fluctuation of temperature within ±3°C was found to be acceptable, but larger derivations from the desired temperature are not desirable. We highly recommend future research to control the reaction at the desired temperature with minimal fluctuation.

Secondly, the influence of reaction time on AgNW product is studied. While setting the reaction temperature at 175°C, we observed an improvement of average nanowire length from 61.2 μm to 63.8 μm when we increased the reaction time from 20 min to 30 min. When we extended the reaction time from 30 min to 40 min, we also saw an increase in nanowire length to 68.1 μm. However, extending the reaction time further did not prove to have a significant influence on the length of AgNWs. From the temperature ramping test, we found that it is important to make sure the reaction is at the desired temperature discussed above for the entire reaction time to ensure that AgNWs would grow to the projected lengths. If the temperature of the first 10 min of the growth phase is lower than the desired temperature, one can raise the temperature to the ideal range and

keep the reaction for another 40 min (or the desired total reaction time) to allow nanowires to grow to the projected length. Although the final nanowire product will have a wider range of lengths (with a larger proportion of short AgNWs compared to the product from an ideal reaction), the longest nanowires will still be of the desired length.

Thirdly, the mass ratio of PVP of two different molecular weights was considered to improve the synthesis protocol. PVP, as the capping agent, determines the growth mechanism of nanostructured silver at different crystalline face surfaces^[95]. Specifically, PVP has a strong interaction with the (100) planes of AgNW and a weaker interaction with the (111) planes, the two ends of the rod-shaped nanocrystals^[96]. This confinement assists silver atoms to diffuse to the two active ends of the nanocrystals in the growth phase and thus grow anisotropically at the [111] direction during synthesis^[89]. Therefore, PVP directly influences the final shape and aspect ratio of AgNWs. Most of the previous studies only used PVP of one particular molecular weight. Wang *et al.* particularly studied the influence of the chain length of PVP on the final dimensions of AgNW. They found that PVP of higher molecular weight assist to fabricate AgNWs of high aspect ratios^[97]. However, we observed that it is more difficult to properly dissolve PVP of high molecular weight in ethylene glycol and there can still be undissolved PVP even when the solution appears all clear. And when this happens, a foaming supernatant would form during AgNW synthesis even at a temperature lower than 180°C. Therefore, instead of using one type of PVP, we improved the protocol by mixing PVP of high molecular weight (MW ~360,000) with PVP of low molecular weight (~55,000) to avoid this issue. Our further parametric study showed that the optimal mass ratio of PVP (~55,000) to PVP (MW ~360,000) is 1:3, which effectively avoids the formation of foaming supernatant and thus supports a high yield production.

The last parameter studied was the stirring time. Unalan *et al.* researched the influence of stirring rate on the dimensions of synthesized AgNWs^[69]. They reported that a faster stirring rate results in AgNWs of smaller lengths and diameters. Furthermore, Andres *et al.* demonstrated the stirring sequence for a 30 min reaction is to apply stirring for the first 10 min, then no stirring for the following 20 min to produce long AgNWs^[143]. Based on these reports, we decided to examine different stirring conditions to further investigate the root cause of this impact. After experimenting with different stirring conditions, we found that the optimal stirring condition is less related to the time that the solution is being stirred, but more related to the stage of the reaction when the solution is being stirred. Specifically, to ensure the production of long AgNWs, we found that the solution needs to be stirred from the moment that it is being heated to the end of the stage where silver nuclei have matured to form seeds. This strategy ensures that the temperature of the solution is homogeneous at the stage where an endothermal environment is most important to the reaction. Stirring at this stage can also effectively prevent the aggregation of seeds that have not started to grow into the rod or wire shape. However, extended stirring during the growing stage decreases the length of AgNWs, as demonstrated by Andres *et al* and also observed by us. We found that the best way to determine the time to stop stirring is by observing the color of the solution. At the initial stage where silver particles are formed, the solution appears as transparent light yellow. As the pentagonal silver particle seeds are formed right before the growth stage, the color of the solution transitions from light yellow to translucent (almost opaque) light ivory/pearl. This is when stirring was stopped, so that there was no stirring during the growth phase of synthesis. Eventually, the final AgNW product appears grey in the solution.

As a summary, our parametric study determined that the optimal mass ratio of PVP (~55,000) to PVP (MW ~360,000) is 1:3, and magnetic stirring should be stopped at the beginning

of the growth phase of the reaction. The averaged AgNW lengths produced with different reaction time (20-40 min) and temperature (160-175 °C) are presented in Figure 2.2. In addition, the protocols to synthesize long AgNWs with minimal impurities are formalized in Section 2.2.2. When production of short AgNWs is desired, the reaction temperature and time from the protocols can be adjusted accordingly as specified in Figure 2.2, while other conditions and procedures are kept the same.

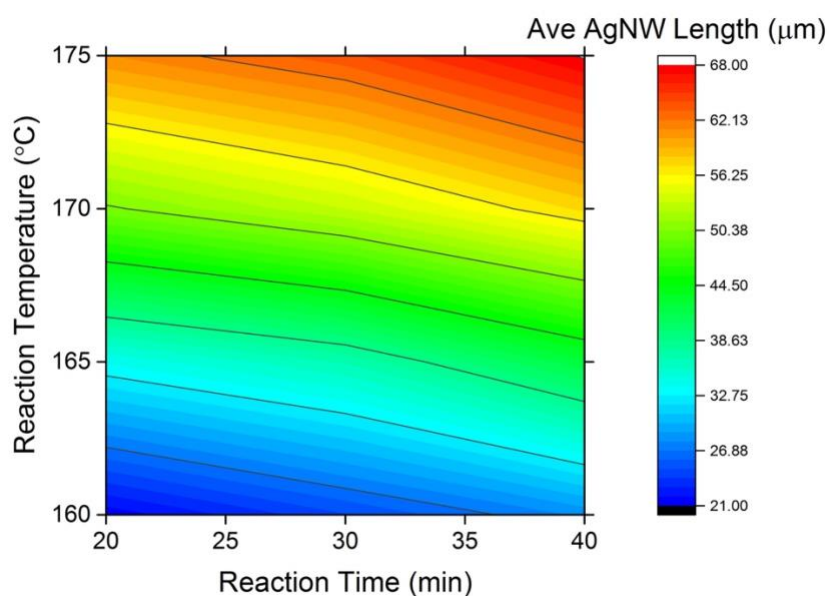


Figure 2.2 Averaged AgNW lengths produced with different reaction temperature and time.

2.2.2 Protocol for silver nanowire synthesis with a hot plate

Materials. Silicon oil (for oil baths, from -50°C to $+200^{\circ}\text{C}$, Sigma-Aldrich) is used for the oil bath. Silver nitrate (AgNO_3 ; $>99\%$, Sigma-Aldrich) and ethylene glycol (EG; 99.8% , Sigma-Aldrich) are used as metal source material and the reducing agent, respectively. A mixture of poly(vinylpyrrolidone) (PVP; average MW $\sim 55,000$, Sigma-Aldrich) and poly(vinylpyrrolidone) (PVP; average MW $\sim 360,000$, Sigma) is used as the capping agent. Copper(II) chloride (CuCl_2 ;

dehydrate, 99.999%-Cu, Strem Chemicals) is used as the nucleating agent. Ethanol (Ethyl alcohol, pure, 200 proof, Sigma-Aldrich) and acetone (Fisher Chemicals) are used to wash and purify the final product.

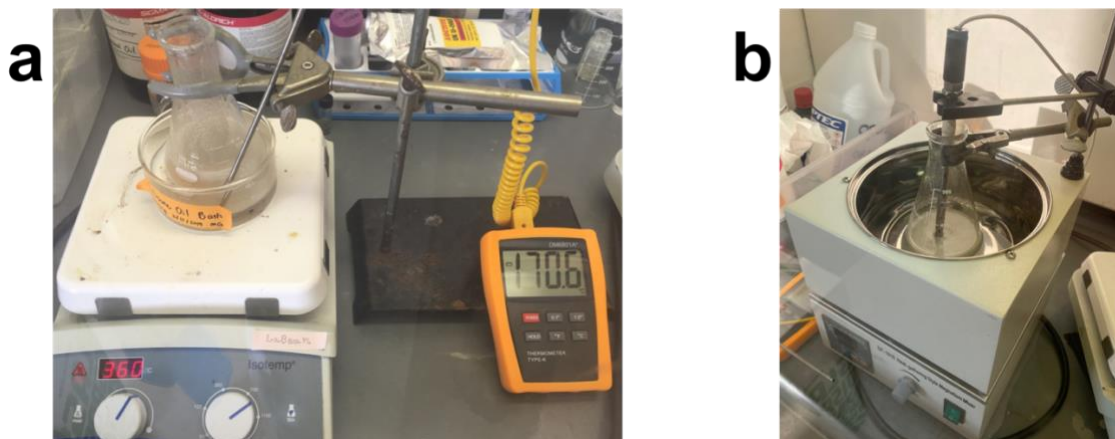


Figure 2.3 Photos of AgNW synthesis setups with (a) hot plate approach and (b) thermostatic bath approach.

Synthesis. The hot plate approach setup to synthesize AgNWs is shown in Figure 2.3 (a). First, 480 mg of AgNO_3 is dissolved in 22 mL ethylene glycol by bath sonication. 380 mg of PVP is separately dissolved in 22 mL ethylene glycol by bath sonication and vortex mixing. Then, 0.54 mg of CuCl_2 is dissolved in 160 mL ethylene glycol in a 250 mL flask, and the flask is suspended inside an oil bath that is set on a hot plate. A magnetic bar is put inside the flask and stirring is turned on as soon as the hot plate is set for heating. Next, the hot plate is set to an appropriate temperature that allows the solution inside the flask to reach and maintain a constant temperature of 175°C . Once the solution in the flask reaches the homogeneous temperature, the PVP solution prepared in the first step is added into the flask by a syringe drop by drop. The temperature of the solution in the flask is allowed to return to 175°C again. Then, the AgNO_3 solution prepared in the

first step is added to the flask with a syringe drop by drop. Once the solution inside the flask starts to turn cloudy and become translucent, the AgNO_3 solution can be added at a faster rate. Once all the reagents have been added to the flask, one can start to count for the reaction time. Shortly after all the reagents are added to the flask, the color of the solution will turn to translucent light ivory/pearl, which over time will become more and more opaque. Eventually, it will turn to grey with some splash of shiny silver indicating that AgNWs have been grown (Figure 2.4). One should stop stirring when the color just turns light ivory.

Once the reaction time reaches 40 min, heating is stopped, and the flask is removed from the oil bath. The flask is then quenched in room temperature water to stop the reaction. The product is left at room temperature until it completely cools down. Once the solution is cooled to room temperature, the final product inside the flask is transferred to several 50 mL polypropylene centrifuge tubes. The next step is to repeatedly wash and purify the final product with ethanol and acetone in turn to remove any PVP, ethylene glycol, and nanoparticle impurities. For each wash, the solution is centrifuged at 2000 rpm for 30 minutes to precipitate nanowires before removing the supernatant solution and resuspending the wires in fresh solvent. After a total of six washes (three times with ethanol and three times with acetone), the final AgNW product is preserved in ethanol for future use.

Caution and notes. First of all, the purity and quality of chemicals used in the synthesis are very important and are directly related to the quality of the final AgNW product. We recommend using analytical-grade chemical reagents and solvents. Second, it is essential to make sure all reagents are well dissolved in ethylene glycol before adding them to the reaction. Undissolved chemicals can result as particles/crystal/impurities, may change the final dimensions of AgNWs, and would also decrease the yield of AgNW product. When dissolving AgNO_3 in

ethylene glycol, it is recommended that the sonication time does not go over 5 min. The solution will turn to a slightly darker color when the sonication time is over 10 min, and the final AgNW product that utilized such AgNO_3 precursor tend to have more nanoparticle impurities in the solution. Besides, it is important to make sure that the reaction temperature is constant during the entire synthesis. Our temperature ramping study shows that the length of AgNWs cannot be guaranteed if the reaction temperature drops over 5°C for more than 5 min during any phase of the reaction. In addition, although it is proven that magnetic stirring during the growth phase of the reaction will decrease the length of the final AgNW product, this consideration is not as important as the other reaction parameters such as reaction temperature and time. Therefore, if one needs to apply stirring throughout the entire reaction to ensure that the temperature of the reaction solution is homogeneous, one should put temperature as a priority. Some future processing with AgNWs could shorten the length of nanowires, and one should keep this in mind in order to produce AgNWs of ideal dimensions for their specific applications.



Figure 2.4 AgNWs stored in ethanol after purification.

2.2.3 Protocol for silver nanowire synthesis with a thermostatic bath

Although it is simple and convenient to use basic laboratory equipment such as a hot plate and a flat beaker to synthesize nanomaterials, it is difficult to scale up the production with this setup. Therefore, we also applied a second setup using a thermostatic bath to mass-produce AgNWs, as shown in Figure 2.3 (b). We used a DF-101S heat-gathering style magnetism mixer as the thermostatic bath. Silicone oil was added directly into the bath, and a 1L reaction flask was suspended in the oil. The synthesis procedure is the same as the protocol for using a hot plate, and the scaled-up parameters are listed in Table 2.2. This approach scales up production of AgNWs by at least 3-fold. Since a much larger volume of solution is used in this approach compared to the hot plate approach, it is advised to slowly heat up the silicone oil and the reaction solution before adding AgNO₃ precursor to ensure that the solution temperature is homogeneous.

Table 2.2. Reagent specifications for AgNW synthesis with a thermostatic bath.

Reagent	Mass	Volume of ethylene glycol
CuCl ₂	1.62 mg	480 mL
AgNO ₃	1.44 g	66 mL
PVP (MW ~55,000)	285 mg	16.5 mL
PVP (MW ~360,000)	855 mg	49.5 mL

2.3 Characterization

2.3.1 Chemical analysis

We first used UV-Vis spectroscopy to quickly examine the final AgNWs product after purification and compared the results with prior studies. AgNWs were dispersed in pure ethanol in a standard-sized quartz cuvette and then examined by a spectrophotometer (Thermo Scientific NanoDrop 2000c). Our samples showed an absorption peak at ~390 nm, which agrees with the

studies by Andres, *et al*^[143]. The UV-Vis spectroscopy results provide preliminary evidence that we have successfully synthesized AgNWs.

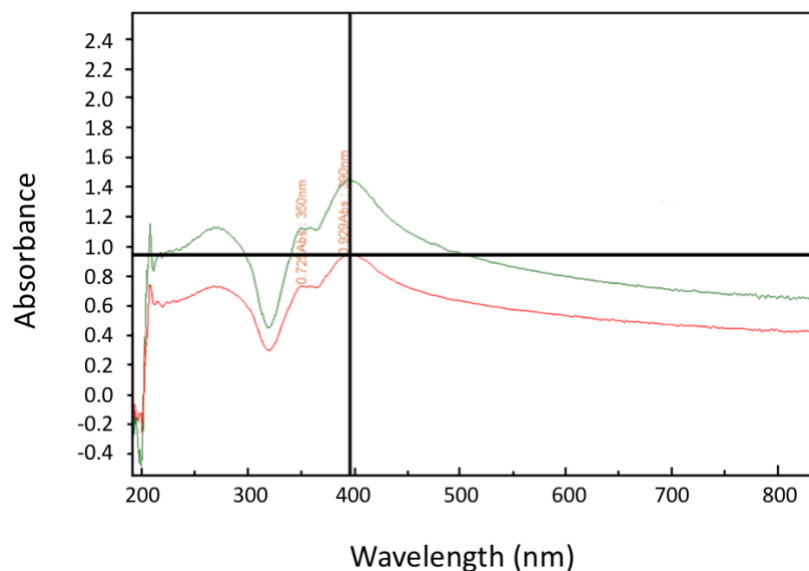


Figure 2.5 Absorption spectrum of AgNWs after synthesis and purification, showing an absorption peak at ~390 nm.

Energy-dispersive X-ray spectroscopy (EDS) mode of JEOL JSM-6010LA scanning electron microscope (SEM) was used to perform elemental mapping on the synthesized nanowires. A sample was prepared following the typical SEM sample preparation on an SEM mount. The EDS results shown in Figure 2.6 agreed with UV-Vis analysis on chemical characterization and confirmed that the synthesized product is silver. Detected carbon is from the carbon tape on the SEM mount.

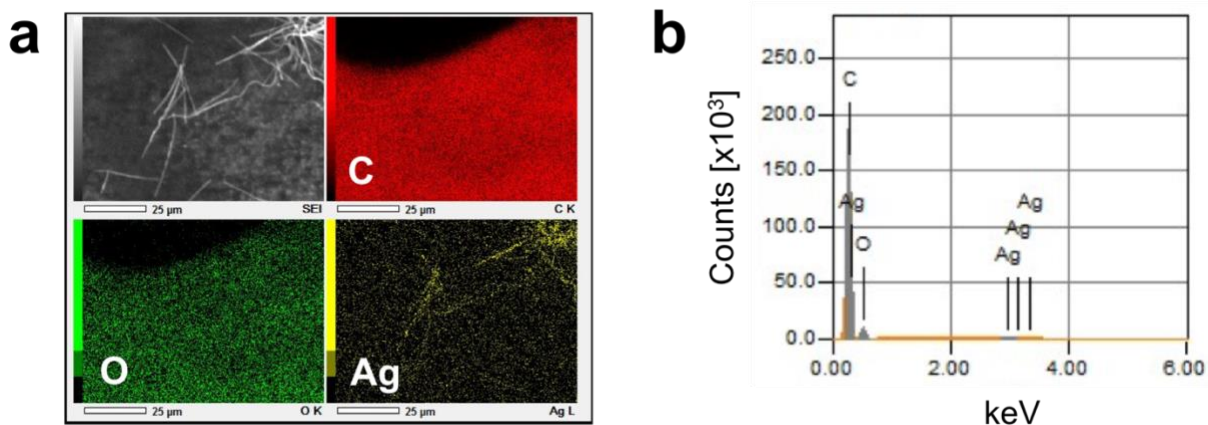


Figure 2.6 (a) An SEM image of AgNWs and its corresponding EDS element maps, and (b) EDS spectrum of the detected area.

2.3.2 Microscope imaging

In order to further characterize synthesized AgNWs, we first applied optical microscope imaging with AmScope Darkfield Microscope and Nikon Optiphot 100 to rapidly and conveniently check the conditions of nanowires before using more time-consuming visualization methods such as SEM and transmission electron microscope (TEM). Optical microscopy visualization gives us good idea of the distribution of lengths of AgNWs and the condition of potential impurities in the solution (Figure 2.7). To prepare the samples, 3 μL of AgNWs dispersed in ethanol are drop cast onto a glass microscope slide that has been previously cleaned with acetone, ethanol, and DI water.

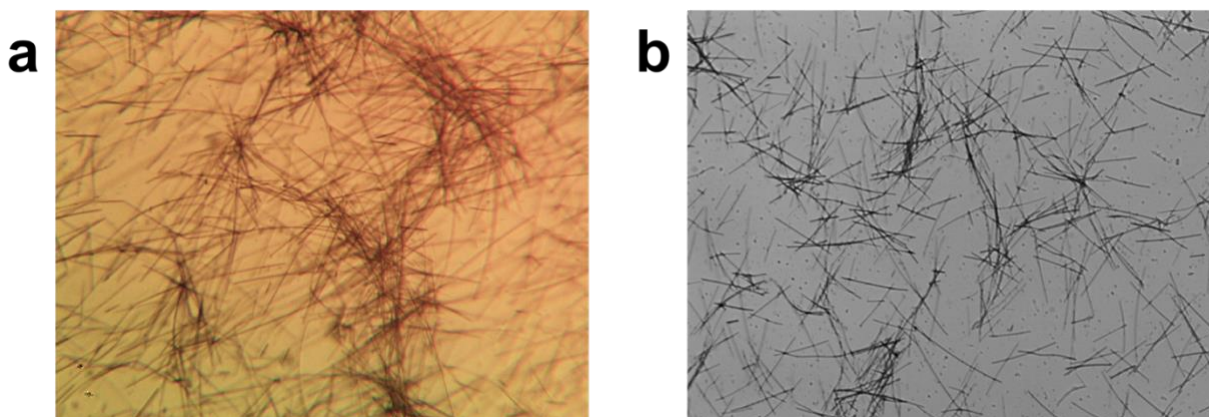


Figure 2.7 Optical images of AgNWs taken by (a) AmScope microscope with MU1000 digital camera at 40X magnification, showing synthesized long AgNWs and (b) Nikon Optiphot at 20X magnification showing short AgNWs.

However, it is also necessary to apply electron microscope imaging to get precise dimensions of the synthesized nanowires. We used the secondary electron imaging mode of JEOL JSM-6010LA to obtain SEM images (Figure 2.8 (a)). To prepare an SEM sample, 1.5 μm of AgNWs suspended in ethanol was drop cast onto carbon tape on an aluminum SEM mount. Once the sample is completely dried over an hour, it was sent to the SEM chamber without additional treatment with sputter coating. We also took series of SEM images with low magnifications for diluted AgNWs to reveal the length distribution of AgNWs. The nanowire lengths were measured and analyzed with ImageJ software. Segmented line measurement was used to measure each of the nanowires to accommodate their curvy nature. For example, when synthesizing AgNWs at 170°C for 25 min, the measured lengths of nanowires were in the range of 26.98 to 89.51 μm with an average of 49.53 μm (Figure 2.9 (a)). Statistics were collected from 15 SEM images showing 152 nanowires.

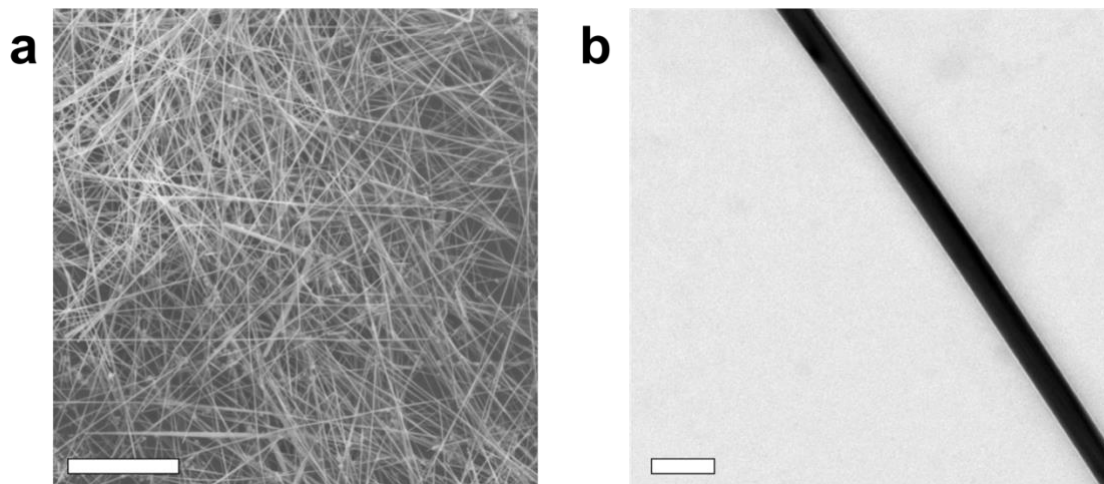


Figure 2.8 (a) An SEM image of AgNWs. Scale bar is 10 μm . (b) A TEM image of AgNWs for diameter measurements. Scale bar is 200 nm.

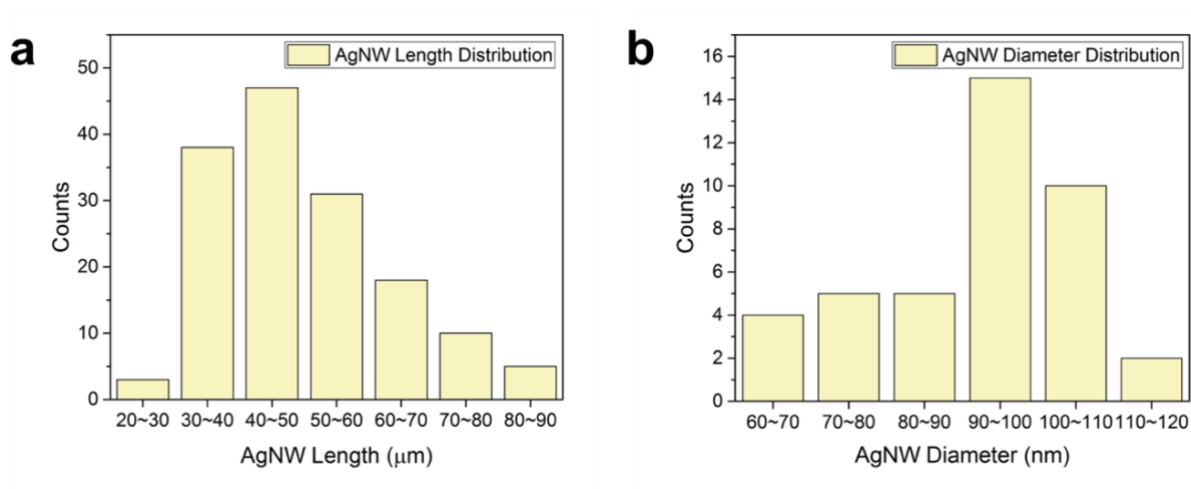


Figure 2.9 Using AgNWs synthesized at 170 $^{\circ}\text{C}$ for 25 min for example, (a) the length distribution of AgNWs is measured by ImageJ from SEM images, and (b) the diameter distribution of AgNWs is measured from TEM images.

In addition, we used JEOL JEM-2000FX and FEI Talos F200X to take TEM images of AgNWs. TEM imaging allows us to check the surface conditions of AgNWs and to obtain accurate

information on the nanowire diameters. AgNWs samples were drop cast and dried onto 200-mesh copper grids with a formvar film covered with a light layer of carbon (Ted Pella, 01800-F). They were then imaged at an accelerating voltage of 200 kV. Images of the ends of nanowires proved that the synthesized nanowires are pentagonal rods as previously reported^[77]. Using the same batch of AgNWs, a total of 41 nanowires were measured from 18 TEM images using ImageJ. Their diameters are in the range of 63.9 to 118.3 nm, with an average of 91.9 nm (Figure 2.9 (b)). Furthermore, we took a series of TEM images following a single AgNW, then processed the images with the MosaicJ plugin by ImageJ to stitch the images into one to reveal the curvature of AgNWs (Figure 2.10). We analyzed the curvature of AgNWs by calculating the ratio of the length of the nanowire to the distance between the two ends of the nanowire. We obtained an averaged ratio of 1.054, measured and calculated from 18 nanowires.

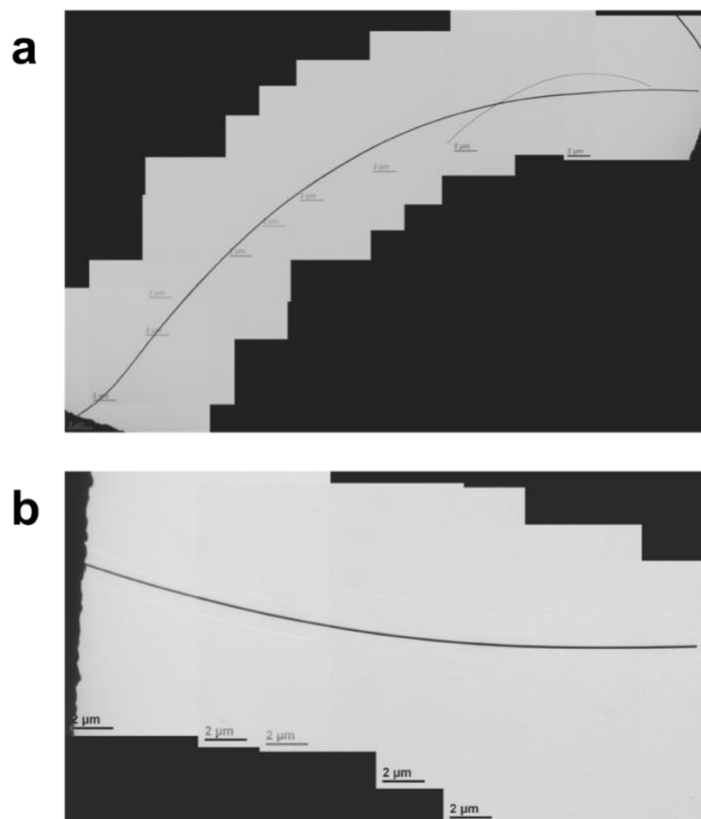


Figure 2.10 Stitched images of a single AgNW (a) from 10 TEM images and (b) from 5 TEM images for curvature calculation.

2.4 Conclusions and future directions

We performed a parametric study to determine the influence of major synthesis conditions on the dimensions of the final AgNW product. We especially investigated the influence of reaction temperature, reaction time, PVP chain length, and stirring condition. When using PVP as the capping agent for AgNW synthesis, we found that it is optimal to use a mixture of PVP (~55,000) and PVP (~360,000) in the mass ratio of 1:3 to support anisotropic growth and to prevent forming a foaming supernatant layer during the reaction. We also determined that magnetic stirring should be stopped at the beginning of the growth phase, where seeds are about to grow into the wire shape, to support growing long nanowires. Extended stirring during the growth phase was shown to

disturb the growth of long nanowires. We researched beyond the one-pot polyol-mediated procedures reported by Andres *et al.* and formulated a protocol to synthesize AgNWs using a hot plate or a thermostatic bath. Our robust method effectively produced AgNWs with an averaged length up to 68.1 μm . We also examined different reaction temperatures and durations to fabricate shorter AgNWs from 21 μm to 68.1 μm . Besides, we used UV-Vis spectroscopy and EDS for chemical characterization of the produced nanowires and proved their silver nature. We also used optical imaging, SEM, and TEM to visualize the nanowires. We used SEM images to measure the length distribution of AgNWs and used TEM images to analyze the diameters and curvatures of AgNWs.

One can continue this study by exploring other synthesis parameters and conditions. One direction is to study the type and concentration of each of the reagents in synthesis, such as the type of chlorinated derivatives as the nucleating agent and potential alternatives to ethylene glycol as the reducing agent. One can investigate how these factors influence the dimensions of the final AgNW product. Another direction is to continue the exploration of different synthesis setups for mass production. The possibility of utilizing novel instruments that are not traditionally used for solution-based nanomaterials synthesis can be evaluated (i.e. such as drug dissolution testing and analysis apparatus).

Bibliography

- [64] Gong, S.; Cheng, W. One-Dimensional Nanomaterials for Soft Electronics. *Adv. Electron. Mater.* **2017**, *3*, 1600314.
- [65] Deignan, G.; Goldthorpe, I. The Dependence of Silver Nanowire Stability on Network Composition and Processing Parameters. *RSC Adv.* **2017**, *7*, 35590.
- [66] Tan, D.; Jiang, C.; Li, Q.; Bi, S.; Song, J. Silver Nanowire Networks with Preparations and Applications: A Review. *J. Mater. Sci.: Mater. Electron.* **2020**, *31*, 15669-15696.
- [67] Wu, X.; Zhou, Z.; Wang, Y.; Li, J. Syntheses of Silver Nanowires Ink and Printable Flexible Transparent Conductive Film: A Review. *Coatings* **2020**, *10*, 865.
- [68] Shi, Y.; He, L.; Deng, Q.; Liu, Q.; Li, L.; Wang, W.; Xin, Z.; Liu, R. Synthesis and Applications of Silver Nanowires for Transparent Conductive Films. *Micromachines* **2019**, *10*, 330.
- [69] Hemmati, S.; Harris, M.T.; Barkey, D.P. Polyol Silver Nanowire Synthesis and the Outlook for a Green Process. *J. Nanomat.* **2020**, 2020.
- [70] Kumar, A.; Shaikh, M.O.; Chuang, C.-H. Silver Nanowire Synthesis and Strategies for Fabricating Transparent Conducting Electrodes. *Nanomaterials* **2021**, *11*, 693.
- [71] Rathmell, A.R.; Bergin, S.M.; Hua, Y.-L.; Li, Z.-Y.; Wiley, B.J. The Growth Mechanism of Copper Nanowires and Their Properties in Flexible, Transparent Conducting Films. *Adv. Mater.* **2010**, *22*, 3558–3563.
- [72] Zhang, D.; Wang, R.; Wen, M.; Weng, D.; Cui, X.; Sun, J.; Li, H.; Lu, Y. Synthesis of Ultralong Copper Nanowires for High-Performance Transparent Electrodes. *J. Am. Chem. Soc.* **2012**, *134*, 14283–6.
- [73] Lyons, P.E.; De, S.; Elias, J.; Schamel, M.; Philippe, L.; Bellew, A.T.; Boland, J.J.; Coleman, J.N. High-Performance Transparent Conductors from Networks of Gold Nanowires. *J. Phys. Chem. Lett.* **2011**, *2*, 3058–3062.
- [74] S´anchez-Iglesias, A.; Rivas-Murias, B.; Grzelczak, M.; P´erez-Juste, J.; Liz-Marz´an, L.M.; Rivadulla, F.; Correa-Duarte, M.A. Highly Transparent and Conductive Films of Densely Aligned Ultrathin Au Nanowire Monolayers. *Nano Lett.* **2012**, *12*, 6066–6070.
- [75] Ran, Y.; He, W.; Wang, K.; Ji, S.; Ye, C. A One-Step Route to Ag Nanowires with a Diameter Below 40 nm and an Aspect Ratio Above 1000. *Chem. Commun.* **2014**, *50*, 14877.
- [76] Sannicolo, T.; Lagrange, M.; Cabos, A.; Celle, C.; Simonato, J.-P.; Bellet, D. Metallic Nanowire-Based Transparent Electrodes for Next Generation Flexible Devices: a Review. *Small* **2016**, *12*, 6052-6075.

- [77] Langley, D.; Giusti, G.; Mayousse, C.; Celle, C.; Bellet, D.; Simonato, J.P.; Flexible Transparent Conductive Materials Based on Silver Nanowire Networks: A Review. *Nanotechnology* **2013**, *24*, 452001.
- [78] Chen, D.; Qiao, X.; Chen, J. Morphology-Controlled Synthesis of Silver Nanostructures Via a Solvothermal Method. *J. Mater. Sci.: Mater. Electron.* **2011**, *22*, 1335–9.
- [79] Bari, B.; Lee, J.; Jang, T.; Won, P.; Ko, S.H.; Alamgir, K.; Arshad, M.; Guo, L.J. Simple Hydrothermal Synthesis of Very-Long and Thin Silver Nanowires and Their Application in High Quality Transparent Electrodes. *J. Mater. Chem. A.* **2016**, *4*, 11365.
- [80] Gebeyehu, M.B.; Chala, T.F.; Chang, S.-Y.; Wu, C.-M.; Lee, J.-Y. Synthesis and Highly Effective Purification of Silver Nanowires to Enhance Transmittance at Low Sheet Resistance with Simple Polyol and Scalable Selective Precipitation Method. *RSC Adv.* **2017**, *7*, 16139.
- [81] Noroozi, M.; Zakaria, A.; Moxsin, M.M.; Wahab, Z.A.; Abedini, A. Nanostructures under Microwave Irradiation without Reducing Agent. *Int. J. Mol. Sci.* **2012**, *13*, 8086-8096.
- [82] Sun, Y.; Gates, B.; Mayers, B.; Xia, Y. Crystalline Silver Nanowires by Soft Solution Processing. *Nano Lett.* **2002**, *2*, 165-168.
- [83] Sun, Y.; Xia, Y. Large-Scale Synthesis of Uniform Silver Nanowires Through a Soft, Self-Seeding, Polyol Process. *Adv. Mater.* **2002**, *14*, 833–7.
- [84] Sun, Y.; Mayers, B.; Herricks, T.; Xia, Y. Polyol Synthesis of Uniform Silver Nanowires: A Plausible Growth Mechanism and the Supporting Evidence. *Nano Lett.* **2003**, *3*, 955–60.
- [85] Hu, M.; Gao, J.; Dong, Y.; Yang, S.; Li, R.K.Y. Rapid Controllable High-Concentration Synthesis and Mutual Attachment of Silver Nanowires. *RSC Adv.* **2012**, *2*, 2055–2060.
- [86] Andres, L.; Menendez, M.; Gomez, D.; Martinez, A.; Bristow, N.; Kettle J.; Menendez, A.; Ruiz, B. Rapid Synthesis of Ultra-Long Silver Nanowires for Tailor-Made Transparent Conductive Electrodes: Proof of Concept in Organic Solar Cells. *Nanotechnology* **2015**, *26*, 265201.
- [87] Bellew, A.T.; Manning, H.G.; de Rocha, C.G.; Ferreira, M.S.; Boland, J.J. Resistance of Single Ag Nanowire Junctions and Their Role in the Conductivity of Nanowire Networks. *ACS Nano* **2015**, *9*, 11422-11429.
- [88] Forró, C.; Demkó, L.; Weydert, S.; Vörös, J.; Tybrandt, K. Predictive Model for the Electrical Transport within Nanowire Networks. *ACS Nano* **2018**, *12*, 11080-11087.
- [89] Bobinger, M.; Dergianlis, V.; Becherer, M.; Lugli, P. Comprehensive Synthesis Study of Well-Dispersed and Solution-Processed Metal Nanowires for Transparent Heaters. *J. Nanomater.* **2018**, 2018.

- [90] Wang, Z.; Liu, J.; Chen, X.; Wan, J.; Qian, Y. A Simple Hydrothermal Route to Large-Scale Synthesis of Uniform Silver Nanowires. *Chem. Eur.* **2005**, *11*, 160-163.
- [91] Lee, J.H.; Lee, P.; Lee, D.; Lee, S.S.; Ko, S.H. Large-Scale Synthesis and Characterization of Very Long Silver Nanowires via Successive Multistep Growth. *Cryst. Growth Des.* **2012**, *12*, 5598–5605.
- [92] Lee, J.H.; Lee, P.; Lee, H.; Lee, D.; Lee, S.S.; Ko, S.H. Very Long Ag Nanowire Synthesis and its Application in a Highly Transparent, Conductive and Flexible Metal Electrode Touch Panel. *Nanoscale* **2012**, *4*, 6408.
- [93] Sun, Y.; Yin, Y.; Mayers, B.T.; Herricks, T.; Xia, Y. Uniform Silver Nanowires Synthesis by Reducing AgNO₃ with Ethylene Glycol in the Presence of Seeds and Poly (vinyl pyrrolidone). *Chem. Mater.* **2002**, *14*, 4736–4745.
- [94] Coskun, S.; Aksoy, B.; Unalan, H.E. Polyol Synthesis of Silver Nanowires: An Extensive Parametric Study. *Cryst. Growth Des.* **2011**, *11*, 4963–9.
- [95] Liu, S.; Sun, B.; Liu, J.; Chen, J. Silver Nanowires with Rounded Ends: Ammonium Carbonate-Mediated Polyol Synthesis, Shape Evolution and Growth Mechanism. *Cryst. Eng. Comm.* **2014**, *16*, 244-251.
- [96] Gao, Y.; Jiang, P.; Liu, D.F.; Yuan, H.J.; Yan, X.Q.; Zhou, Z.P.; Wang, J.X.; Song, L.; Liu, L.F.; Zhou, W.Y.; Wang, G.; Wang, C.Y.; Xie, S.S.; Zhang, J.M.; Shen, D.Y. Evidence for the Monolayer Assembly of Poly(vinylpyrrolidone) on the Surfaces of Silver Nanowires. *J. Phys. Chem. B.* **2004**, *108*, 12877–81.
- [97] Zhu, J.J.; Kan, C.X.; Wan, J.G.; Han, M.; Wang, G.H. High-Yield Synthesis of Uniform Ag Nanowires with High Aspect Ratios by Introducing the Long-Chain PVP in an Improved Polyol Process. *J. Nanomater.* **2011**, *2011*, 1-7.

CHAPTER 3

Two-Dimensional Silver Nanowire Networks on Glass Substrate

3.1 Introduction and background

3.1.1 Two-dimensional silver nanowire-based films

Most studies on two-dimensional (2D) silver nanowire- (AgNW) based films look into their applications in optoelectronic devices, such as touch panels, solar cells, and thin-film heaters^[98-99]. AgNW-based conductive and transparent films are seen as a great candidate to take the place of indium-doped tin oxide (ITO) that are traditionally used in these applications. ITO materials have suffered from expensive production costs, and their brittle nature makes them undesirable for applications in flexible electronics^[95]. Thus, the research on AgNW films made with inexpensive methods surged in recent years. However, these studies have a limited focus on enhancing the conductivity, transparency, and flexibility of the films, and an in-dept investigation on their electrical performance beyond conductivity has been missing.

3.1.2 Fabrication methods for silver nanowire-based films

Commonly, 2D AgNW-based films are made by solution deposition on various substrates. Some studies deposit AgNWs in certain patterns to optimize the optical transparency of the films for applications in transparent conducting electrodes (TCE). These studies are motivated to form conductive pathways with AgNW networks while maximizing the uncovered areas between nanowires^[100-101]. In other studies, AgNW networks are randomly deposited onto the substrate without any controlled patterns. In general, the following deposition methods can be used to fabricate 2D films with randomly oriented AgNW networks: spin coating, drop casting, inkjet printing, blade coating, Mayer rod coating, and vacuum filtration processing.

Spin coating is a convenient method that uniformly spreads a volume of AgNW solution with centrifugal force when it is dropped on a spinning substrate. The final thickness, transparency, and conductivity of the AgNW film are directly related to the controllable spinning rate and the dimensions of AgNWs^[102-103]. Spin coating effectively improves upon the disadvantage of the drop casting method that may form an uneven distribution of AgNWs due to the coffee-ring effect^[104]. In the drop casting method, the AgNW solution is dropped onto the substrate without a spin coater. Often times, a pretreatment for the substrate surface, such as plasma cleaning, is required to assist the uniform distribution of AgNWs when utilizing drop casting^[105-106]. Another common method to fabricate AgNW films is inkjet printing. Like the other printing methods, the final film conditions from inkjet printing are mainly controlled by the parameters related to the nozzle and the properties of the AgNW solution. Inkjet printing is especially suitable for AgNWs in the smaller range of dimensions ($D \sim 10 \mu\text{m}$)^[107-108]. Furthermore, another way to spread the AgNW solution uniformly onto a substrate is by using a blade or a Mayer rod at a fixed height above the substrate surface. Both methods have high requirements for the AgNW solution in order to construct homogeneous and scalable films^[109]. The Mayer rod method is especially suitable to coat large surfaces and is often used to make AgNW films with larger surface areas ($W \sim 20 \text{ cm}$)^[110-111]. Last but not least, vacuum filtration is another method to transfer AgNWs onto the substrate. It involves two steps—AgNW networks are first left on a filter paper after the AgNW solution goes through the vacuum filtration process, then the networks are transferred and printed onto the target substrate^[112-113]. This method has the advantage of filtering out unwanted nanoparticle impurities with the solvent before the network is transferred to a substrate, but it also has the disadvantage of losing a larger amount of materials during processing.

3.1.3 Project Overview

In this project, we would like to explore the fabrication and characterization of 2D AgNW networks built by AgNWs with different surface modifications, because they may display more interesting electrical behaviors than do simple conducting electrodes. Specifically, we utilized AgNWs with and without polyvinylpyrrolidone (PVP) coatings, as well as Ag-Ag₂S core-shell nanowires. The Ag-PVP-Ag structure can exhibit resistive switching properties with an applied electric field as a result of ionic transport of silver and filament growth through the PVP layer between two AgNWs^[114,115,116,117,118]. To further investigate this interesting behavior and perhaps make use of it for neuromorphic computing applications, we would like to compare the electrical responses between 2D networks comprising AgNWs with PVP coatings and networks of bare AgNWs without PVP coatings. We also sulfurized nanowire surfaces to fabricate Ag-Ag₂S core-shell nanowires that were combined with AgNWs to build 2D networks. Beyond that, we experimented with different fabrication methods to deposit 2D networks on the glass substrate, including spin coating, drop casting, blade coating, and dip coating. We determined that the spin coating method works the best with our electrical measurement setup and adopted this method to effectively make evenly distributed nanowire networks that were later characterized by current-voltage (IV) curve measurements.

3.2 Surface modifications of silver nanowires

3.2.1 Silver nanowires with and without PVP coatings

The electrical performance of AgNWs and AgNW networks is directly related to their surface coatings, since these coating will directly affect contact resistance between neighboring nanowires. One common coating to AgNWs is PVP. Using our one-pot polyol method described

in Chapter 2, as-synthesized AgNWs naturally have a nanometers-thick PVP residual coating^[119,120,121]. It has been reported that the PVP coating is between 1.5-3 nm in thickness and covers the entire surface of AgNWs^[122-123]. It is generally believed that the PVP layer can be washed off when AgNWs go through several purification cycles with ethanol and acetone, where acetone can remove PVP as well as other residues from synthesis^[124-125].

Since the studies of AgNW films for TCE applications are highly motivated to enhance the current flow in the AgNW networks, these studies commonly adapt post-deposition treatments such as annealing the percolating network at high temperature or intense pulsed ion beam irradiation to remove the PVP coatings and to fuse nanowire-nanowire connections in order to lower nanowire junction resistance^[126,127,128,129,130]. In our project, we would like to explore the nonlinear properties of a network built with AgNWs with insulating PVP coatings, therefore we would like to preserve the PVP coatings from synthesis for such purposes. Diaz-Alvarez *et al.* found that the PVP layer can be preserved if AgNWs are purified with isopropanol and DI water^[109]. We adopted these purification solvents when it is desired to keep the PVP coating over the nanowire surface. In contrast, our other goal is to perform the same electrical measurements with AgNWs that do not have PVP coatings as a control group. We simply used purification with ethanol and acetone to take off PVP coatings to prepare nanowires for these measurements. We did not apply any additional treatment to fuse nanowires junctions together as that would change the network connectivity of the control group.

3.2.2 Ag-Ag₂S core-shell nanowires

Another type of surface modification of AgNWs we explored is to sulfurize AgNWs with sulfur particles to fabricate nanowires with silver core and silver sulfide shell. We will refer to such nanowires as silver sulfide nanowires (Ag₂S NWs) in the following. Ag₂S is a narrow-

bandgap semiconducting material and has great chemical stability^[131]. Resistive switching has been observed from the structure of Ag-Ag₂S-Ag^[132-133], thus nanostructured silver sulfide materials are often prepared with silver in the form of Ag-Ag₂S heterostructures to harvest their resistance switching properties for applications in nonvolatile memory devices^[134,135,136]. Such heterostructures include Ag-Ag₂S heterojunction nanowires^[137 - 138], Ag-Ag₂S core-shell nanoparticles^[139-140], as well as Ag-Ag₂S core-shell nanowires, which is what we fabricated in this project.

We prepared Ag₂S NWs based on a modified method reported by Xiong, *et al*^[129] using sulfur particles and AgNWs purified with ethanol and acetone as described earlier. Specifically, the stoichiometric amounts of sulfur particles and AgNWs are first separately suspended in ethanol. Then, the solutions are combined and mixed at an elevated temperature (~60°C). Once the sulfurization process is complete, Ag₂S NWs are washed with ethanol to remove any potentially unreacted sulfur particles in the solution, and the final materials are suspended in ethanol for future use^[141]. The microscopy characterization of Ag₂S NWs is shown in Figure 3.1. We found that AgNWs broke into shorter nanowires during sulfurization with bumpy sulfur and Ag₂S islands on the surfaces. The average diameter of Ag₂S NWs is 135.4 nm, measured from 152 nanowires recorded by transmission electron microscopy (TEM) images. The average length of Ag₂S NWs is 25 μm, measured from scanning electron microscopy (SEM) images. For observed distributions of measured lengths and diameters see Figure 2.9, above. We also analyzed the nanowires with energy dispersive spectroscopy (EDS), as shown in Figure 3.2.

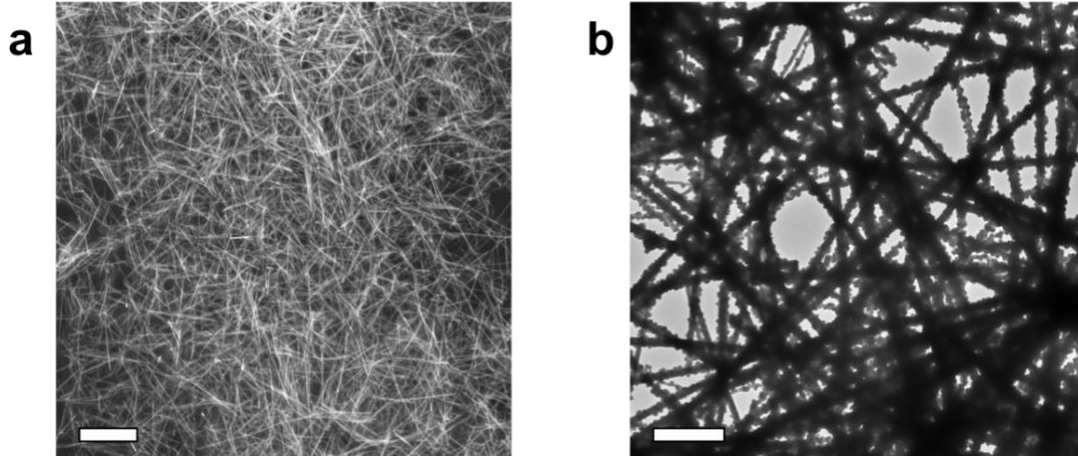


Figure 3.1 (a) Scanning electron microscopy (SEM) and (b) transmission electron microscopy (TEM) images of Ag_2S NWs. Scale bars are $10\ \mu\text{m}$ and $1\ \mu\text{m}$, respectively. Figure 3.1 (b) was taken by Mahshid Hosseini, used with permission.

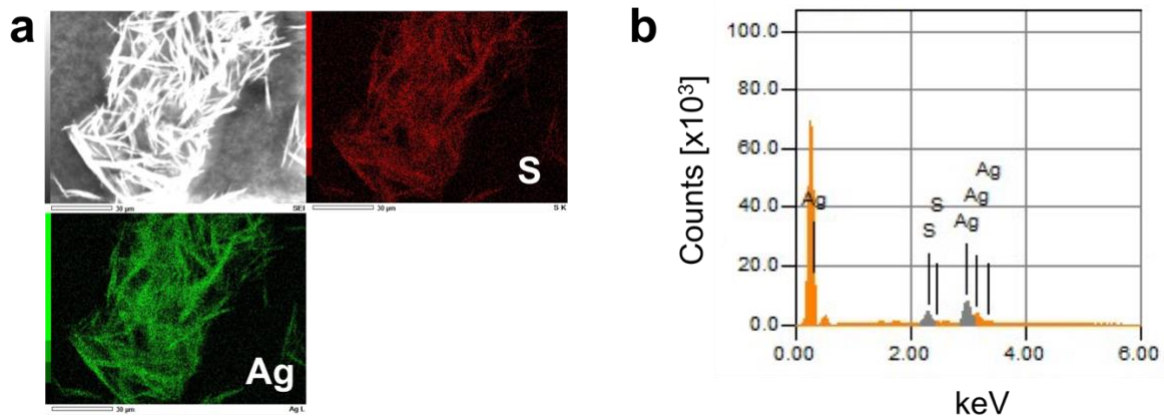


Figure 3.2 (a) EDS element mapping of Ag_2S NWs, and (b) EDS spectrum of the detected area.

3.3 Fabrication of two-dimensional silver nanowire networks

We explored several common methods to deposit AgNWs onto a flat substrate: blade coating, dip coating, drop casting, and spin coating. When we first applied the blade coating technique for the glass microscope slide surface, we found that it is essential to control to flow of

the AgNW solution and the height and angle of the blade to be able to coat the substrate evenly. Due to the manual factors during coating, we found it more difficult to produce films with an even distribution of nanowires and to maintain a high reproducibility with the blade method. Besides, it is also harder to tune the surface fraction of the glass substrate covered by AgNWs with blade coating, so we moved on to examine dip coating. While dip coating shows a better nanowire distribution compared to blade coating, we found that it is more vulnerable to any potential impurities in the AgNW solution and the particle impurities tend to remain on the edge of the glass substrate after drying. Also, there is a waste of material from dip coating, and it is also more difficult to control and reproduce the final surface fraction of nanowires. Due to these reasons, we moved on to test drop casting. With drop casting, it is more convenient to aim at the target area (near or between electrodes, for example) and to control the final surface fraction of AgNWs. However, we experienced the coffee-ring effect from drop casting, with a very high concentration of nanowires trapped in the outer circumference of the drop. Although we could manually erase the perimeter of the coated area, this post-deposition process may alter the nanowire networks and thus is not ideal. Therefore, after exploring different types of deposition methods, we chose spin coating to create 2D nanowire networks.

To deposit nanowire networks on the glass substrate, we first cleaned the microscope glass slide with ethanol and acetone, then rinsed it with DI water. After the glass slide substrate was completely dried, we placed it in a plasma cleaner (Harrick Plasma, PDC-32G) and allowed 1 min of plasma treatment. Once the substrate was cleaned and treated, it was placed on a spin coater (Instras Scientific, SCK-300P, shown in Figure 3.3). The vacuum system was then turned on to secure the substrate on the coater. Then, the spin coater was started at a low rotational speed (250 rpm), and the desired volume of AgNW or AgNW/Ag₂S NW solution (15-20 μ L) was dropped on

the substrate, aiming at the center of the coater. Then, we adjusted the spinning setup to the desired rotational speed (850-1000 rpm) to spread the solution. The coater was stopped after the solvent evaporates, and a uniform network was left on the surface of the glass substrate. The surface fraction of the final network is controlled by the initial concentration of the AgNW solution and the spinning settings. After a nanowire network was formed, the transparency of multiple spots of the substrate was examined with a broad spectral range spectrometer (ASEQ Instruments, LR1-B) to ensure that the network is uniformly distributed on the substrate.



Figure 3.3 The spin coating setup.

3.4 Electrical characterization

3.4.1 IV curve measurements of silver nanowire with and without PVP coatings

We explored the IV curve characterization of AgNW networks composed of AgNWs with different surface conditions: AgNWs with PVP coatings, bare AgNWs without PVP coatings, and a mixture of nanowires that have Ag cores with Ag₂S surfaces (Ag-Ag₂S core-shell nanowires) and AgNWs without PVP coatings. For IV curve measurements, a 2D AgNW network with one type of the above surfaces was first deposited onto a glass substrate using the method described in section 3.3. Then, the glass substrate with deposited network was contacted with two parallel line

electrodes made by copper that have a fixed gap distance between 1-5 mm by clamping the glass substrate over the electrodes with fixed pressure. The electrodes were connected to a two-channel source/monitor unit module (Agilent Technologies E5272A), and the glass substrate with sample was placed inside a Faraday cage (Hewlett Packard Test Fixture Analyzer 16058A) during measurements to block interference from the external environment.

First of all, we compared the 2D networks composed of AgNWs with and without PVP coatings using IV curve measurements. We also explored with both long AgNWs with an average length of 49.5 μm (referred to as “long AgNWs” in the following) and short AgNWs with an average length of 25.7 μm (referred to as “short AgNWs” in the following) to fabricate the networks. In either case, AgNWs synthesized from the same batch (i.e. and thus with the same dimensional conditions) were purified separately in two conditions—half of the batch was washed with ethanol and acetone to take off the PVP coating in order to obtain bare AgNWs, and the other half of the batch was washed with isopropanol and DI water to reserve the PVP layer to obtain AgNWs with PVP coatings. The final AgNW solutions were all adjusted to the same concentration of 0.75 mg/mL. Then, the four types of AgNW networks made with (i) long AgNWs with PVP coatings, (ii) long AgNWs without PVP coatings, (iii) short AgNWs with PVP coatings, and (iv) short AgNWs without PVP coatings were characterized using IV curve measurements. For each network, we applied 10 consecutive positive and negative voltage pulses at either 5 V or 10 V and recorded the current outputs. The IV responses of networks built with long AgNWs with and without PVP coatings are shown in Figure 3.4, and the IV responses of networks built with short AgNWs with and without PVP coatings are shown in Figure 3.5.

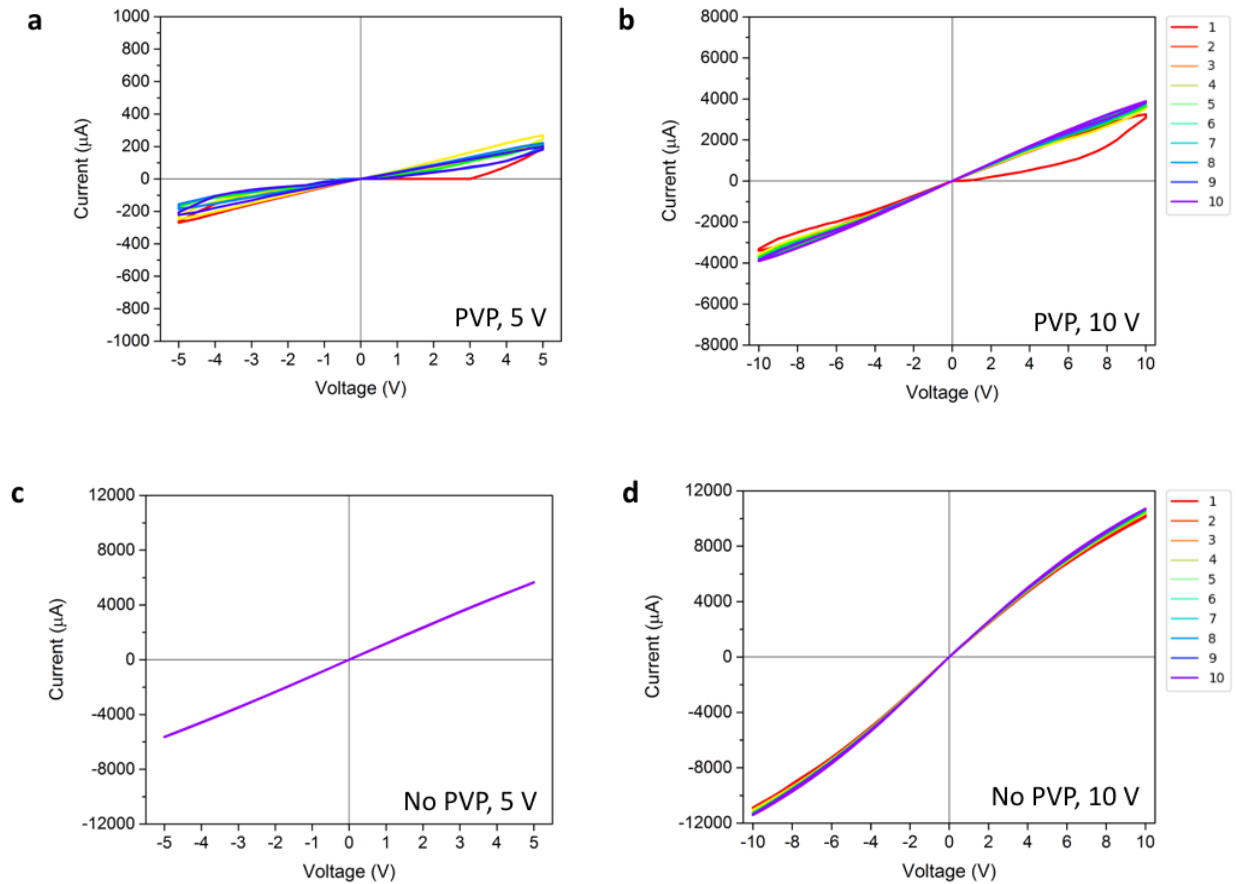


Figure 3.4 IV curve measurements of AgNW networks built by long AgNWs (a-b) with and (c-d) without PVP coatings. (a, c) were recorded with voltage pulses at ± 5 V, while (b, d) were recorded with pulses at ± 10 V. Legends show the pulse number.

As shown in Figure 3.4, we observed that 2D AgNW networks with PVP coatings exhibit hysteresis loops and variation in the resistance at different given pulses. The PVP coatings served as an insulating layer where Ag ion migrations took place and conductive filaments formed. From Figure 3.4 (a), it is likely that different current pathways from the network were activated and recorded during different voltage pulses. In addition, the network composed of AgNWs without PVP coatings showed higher conductivities than networks composed of AgNWs with PVP coatings, which agrees with previous TCE studies that the PVP layer hinders the performance of

AgNWs in building a highly conductive 2D film. Although we didn't anneal the AgNW junctions or provide any other post-treatments as the reported TCE studies, we proved that we can still increase the conductivity of the nanowire network merely by taking off the PVP layer. Furthermore, we also observed that at this low nanowire concentration, AgNWs without PVP coatings also exhibit a slight tendency towards nonlinearity with high supplied voltage pulses (Figure 3.4 (d)).

The overall observations from networks of long AgNWs echo with the observations from networks of short AgNWs with and without PVP coatings (Figure 3.5). We first prepared AgNW solution with short nanowires that has the same concentration as the long AgNW nanowire (0.75 mg/mL). However, a deposited nanowire film from this concentration did not reach percolation as the short nanowires were not able to effectively build percolation pathways. Then, we increased the solution concentration to 1 mg/mL, and the IV responses of a network deposited from this concentration were recorded in Figure 3.5 (a-b). Similar to the IV curves from long AgNWs with PVP coatings, the ones measured from short AgNWs with PVP also exhibit resistive switching in response to different voltage pulses. We then characterized short AgNW without PVP coatings from the same solution concentration as the long AgNWs (0.75 mg/mL). As expected, we observed a decrease in the conductivity of the network built from short AgNWs (Figure 3.5 (c-d)). The tendency towards nonlinearity at higher voltage pulses was also observed from the network built with short AgNWs without PVP coatings (Figure 3.5 (d)).

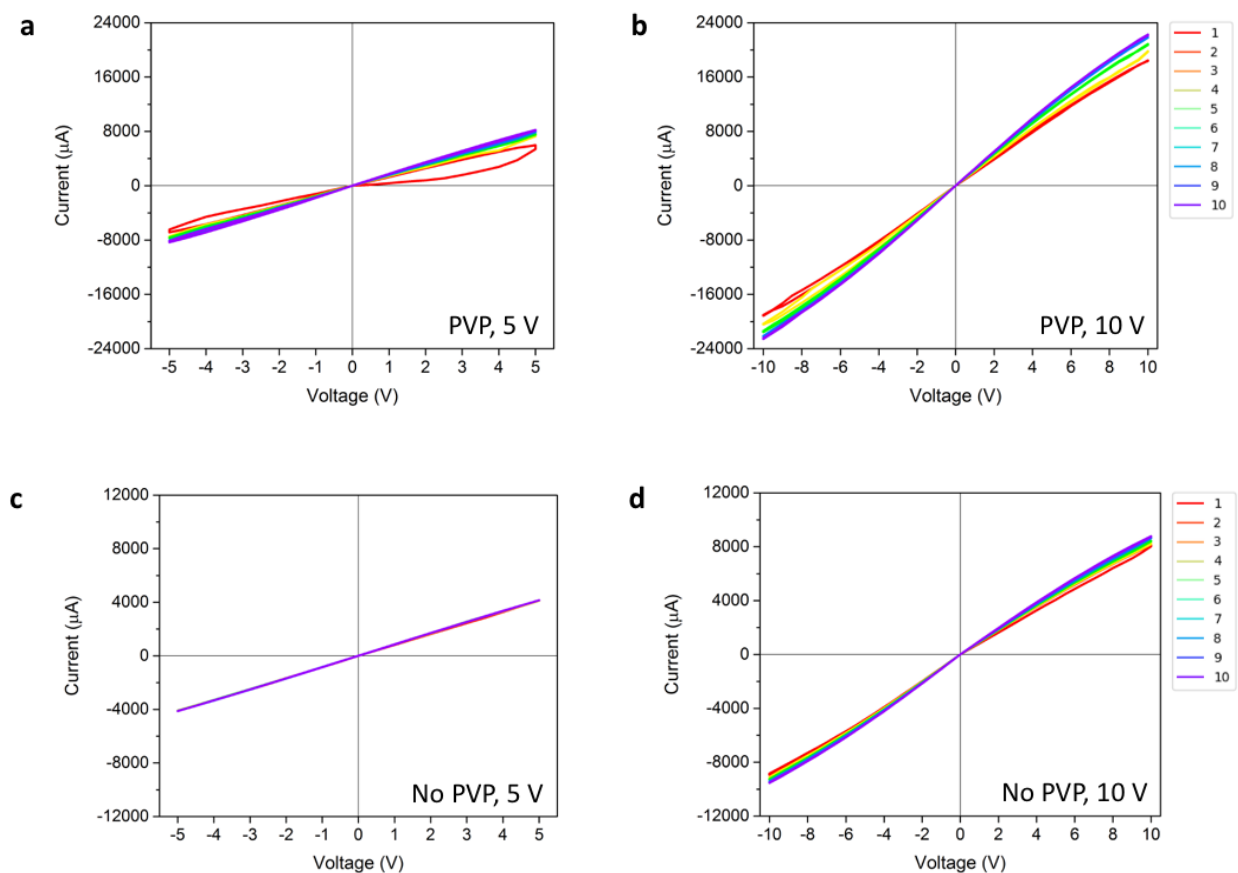


Figure 3.5 IV curve measurements of AgNW networks built by short AgNWs (a-b) with and (c-d) without PVP coatings. (a-b) The networks were deposited from solution with the concentration of 1 mg/mL and (c-d) was from solution with concentration of 0.75 mg/mL. (a, c) were recorded with voltage pulses at ± 5 V, while (b, d) were recorded with pulses at ± 10 V. Legends show the pulse number.

3.4.2 IV curve measurements of silver nanowire and silver-silver sulfide core-shell nanowires

After examining the networks built with AgNWs with and without PVP coatings, we prepared and examined 2D networks that combined AgNWs and Ag-Ag₂S core-shell nanowires in the mass ratio of 1:10. We used the same setup and testing conditions to run IV curve

measurements. The goal of this study is to provide preliminary observations for the electrical measurement of 3D composites comprised of AgNWs and Ag₂S NWs.

As shown in Figure 3.6, the 2D network of AgNWs and Ag₂S NWs also exhibited nonlinear behaviors. Here, similar to the PVP coating, the Ag₂S layer between AgNWs structure enables tunneling of Ag ions and the formation of conductive filaments through the Ag₂S layer under an applied voltage, which was shown by the current fluctuations and the narrow hysteresis loops from the IV curves. This nonlinear behavior has previously been observed and reported by studies on the individual Ag-single Ag₂S-Ag structure^[142]. Unlike the observations from single Ag₂S device, the network of Ag-Ag₂S-Ag configuration we fabricated using nanowires did not exhibit a sharp switching process showing by the significant difference in sweeping cycles. With that being said, the current increased slightly after the first positive and negative sweep, indicating the switching-on process. The IV curve responses of this 2D network will be compared later in Chapter 4 with the electrical behaviors of our 3D AgNW-Ag₂SNW networks embedded in polymer-based composites.

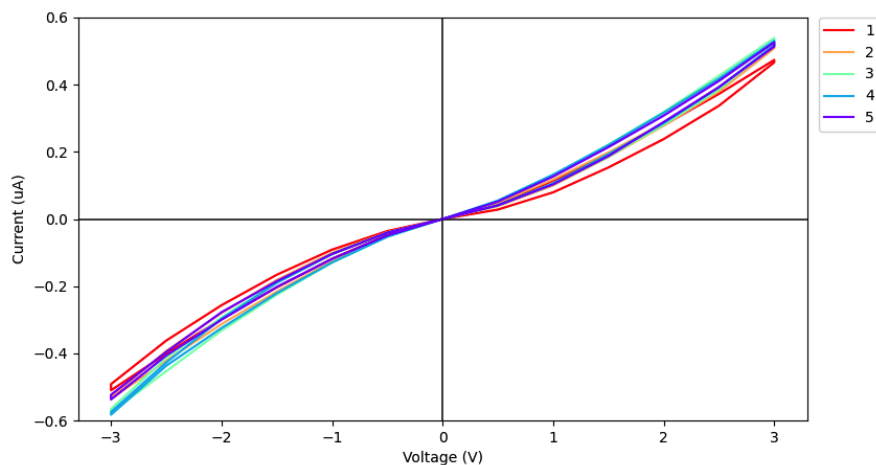


Figure 3.6 IV curves of a 2D network built by AgNWs and Ag₂S NWs. Legend shows the pulse number.

3.5 Conclusions and future directions

As a summary, we studied the deposition and characterization of 2D AgNW networks on the glass substrate and the influence of nanowire lengths on the conductivity of the final networks. We measured and compared networks of AgNW with different surface conditions: with and without PVP coatings, and with Ag₂S shells. We examined the final 2D nanowire network conditions fabricated from spin coating, drop casting, dip coating, and blade coating. Among these deposition methods, we observed that spin coating demonstrated the best performance in fabricating a homogeneous nanowire network. Therefore, we used spin coating to fabricate AgNW-based networks on glass substrates and explored the conductivity and nonlinearity of the Ag-PVP-Ag and Ag-Ag₂S-Ag structures with IV curve measurements. We observed that a network comprised of AgNWs without PVP coatings showed increased conductivity compared to a network at the same concentration comprised of AgNWs with PVP coatings. Besides, the IV curve measurements showed that it was likely different current pathways were taken at different given pulses from the networks of AgNWs with PVP coatings. This study serves as the first step towards the investigation of 3D nanowire networks that will be reported in reported in Chapter 4.

As a future step to this project, one can explore the relationship between the surface fraction of the glass substrate covered by a AgNW network and the conductivity of the network. For this study, one can continue to use a spectrometer to measure transmission or analyze microscopy images to characterize the surface fraction covered by nanowires. Then, a four-point probe system designed to measure sheet resistivity can be used to test the surface conductivity of the network. In addition, one can further formulate the relationship between the concentration of AgNW in the solution and the surface fraction of the 2D AgNW network once the nanowires are deposited on the glass substrate. This study will also allow fellow researchers to verify the uniform deposition

of nanowires. Last but not least, another further step of this project is to tune the ratio of AgNWs and Ag₂S NWs being used to make a combined network. One can study how the amount of Ag₂S NWs influences the electrical behavior of the combined network.

Bibliography

- [98] Langley, D.; Giusti, G.; Mayousse, C.; Celle, C.; Bellet, D.; Simonato, J.P.; Flexible Transparent Conductive Materials Based on Silver Nanowire Networks: A Review. *Nanotechnology* **2013**, *24*, 452001.
- [99] Wu, X.; Zhou, Z.; Wang, Y.; Li, J. Syntheses of Silver Nanowires Ink and Printable Flexible Transparent Conductive Film: A Review. *Coatings* **2020**, *10*, 865.
- [100] Kumar, A.; Shaikh, M.O.; Chuang, C.-H. Silver Nanowire Synthesis and Strategies for Fabricating Transparent Conducting Electrodes. *Nanomaterials* **2021**, *11*, 693.
- [101] Chu, X.; Wang, K.; Tao, J.; Li, S.; Ji, S.; Ye, C. Tackling the Stability Issues of Silver Nanowire Transparent Conductive Films through FeCl₃ Dilute Solution Treatment. *Nanomaterials* **2019**, *9*, 533.
- [102] He, X.; He, R.; Chen, X.; Zhao, Z.; Feng, S.; Chen, N.; Zhang, M. A Highly Conductive, Flexible, Transparent Composite Electrode based on the Lamination of Silver Nanowires and Polyvinyl Alcohol. *J. Mater. Chem. C* **2014**, *2*, 9737–9745.
- [103] Leem, D.S.; Edwards, A.; Faist, M.; Nelson, J.; Bradley, D.D.C.; De Mello, J.C. Efficient Organic Solar Cells with Solution-Processed Silver Nanowire Electrodes. *Adv. Mater.* **2011**, *23*, 4371–4375.
- [104] Koga, H.; Nogi, M.; Komoda, N.; Nge, T.T.; Sugahara, T.; Suganuma, K. Uniformly Connected Conductive Networks on Cellulose Nanofiber Paper for Transparent Paper Electronics. *NPG Asia Mater.* **2014**, *6*, e93.
- [105] Hong, C.-H.; Oh, S.K.; Kim, T.K.; Cha, Y.-J.; Kwak, J.S.; Shin, J.-H.; Ju, B.-K.; Cheong, W.-S. Electron Beam Irradiated Silver Nanowires for a Highly Transparent Heater. *Sci. Rep.* **2015**, *5*, 17716.
- [106] Chen, Y.; Carmichael, R.S.; Carmichael, T.B. Patterned, Flexible, and Stretchable Silver Nanowire/Polymer Composite Films as Transparent Conductive Electrodes. *ACS Appl. Mater. Interfaces* **2019**, *11*, 31210–31219.
- [107] Maisch, P.; Tam, K.C.; Lucera, L.; Egelhaaf, H.-J.; Scheiber, H.; Maier, E.; Brabec, C.J. Inkjet Printed Silver Nanowire Percolation Networks as Electrodes for Highly Efficient Semitransparent Organic Solar Cells. *Org. Electron.* **2016**, *38*, 139-143.
- [108] Lu, H.; Lin, J.; Wu, N.; Nie, S.; Luo, Q.; Ma, C.-Q.; Cui, Z. Inkjet Printed Silver Nanowire Network as Top Electrode for Semitransparent Organic Photovoltaic Devices. *Appl. Phys. Lett.* **2015**, *106*, 093302.
- [109] Krantz, J.; Richter, M.; Spallek, S.; Spiecker, E.; Brabec, C.J. Solution-Processed Metallic Nanowire Electrodes as Indium Tin Oxide Replacement for Thin-Film Solar Cells. *Adv. Funct. Mater.* **2011**, *21*, 4784-4787.

- [110] Junaidi; Triyana, K.; Harsojo; Suharyadi, E. High-Performance Silver Nanowire Film on Flexible Substrate Prepared by Meyer-rod Coating. *IOP Conf. Ser.: Sci. Eng.* **2017**, *202*, 012055.
- [111] Cho, S.; Kang, S.; Pandya, A.; Shanker, R.; Khan, Z.; Lee, Y.; Park, J.; Craig, S.L.; Ko, H. Large-Area Cross-Aligned Silver Nanowire Electrodes for Flexible, Transparent, and Force-Sensitive Mechanochromic Touch Screens. *ACS Nano* **2017**, *11*, 4346–4357.
- [112] Xu, W.; Xu, Q.; Huang, Q.; Tan, R.; Shen, W.; Song, W. Fabrication of Flexible Transparent Conductive Films with Silver Nanowire by Vacuum Filtration and PET Mold Transfer. *J. Mater. Sci. Technol.* **2016**, *32*, 158–161.
- [113] Kisannagar, R.R.; Jha, P.; Navalkar, A.; Maji, S.K.; Gupta, D. Fabrication of Silver Nanowire/Polydimethylsiloxane Dry Electrodes by a Vacuum Filtration Method for Electrophysiological Signal Monitoring. *ACS Omega* **2020**, *5*, 10260–10265.
- [114] Wu, S.; Tsuruoka, T.; Terabe, K.; Hasegawa, T.; Hill, J.P.; Ariga, K.; Aono, M. A Polymer-Electrolyte-Based Atomic Switch. *Adv. Funct. Mater.* **2011**, *21*, 93–99.
- [115] Sandouk, E.J., Gimzewski, J.K. Stieg, A.Z. Multistate Resistive Switching in Silver Nanoparticle Films. *Sci. Technol. Adv. Mater.* 2015, *16*.
- [116] Diaz-Alvarez, A.; Higuchi, R.; Sanz-Leon, P.; Marcus, I.; Shingaya, Y.; Stieg, A.Z.; Gimzewski, J.K.; Kuncic, Z.; Nakayama, T. Emergent Dynamics of Neuromorphic Nanowire Networks. *Sci. Rep.* **2019**, *9*, 14920.
- [117] White, S.I.; Vora, P.M.; Kikkawa, J.M.; Winey, K.I. Resistive Switching in Bulk Silver Nanowire-Polystyrene Composites. *Adv. Funct. Mater.* **2011**, *21*, 233–240.
- [118] Bellew, A.T., Bell, A.P., McCarthy, E.K., Fairfield, J.A. Boland, J.J. Programmability of Nanowire Networks. *Nanoscale* **2014**, *6*, 9632–9639.
- [119] Zhan, K.; Su, R.; Bai, S.; Yu, Z.; Cheng, N.; Wang, C.; Xu, S.; Liu, W.; Guo, S.; Zhao, X.-Z. One-Pot Stirring-Free Synthesis of Silver Nanowires with Tunable Lengths and Diameters via a Fe³⁺ & Cl⁻-co-Mediated Polyol Method and Their Application as Transparent Conductive Films. *Nanoscale* **2016**, *8*, 18121–18133.
- [120] Gao, Y.; Jiang, P.; Liu, D.F.; Yuan, H.J.; Yan, X.Q.; Zhou, Z.P.; Wang, J.X.; Song, L.; Liu, L.F.; Zhou, W.Y.; Wang, G.; Wang, C.Y.; Xie, S.S.; Zhang, J.M.; Shen, D.Y. Evidence for the Monolayer Assembly of Poly(vinylpyrrolidone) on the Surfaces of Silver Nanowires. *J. Phys. Chem. B.* **2004**, *108*, 12877–81.
- [121] Zhang, R.; Engholm, M. Recent Progress on the Fabrication and Properties of Silver Nanowire-Base Transparent Electrodes. *Nanomaterials* **2018**, *8*, 628.

- [122] Azani, M.-R.; Hassanpour, A.; Plaia, N.; Meshkat-Mamalek, M. Movement-Reactor Oven and Wire Mesh Filter for Large-Scale Solvothermal Preparation and Purification of Silver Nanowires with High Uniformity in Length and Diameter for the Fabrication of Low and High Haze Transparent Conductive Films. *Nanoscale Adv.* **2019**, *1*, 2732-2739.
- [123] Hwang, J.; Shim, Y.; Yoon, S.-M.; Lee, S.H.; Park, S.-H. Influence of Polyvinylpyrrolidone (PVP) Capping Layer on Silver Nanowire Networks: Theoretical and Experimental Studies. *RSC Adv.* **2016**, *6*, 30972–30977.
- [124] Gebeyehu, M.B.; Chala, T.F.; Chang, S.-Y.; Wu, C.-M.; Lee, J.-Y. Synthesis and Highly Effective Purification of Silver Nanowires to Enhance Transmittance at Low Sheet Resistance with Simple Polyol and Scalable Selective Precipitation Method. *RSC Adv.* **2017**, *7*, 16139.
- [125] Wang, J.; Jiu, J.; Araki, T.; Nogi, M.; Sugahara, T.; Nagao, S.; Koga, H.; He, P.; Suganuma, K. Silver Nanowire Electrodes: Conductivity Improvement Without Post-Treatment and Application in Capacitive Pressure Sensors. *Nano-Micro Lett.* **2015**, *7*, 51–58.
- [126] Bellew, A.T.; Manning, H.G.; de Rocha, C.G.; Ferreira, M.S.; Boland, J.J. Resistance of Single Ag Nanowire Junctions and Their Role in the Conductivity of Nanowire Networks. *ACS Nano* **2015**, *9*, 11422-11429.
- [127] Langley, D.P.; Lagrange, M.; Giusti, G.; Jiménez, C.; Bréchet, Y.; Nguyen, N.D.; Bellet, D. Metallic Nanowire Networks: Effects of Thermal Annealing on Electrical Resistance. *Nanoscale* **2014**, *6*, 13535–13543.
- [128] Deignan, G.; Goldthorpe, I. The Dependence of Silver Nanowire Stability on Network Composition and Processing Parameters. *RSC Adv.* **2017**, *7*, 35590.
- [129] Kaikanov, M.; Amanzhulov, B.; Demeuova, G.; Akhtanova, G.; Bozheyev, F.; Kemelbay, A.; Tikhonov, A. Modification of Silver Nanowire Coatings with Intense Pulsed Ion Beam for Transparent Heaters. *Nanomaterials* **2020**, *10*, 2153.
- [130] Kim, C.-L.; Lee, J.-Y.; Shin, D.-G.; Yeo, J.-S.; Kim, D.-E. Mechanism of Heat-Induced Fusion of Silver Nanowires. *Sci. Rep.* **2020**, *10*, 1–8.
- [131] Wang, D.; Hao, C.; Zheng, W.; Peng, Q.; Wang, T.; Liao, Z.; Yu, D.; Li, Y. Ultralong Single-Crystalline Ag₂S Nanowires: Promising Candidates for Photoswitches and Room-Temperature Oxygen Sensors. *Adv. Mater.* **2008**, *20*, 2628-2632.
- [132] Demis, E.C.; Aguilera, R.; Sillin, H.O.; Scharnhorst, K.; Sandouk, E.J.; Aono, M.; Stieg, A.Z.; Gimzewski, J.K. Atomic Switch Networks—Nanoarchitectonic Design of a Complex System for Natural Computing. *Nanotechnology* **2015**, *26*, 204003.
- [133] Gubicza, A.; Manrique, D.Z.; Pósa, L.; Lambert, C.J.; Mihály, G.; Csontos, M.; Halbritter, A. Asymmetry-Induced Resistive Switching in Ag-Ag₂S-Ag Memristors Enabling a Simplified Atomic-Scale Memory Design. *Sci. Rep.* **2016**, *6*, 30775.

- [134] Hadiyawarman; Usami, Y.; Kotooka, T.; Azhari, S.; Eguchi, M.; Tanaka, H. Performance of Ag-Ag₂S core-shell Nanoparticle-Based Random Network Reservoir Computing Device. *Jpn. J. Appl. Phys.* **2021**, *60*, SCCF02.
- [135] Sadovnikov, S.I.; Gusev, A.I. Recent Progress in Nanostructured Silver Sulfide: From Synthesis and Nonstoichiometry to Properties. *J. Mater. Chem. A.* **2017**, *5*, 17676.
- [136] Xiong, J.; Han, C.; Li, W.; Sun, Q.; Chen, J.; Chou, S.; Li, Z.; Dou, S. Ambient Synthesis of a Multifunctional 1D/2D Hierarchical Ag-Ag₂S Nanowire/Nanosheet Heterostructure with Diverse Applications. *Cryst. Eng. Comm.* **2016**, *18*, 930.
- [137] Liang, C.; Terabe, K.; Hasegawa, T.; Aono, M. Resistance Switching of an Individual Ag₂S/Ag Nanowire Heterostructure. *Nanotechnology* **2007**, *18*, 485202.
- [138] Lai, X.; Feng, X.; Hu, J.; Tan, L.; Liu, J.; Chen, Y.; Deng, X.; Li A. A Straightforward and Effective Strategy for Controllable Synthesis of Ag/Ag₂S and Ag/CdS Heterojunction Nanowires. *J. Nanopart. Res.* **2015**, *17*, 113.
- [139] Yang, J.; Ying, J.Y. Nanocomposites of Ag₂S and Noble Metals. *Angew. Chem. Int. Ed.* **2011**, *50*, 4637-4643.
- [140] Sadovnikov, S.I.; Gusev, A.I. Universal Approach to the Synthesis of Silver Sulfide in the Forms of Nanopowders, Quantum Dots, Core-Shell Nanoparticles, and Heteronanostructures. *Eur. J. Inorg. Chem.* **2016**, *2016*, 4944-4957.
- [141] Hosseini, M.; Frick, N.; Guilbaud, D.; Gao, M.; LaBean, T.H. Modeling and Measurement of Non-Linear Electrical Properties of Self-Assembled Ag₂S Nanowire Resistive Switching Networks for Neuromorphic Applications. *Submitted*.
- [142] Liao, Z.-M.; Hou, C.; Zhang, H.-Z.; Wang, D.-S.; Yu, D.-P. Evolution of Resistive Switching over Bias Duration of Single Ag₂S Nanowires. *Appl. Phys. Lett.* **2010**, *96*, 203109.

CHAPTER 4

Fabrication and Characterization of Nanowire-Polymer Composites

4.1 Introduction and background

4.1.1 Background

In recent years, there have been numerous studies on polymer-based composites that exhibit nonlinear conductive properties. In these studies, the composites are composed of dispersed phase materials that show nonlinear characteristics, such as zinc oxide nanowires (ZnO NWs)^[143], graphene nanoplatelets^[144], and carbon nanotubes (CNTs)^[145,146,147]. Usually, these fillers are embedded in the polymer matrix by solution blending to make composites with certain applications in electronic devices^[148]. However, the state-of-the-art nano/micromaterial-polymer composites being reported are composite thin films and thus are not truly three-dimensional (3D) composites. Even fewer studies had a focus on wire-shaped dispersed phase material. Therefore, there is a considerable need for the investigation of 3D nanowire-polymer composites that exhibit interesting nonlinear characteristics.

4.1.2 Fabrication of polymer-based composites

Polymer solubility and dissolution behavior plays a key role in composite integration. The dissolution process and condition of polymers determine their capability of being used as the continuous phase of the a composite^[149]. To make a composite with a polymeric matrix, a solution of dissolved polymer can be combined with a solution containing the dispersed phase materials^[140]. With proper mixing and once the solvent evaporates from the mixture, a solid phase composite can be formed. During this process, parameters such as temperature and external agitation can greatly influence the dissolution of the polymer and the integration of the dispersed phase. It is

believed that agitation prevents the formation of a gel layer during polymer dissolution as the solvent penetrates the polymer^[141-150]. Therefore, it is desirable to apply stirring during the process. In our project, we paid special attention to the polymer dissolution process during composite fabrication to ensure high quality and good reproducibility of the overall dispersion and integration.

4.1.3 Project overview

In this project, we explored composite fabrication and characterization using different types of polymers as the continuous phase to integrate nanowires, such as silver nanowires (AgNWs) and silver sulfide nanowires (Ag₂S NW), into a polymeric matrix. Specifically, we tested thermoplastic polymers such as polycaprolactone, thermosetting polymers such as epoxy resin, polydimethylsiloxane (PDMS), and acrylic plastic casting, elastomers such as Ecoflex™ silicone rubber compound, as well as biopolymers such as agarose and nanocellulose. One objective of this project is to identify the desirable solvents to suspend AgNWs that allow homogeneous embedding of nanowires into a polymeric matrix. The second objective is to determine a reliable process to integrate the dispersed phase material in the continuous phase material. We performed characterization of the surface and internal microstructures of the final composites, as well as the dispersed phase materials before being embedded. In addition, we have conducted electrical measurements to characterize the electrical response of the AgNW-based composites.

The fabrication and characterization of nanowire-polymer composites provided an initial approach for us to quickly and inexpensively identify important information required for our further studies—using molecular self-assembly techniques to organize neuromorphic architectures, nanocircuits, and nanoelectronics. The composites fabricated during this project,

especially the polycaprolactone-based composites, served important roles in optimizing the setup for electrical measurements and determining the desirable concentrations of the dispersed phase materials to provide percolated networks within the final composites. Moving forward, by exploring biocompatible materials such as agarose and nanocellulose, we were able to prepare nanomaterial networks assembled in a hydrogel and were able to study composites of different states, which gave us insight into nanomaterials assembled in DNA-based hydrogels. As a summary of the various composites surveyed, Table 4.1 lists the combinations of dispersed phase materials and continuous phase materials that have been explored and tested in this. Besides AgNWs and Ag₂S NWs, we also studied dendritic silver structures (Ag dendrite), ZnO NWs, and CNTs as the dispersed phase.

Table 4.1 Composite combinations—dispersed phase explorations in different continuous phases.

	AgNW	Ag ₂ S NW	Ag dendrite	ZnO NW	CNT
<i>Thermoplastic polymers:</i>					
Polycaprolactone	X	X		X	
<i>Thermosetting polymers:</i>					
Epoxy resin		X			X
Instant epoxy					X
Acrylic plastic casting	X	X	X		X
PDMS	X	X			
<i>Elastomer:</i>					
Ecoflex TM (00-30)	X				
<i>Biopolymers:</i>					
Agarose	X	X	X		X
Nanocellulose	X	X			

4.2 Three-dimensional nanowire-polymer composites

4.2.1 Nanowire dispersion

We prepared or acquired five types of dispersed phase materials for this project. ZnO NWs (D: 50-120 nm, L: 5-50 μm) were purchased from ACS Materials. CNTs (multi-walled carbon nanotube, >98% carbon basis, D: 6-13 nm, L: 2.5-20 μm) were purchased from Sigma-Aldrich. AgNWs were synthesized with a polyol-mediated method modified from the protocol reported by Andres *et al.*^[151] and described in Chapter 2. Synthesized AgNW were dispersed in ethanol (pure, 200 proof, Sigma-Aldrich) for storage to prevent oxidation. To fabricate Ag₂S NWs, the amounts of AgNWs and sulfur particles required in the reaction were calculated stoichiometrically. Next, a sulfur solution was made by dispersing measured sulfur particles in ethanol via bath sonication, and the solution was added to the AgNW dispersion in ethanol to allow sulfurization of nanowires. The mixture was set on a hot plate at around 60°C for about 10 minutes to allow the conversion to complete, which was indicated by the color of the solution switching to dark brown. Resulting Ag₂S NWs were left suspended in ethanol until further usage. The dendritic silver structures were fabricated based on an adapted method reported by Yang *et al.*^[152]. This approach grows Ag dendrites by using copper to reduce Ag⁺ in silver nitrate solution. In short, 50 mM silver nitrate (AgNO₃; >99%, Sigma-Aldrich) solution was first prepared in DI water. It was then drop cast on the edge of a copper film to grow Ag dendrites. After 1 min, the surface was rinsed carefully with DI water to stop the reaction.

The first study for the integration of nanowire-polymer composites was to determine the dispersion conditions of AgNWs in different types of solutions. We wanted to determine the best solution conditions in which to disperse AgNWs, which would also allow polymer dissolution for specific types of polymer as the continuous phase of the composites. During this study, we found

that AgNWs could be well dispersed in isopropanol, chloroform, and ethanol. However, we found that hexane and toluene did not support good dispersion, as AgNWs would agglomerate and settle to the bottom of the container when dispersed in these two solvents. For this reason, hexane and toluene were not considered for further integration of AgNWs into a polymeric matrix, although they can effectively lower the viscosity of certain polymers (i.e. PDMS), which assists polymer dissolution. In the meanwhile, chloroform can also effectively dissolve polymers like polycaprolactone, thus we mainly used chloroform (With 0.75% ethanol as preservative, Fisher Scientific) for such purposes. In addition, ethanol was used to disperse Ag₂S NWs and ZnO NWs, and a short period of bath sonication (<1 min) was applied to assist dispersion. CNTs were dispersed in DI water via bath sonication with sodium dodecylbenzenesulfonate (SDBS, technical grade, Sigma-Aldrich) detergent at the concentration of 40 mg/L. We also found that it is possible to perform solvent exchange for AgNW, Ag₂S NW, or ZnO NW solutions to substitute ethanol for chloroform. Therefore, we performed solvent exchange of dispersed phase into chloroform when a polymer was dissolved in chloroform before composite integration.

4.2.2 Composite integration

PDMS is frequently used to integrate AgNWs into films for applications in stretchable, transparent, and conductive 2D films^[153,154,155]. With this inspiration, we explored the possibilities of embedding AgNWs and Ag₂S NWs into PDMS to assemble 3D composites. To make such composites, PDMS (SYLGARD 184, Dow Corning) was first prepared by mixing the base and hardener components in a 10 : 1 ratio. Then, the mixture was degassed quickly in a vacuum chamber while it was in the liquid state. In the meantime, the desired volume of AgNW solution was prepared. The AgNW solution was then added to the PDMS reaction mixture and the sample was placed on a hot plate at 70°C with constant magnetic stirring. As the reaction proceeds and

solvent evaporates, the mixture becomes more and more viscous. The viscous mixture was transferred and casted in the mold with the ideal shape and dimensions for the final composite. We noticed that among the solvents we explored chloroform evaporates most slowly from PDMS. Because of that, more AgNWs settled at the bottom of the mixture during the evaporation process, and the final composite was observably inhomogeneous. Therefore, we suggest the usage of isopropanol or ethanol in preparing AgNW solution for further integrations with PDMS. Similarly, the composites made with acrylic plastic casting (Electron Microscopy Sciences), epoxy resin (Embed-812 resin, DDSA (Dodecenyl Succinic Anhydride Specially Distilled), NMA (Methyl-5-Norbornene-2,3-Dicarboxylic Anhydride), DMP-30, Electron Microscopy Sciences), or instant epoxy (Devcon) were processed by mixing multiple parts of the commercial products in the suggested ratios.

Another type of continuous phase we explored was Ecoflex™ silicone rubbers (00-30, Smooth-On). Ecoflex rubbers are platinum-catalyzed silicones, a type of pre-strained stretchable elastomer. It is cured from a 1:1 ratio mixture of two components under room temperature. It is commonly used to make soft, translucent, and stretchable molds and films^[156-157]. Therefore, we were inspired to explore its performance in making stretchable and conductive 3D gels with AgNWs. These composites will allow us to measure the electrical properties of the composites in different configurations—the embedded AgNW networks can be easily modified by stretching the composite, which allows us to quickly collect information on the electrical characteristics of the composites. Another advantage of using Ecoflex is that it can be cured without external heating, and the slow curing process (i.e. four hours) after mixing two parts will provide sufficient time for us to perform the integration processes.

Since our eventual goal is to use biomolecules to assemble nanomaterials into a 3D networks, it is beneficial to also test biocompatible polymers. Therefore, we studied agarose- and nanocellulose-based hydrogel composites. Agarose is a polysaccharide extracted from red seaweed. Its sol-to-gel transition property allows for easy formation of hydrogel upon cooling^[158]. When making agarose-based hydrogels, the powder form of low melting point agarose (UltraPure™ agarose, ThermoFisher Scientific) was first mixed with DI water that gives a final agarose concentration of 3.5-4 wt% in the composite. Then, the mixture was heated on a hot plate to bring the solution to boiling while stirring. The solution was heated until all the agarose powder was completely dissolved. After that, the AgNW suspension was added and mixed into the agarose solution, which was then transferred to a casting tray. The cast was then placed in a refrigerator to lower the temperature and to allow the hydrogel formation. The sample was stored at 4°C until further testing and characterization.

Of all the combinations of dispersed phase materials and continuous phase materials we explored (Table 4.1), we found that the best combination to support further electrical characterization was AgNW-Ag₂S NW-polycaprolactone composite. Among these thermoplastic and thermosetting polymers listed in Table 4.1, polycaprolactone-based composites showed the best homogeneity during mixing, which is a key factor for reproducibility and to gain controls over the final embedded networks. Processing polycaprolactone also allows us to control its viscosity when it is dissolved, which is another advantage that the other types of thermoplastic and thermosetting polymers do not have. Therefore, all the following electrical characterization reported in Section 4.5 are measured from polycaprolactone-based composites, and a more detailed protocol to fabricate polycaprolactone-based composites is given in Section 4.3. Although Ecoflex is also able to support homogeneous integration of nanomaterials, the electrical responses of

Ecoflex-based composites were more difficult qualified due to its stretchable nature and porous appearance. With the goal of using the 3D composite samples as testing materials to optimize our electrical measurement setups, polycaprolactone remains the most desirable polymer from Table 4.1 for this project.

4.3 Method for composite fabrication

The relationship between nanowire volume fraction and weight fraction to the entire composite can be calculated based on the densities of the dispersed phase material and the continuous phase material. As a modification from a publication by Park *et al.*^[159], the following equation was used,

$$\Phi_{NW} = \frac{\frac{W_{f \cdot NW}}{\rho_{NW}}}{\frac{W_{f \cdot NW}}{\rho_{NW}} + \frac{W_{f \cdot PCL}}{\rho_{PCL}}}$$

where Φ_{NW} , $W_{f \cdot NW}$, and ρ_{NW} are nanowire volume fraction, weight fraction, and density, respectively. $W_{f \cdot PCL}$ and ρ_{PCL} are weight fraction and density of the polycaprolactone matrix. To fabricate a composite with a specific volume fraction of nanowires, the mass of AgNWs (or another type of nanowire filling, such as Ag₂S NWs) and polycaprolactone were calculated accordingly. Then, based on the concentration of AgNWs in ethanol, the required volume of AgNW solution was calculated.

Polycaprolactone (average MW ~14,000, Sigma-Aldrich; InstaMorph Moldable Plastic, InstaMorph) was purchased as solid pellets that melt and reshape above 66°C. The fabrication method for polycaprolactone-based composite was modified based on the protocol developed by Nikolay Frick^[160]. To embed nanowires in the polycaprolactone matrix, the calculated amounts of

AgNWs and Ag₂S NWs that both dispersed in ethanol were combined and mixed first. Then, a small volume of chloroform (~2 mL chloroform for 40 mg polycaprolactone) was added to the polycaprolactone pellets, and stirring was applied to assist the dissolution of polycaprolactone. Once the polycaprolactone pellets became transparent and were all dissolved in chloroform, the ethanol suspension with AgNWs and Ag₂S NWs was added to the mixture while stirring (Figure 4.1 (a)). The mixture becomes more and more viscous as chloroform and ethanol evaporate. Then, the viscous mixture was transferred to a desired casting mold (that could be connected to an electrode array, as shown in Figure 4.1 (b); or in a centrifuge tube, with the resulted sample shown in Figure 4.1 (c)), which was then placed under vacuum for final degassing. When suitable, an electrode array should also be inserted into the viscous mixture at this time (Figure 4.1 (c)). The electrode array shown in Figure 4.1 (c) was conceptualized by Nikolay Frick then fabricated by Mahshid Hosseini. Once all the solvents evaporate, a solid composite will be left with embedded nanowires.

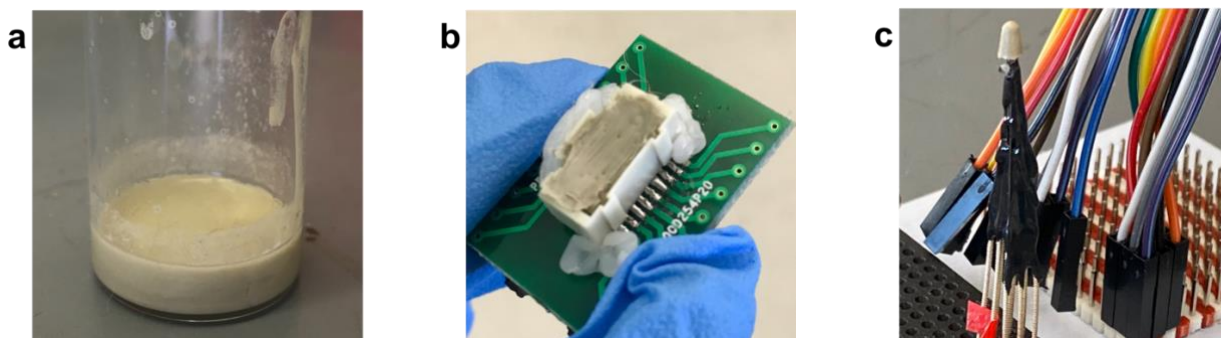


Figure 4.1 (a) The mixture of dissolved polycaprolactone in chloroform and AgNW solution. Photo was taken before the solvents evaporated. (b) Final AgNW-polycaprolactone composite connected to an electrode array. 4 vol% AgNWs were embedded in the polycaprolactone matrix. (c) A AgNW-Ag₂S NW-polycaprolactone composite attached to an electrode array. 0.4 vol% AgNWs and 4 vol% Ag₂S NWs were embedded in the polycaprolactone matrix.

4.4 Characterization

We designed three approaches in characterizing the composite material comprising of silver-based nanowires in a polymeric matrix. The first approach was to characterize the dispersed phase materials deposited onto a 2D substrate. This approach allowed us to reveal the natural morphology of the silver-based materials before they are integrated into a continuous phase. Here, we present the 2D characterization of three types of materials: AgNWs, Ag₂S NWs with silver cores and sulfur-modified surfaces, and dendritic silver structures. The microscopic characterization of AgNWs can be found in Chapter 2. SEM images of Ag₂S NWs can be found in Chapter 3. Microscopic characterization of silver dendrite is shown in Figure 4.2. Here we observed that Ag₂S NWs are much shorter than AgNWs after the sulfurization process. Ag₂S NWs also have a greater averaged diameter than AgNWs because of the sulfur particles and islands on the nanowire surfaces. We also imaged a nanowire networks that combined AgNWs and Ag₂S

NWs, as shown in Figure 4.2 (c). We often used this combination in polycaprolactone-based 3D composites. Figure 4.2 (c) shows both long AgNWs and short Ag₂S NWs that are randomly oriented and connected.

In addition, we examined silver dendrite samples that show dendritic structures that are more neuromorphic than nanowires. The optical microscope image Figure 4.2 (a) at a low magnification shows the amorphous and self-assembled silver nanocrystals in the branching tree and trunk structures. When comparing this optical image with SEM images (Figure 4.2 (b)), we determined that the growth of silver dendrites naturally form a heterostructure network comprising of nanocrystals and connections in different dimensions. This feature provides interesting conductivity pathways, and thus silver dendrites are seen as a great candidate material with which to build neuromorphic networks.

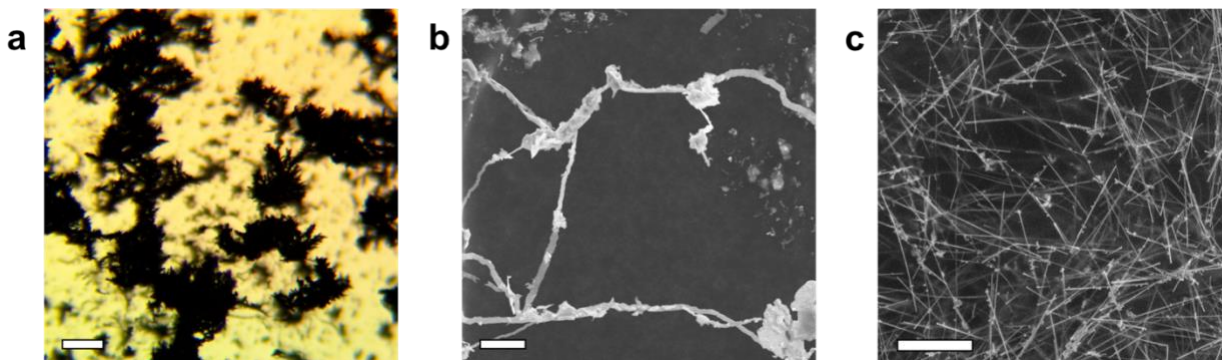


Figure 4.2 (a) Optical microscopy and (b) SEM images of silver dendrites. Scale bars are 400 μm and 10 μm , respectively. (c) SEM image of the combination of AgNWs and Ag₂S NWs. Scale bar is 10 μm .

In the second approach, we moved forward to characterize the 3D composites comprising of the dispersed phase materials in different types of continuous phase materials. In this approach,

however, the composites might have been undesirably altered when preparing samples for characterization. In this case, either the outer surfaces of the 3D samples were characterized directly, or the samples were cut with different techniques to expose the internal network structure. However, in either case, the characterization would only provide a general idea on the embedded networks but would fail to bring the unaltered morphology of nanostructures embedded in the 3D composites. The value of this approach is to allow us to compare the network morphology at the surfaces of 3D composites with their internal network structures, and to study how the shear and compression forces from cutting may have modified the internal structures of a polymeric composites. Figure 4.3 (a-b) presents the SEM images of the surfaces of AgNW-based composites. Figure 4.3 (a) was taken from a composite comprising of AgNWs and polycaprolactone, similar to the one shown in Figure 4.1 (b). This SEM image shows that AgNWs are evenly integrated into the polycaprolactone matrix and are accordant with the shape of the final composite. Figure 4.3 (b) shows a dehydrated sample that used nanocellulose to integrate AgNWs. We found that some nanowires were broken or twisted during the dehydration process, and these nanowires no longer appear straight or in their natural curviness. For this reason, we chose to use polycaprolactone as the polymeric matrix for further studies, as polycaprolactone supports further electrical measurements without disturbing the appearance and connections of AgNWs.

Moving on, we also studied the integration of multiple types of dispersed phase materials into the polycaprolactone matrix. Specifically, we explored assembling 1-5 vol% of Ag₂S NWs with 0.25-2 vol% AgNWs in the composite. Figure 4.3 (c-d) are SEM images of a AgNW-Ag₂S NW-polycaprolactone composite comprising of 0.5 vol% AgNWs and 5 vol% Ag₂S NWs. By comparing these two images with Figure 4.2 (c), we could clearly see the differences in nanowire morphology before and after they are assembled into a 3D composite. The SEM images of 3D

samples clearly show the clumpiness of short Ag₂S NW networks. The images also reveal that long AgNWs help to connect these regional and smaller networks built by Ag₂S NWs. The combination of AgNWs and Ag₂S NWs allowed us to introduce and to study clumpiness of the network. The surfaces shown in figure 4.3 (c-d) were exposed by manually cutting the composite to reveal its internal structures. However, some nanowires might have been shifted due to shear and compression forces during the cutting process.

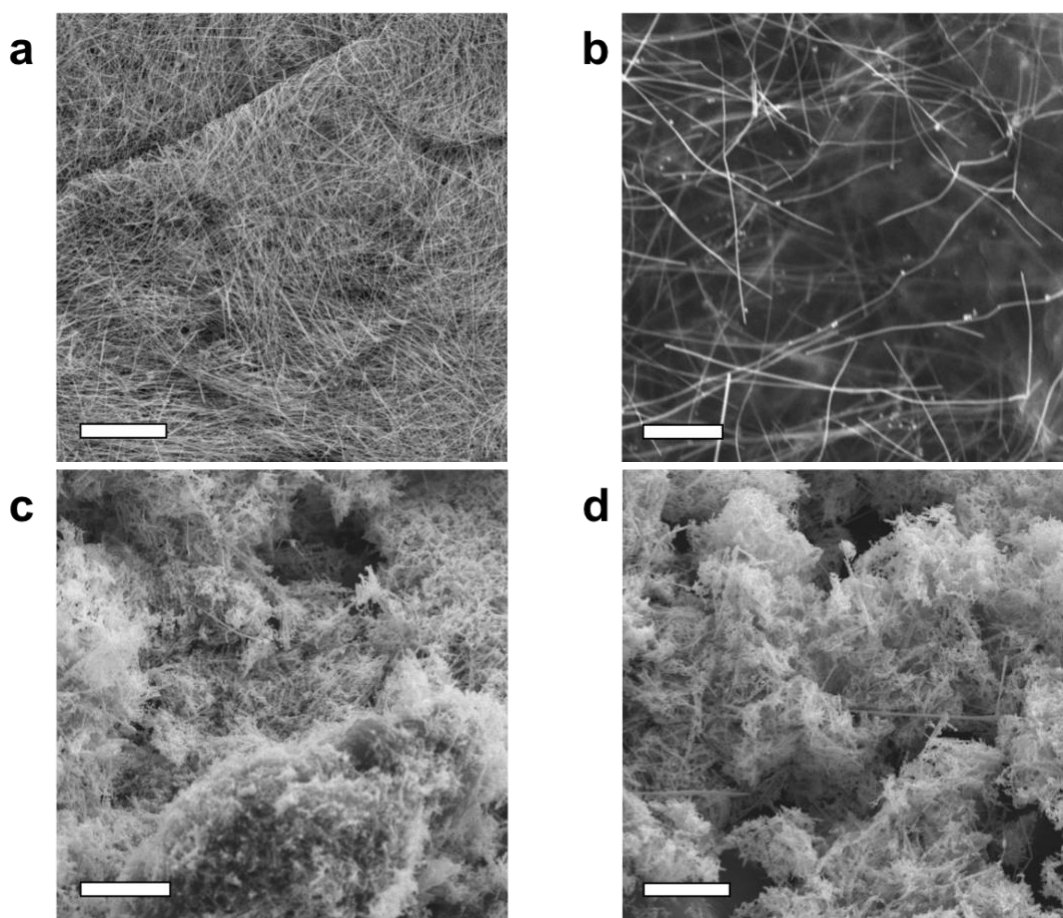


Figure 4.3 SEM images of the surfaces of (a) AgNW-polycaprolactone composite and (b) AgNW-nanocellulose composite. Scale bars are 20 μm and 5 μm , respectively. (c-d) SEM images of the cutting of AgNW-Ag₂S NW-polycaprolactone composite, showing long AgNWs and short Ag₂S NW network. Scale bars are 10 μm .

Finally, the goal of the third approach was to reveal and identify the unmodified morphology of internal nanowire structures embedded in the polymeric matrix. In this approach, we would like to explore different characterization methods to expose the embedded 3D nanostructures without interfering or altering their appearance. This approach was closest to demonstrating the actual connection, direction, and concentration of embedded silver-based materials, which provided valuable information to assist us to understand the electrical behavior of the composites. In the following, we will present three characterization techniques that can reveal the embedded nanowires in the composites without modifying their microstructures—cryogenic electron microscopy (cryo-EM), micro-computed tomography (micro-CT), and nano-computed tomography (nano-CT).

We first used a 3D X-ray tomography technique, micro-CT (Bruker SkyScan1174), to quickly examine the homogeneity of the polycaprolactone-based composites. Micro-CT is a non-destructive imaging technique that produces a 3D reconstruction of an object to reveal its internal structure^[161]. One issue that may arise from using a polymeric matrix to assemble dispersed phase materials is that the dispersed phase may not be homogeneously embedded, and a gradient of concentration could form. Therefore, micro-CT is a quick and convenient tool to check the consistency and uniformity of nanowire distribution within the composites before further studies. Figure 4.4 (a) shows a reconstructed structure based on 364 scans of a composite sample comprising of 0.5 vol% AgNWs and 2% Ag₂S NWs in the polycaprolactone matrix. The dimensions of the sample are 1 cm by 1 cm by 3 mm. And the micro-CT scans have a 3D spatial resolution of 6.4 μm . Although the resolution of micro-CT scans is not high enough to reveal individual nanowires, the scans and the reconstruction proved that the composite is overall homogeneous and there is no concern about the formation of a concentration gradient.

Then, we used nano-CT (Zeiss Xradia 510 Versa) to disclose the internal nanowire structures over one area of the sample. Nano-CT is a high-resolution 3D tomography system that allows non-destructive submicron imaging^[162,163,164]. Figure 4.4 (b) shows a nano-CT scan of a specimen comprising of 0.5 vol% AgNWs and 2% Ag₂S NWs in the polycaprolactone matrix. The resolution of these nano-CT scans is 60 nm voxel size, and the scanning window is 118 μm by 118 μm. With this much higher resolution, the nano-CT scans are able to show some individual nanowires that have a different contrast than the polymeric matrix (background in the figure). These scans show us that the nanowires are truly randomly oriented in the 3D composite and that there are no obvious connected pathways formed by AgNWs throughout the entire composite in this sample, although there are regional connections made by less than five nanowires. When combining this information with the results of further electrical measurements, we were able to determine the desired concentrations of embedded nanowires that allow the final composites to reach percolation. The electrical characterization reported in Section 4.5 were measured from AgNW-Ag₂S NW-polycaprolactone composite with a higher nanowire concentration than the specimen demonstrated in Figure 4.4 (b).

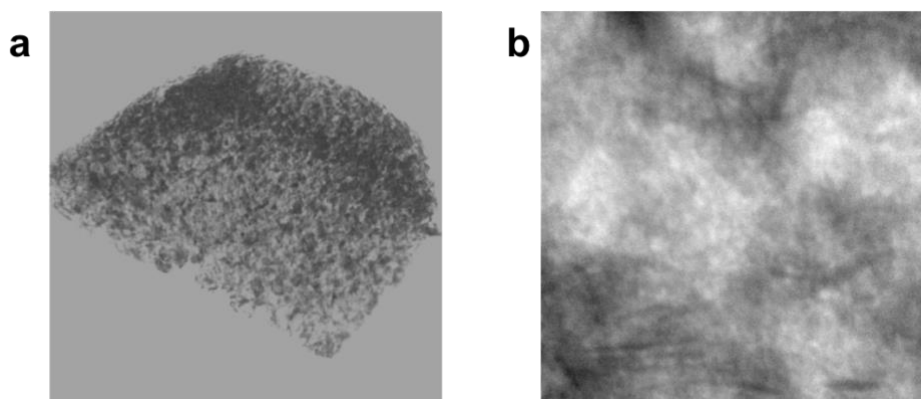


Figure 4.4 (a) Reconstructed 3D composite structure from micro-CT scans and (b) a nano-CT scan (118 μm by 118 μm) of a AgNW-Ag₂S NW-polycaprolactone composite.

Another technique to reveal the internal structures of soft materials is cryo-EM. We used JEOL JSM-7600F SEM equipped with a cryogenic stage and transfer system and Gatan Alto-2500 and Horiba CL detector. Cryo-EM is a desirable imaging technique for hydrated specimens, such as our hydrogel composite samples^[165]. To prepare for a cryogenic specimen, the hydrogel composite was first loaded onto the edge mounting sample holder, which was then plunge frozen in the liquid nitrogen slush. Next, the sample was loaded to the cryogenic chamber under vacuum, where it was cryo-fractured with a cold knife fracture device to expose a cross-section surface. Then, the temperature of the chamber was risen to 95°C to sublimate ice and to etch the sample for five minutes in order to reveal its internal structures. Once the sample was cooled down again, an in-situ sputter coater coated the etched surface with 5 nm of Au/Pd. Then, the sample was transported to the imaging chamber for SEM imaging under cryo-temperature. Figure 4.5 shows SEM images of an agarose-based hydrogel sample comprising of 3.5 wt% agarose and 1.5 vol% AgNWs. Figure 4.5 (a) in particular shows the AgNW cutoffs from cryo-fracture in the cryogenic chamber, in which the two nanowires were likely to be connected before the fracture. These images gave us an insight into the internal microstructure of nanowire networks and showed us that AgNWs are randomly oriented and embedded in the agarose networks. The cryo-EM images agreed with the X-ray tomography scans and they both proved our hypothesis for the morphology of AgNW networks in the 3D composites.

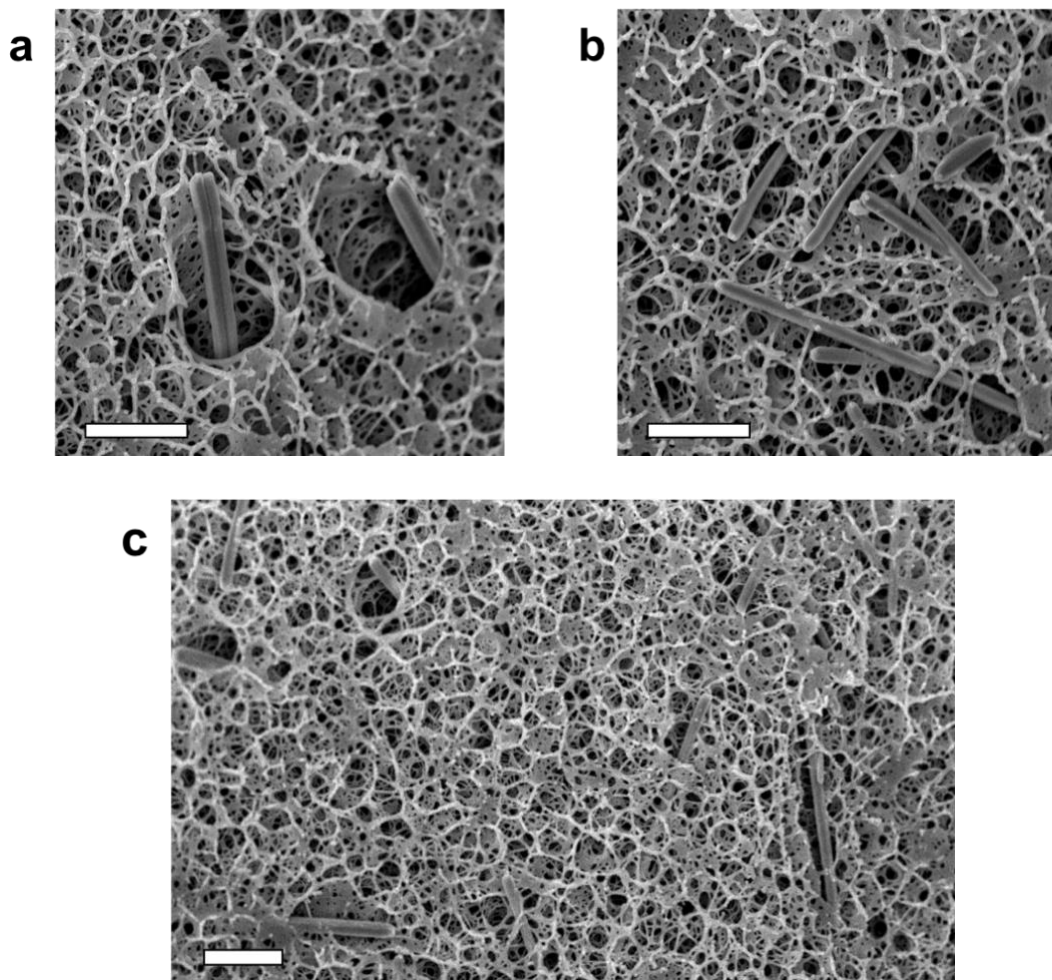


Figure 4.5 SEM images of a cryo-fractured hydrogel composite, showing AgNWs embedded in the agarose networks. Scale bars are 1 μm .

4.5 Electrical measurement

We performed two-terminal current-voltage (IV) characterization for the nanowire-polymer composites to investigate their electrical responses. As shown in Figure 4.1 (c), a 3 by 3 electrode array with 100 μm spacings was fabricated using stainless steel needles. The electrode array was conceptualized by Nikolay Frick and fabricated by Mahshid Hosseini. The electrode array was connected to the polycaprolactone-based specimen, and the distal end of the electrode array was inserted in a ZIF socket that was connected to a 2 channel (medium power)

source/monitor unit module (Agilent Technologies E5272A). The sample along with the electrode array setup was placed in a Faraday cage (Hewlett Packard Test Fixture Analyzer 16058A) while IV curve measurements were recorded. We chose to use IV characterization since it allows us to measure small conductivity responses when a positive or negative voltage pulse is applied.

Specifically, we applied 10 consecutive pulses at positive and negative 3 V to a composite comprising of 0.4 vol% AgNWs and 4 vol% Ag₂S NWs in the polycaprolactone matrix, and the current outputs were recorded in Figure 4.6 (a). Its corresponding triangle pulse scanning curves are present in Figure 4.6 (b). The IV curves of AgNW-Ag₂S NW-polycaprolactone composite exhibited nonlinearity in all pulses due to the nonlinear properties of Ag₂S NWs. We also saw that each pulse resulted in a different current response, which most likely demonstrated that a different conductivity pathway was taken between two electrodes inside the composite sample. In contrast, such huge differences in current responses were not obvious from the 2D AgNW /Ag₂S NW network samples, as reported in Chapter 3. When performing the IV curve characterization in the same setup over a composite comprising of 0.5 vol% AgNWs and 5 vol% Ag₂S NWs in the polycaprolactone matrix (Figure 4.7), we observed similar nonlinear responses, with a slightly higher current output in magnitude as expected. In the AgNW-Ag₂S NW-polycaprolactone composites, Ag₂S NW served as the media for filament formation in which silver ion migration occurred. The network initially exhibited a high-resistant state. When the system was applied with a voltage pulse at 3 V, silver ion migration started to occur, forming a conductive filament through the Ag₂S NW. The network transited from the high-resistance state to a low-resistance state. Then, the unstable filament ruptured as voltage decreased back to 0 V. In the following voltage pulses, a different current pathway was activated through the network, showing an increased current response with the same applied voltage. This interesting switching behavior proved that the

AgNW-Ag₂S NW-polycaprolactone composite can be a great candidate for neuromorphic computing applications. Additional IV curve measurements can be found in Nikolay Frick's doctoral dissertation^[166].

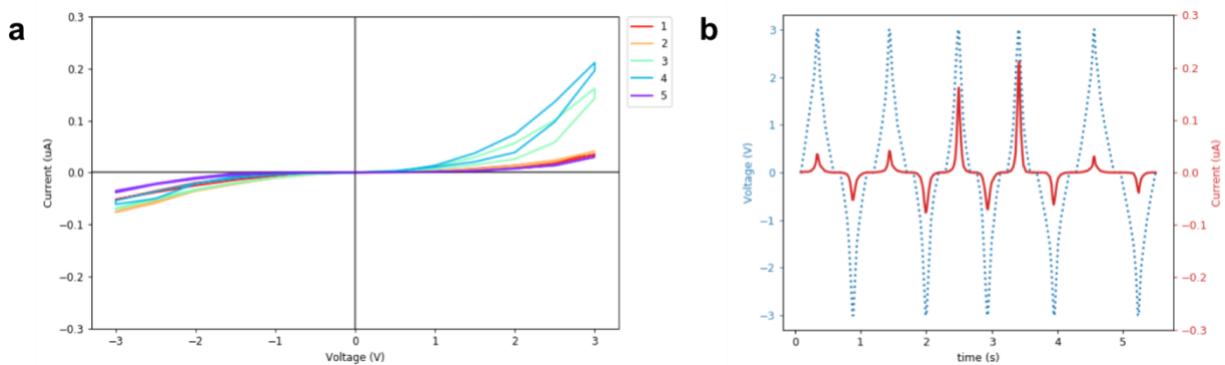


Figure 4.6 (a) IV curve measurements of a AgNW-Ag₂S NW-polycaprolactone sample comprising of 0.4 vol% AgNWs and 4 vol% Ag₂S NWs, measured with an electrode array shown in Figure 4.1 (c). Legend shows pulse number. (b) The corresponding triangle pulses scanning curves.

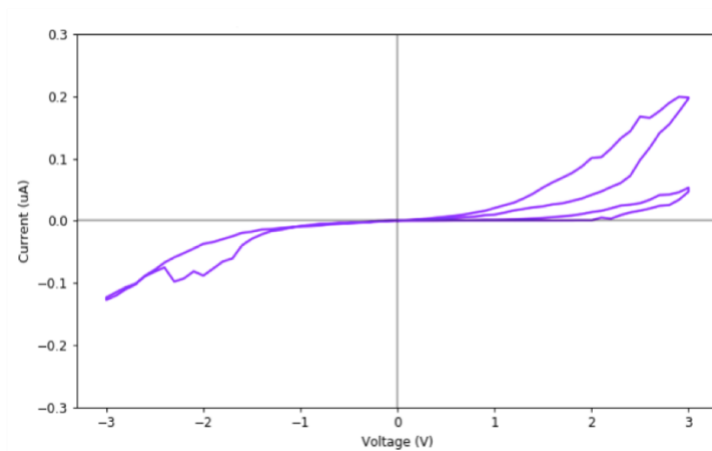


Figure 4.7 IV curve measurements of a AgNW-Ag₂S NW-polycaprolactone sample comprising of 0.5 vol% AgNWs and 5 vol% Ag₂S NWs.

4.6 Conclusions and future directions

As a summary, we explored the fabrication, characterization, and electrical measurements of multiple types of nanowire-polymer composites. The fabrication of nanowire-polymer composites is a quick and inexpensive approach to collect essential information for the further studies of this project. We explored dispersing and integrating different dispersed phase materials that include AgNWs, Ag₂S NWs, dendritic silver structures, ZnO NWs, and CNTs. We identified desirable solvents for the dispersion of each of the above materials for the purpose of assembling them into a polymeric matrix. We also explored using thermoplastic polymers, thermosetting polymers, elastomers, and biopolymers as the continuous phase of the composite. In particular, we explored polycaprolactone, PDMS, epoxy resin, instant epoxy, acrylic plastic casting, Ecoflex™, agarose, and nanocellulose. We determined that among these polymers polycaprolactone provides the best performance in homogeneous assembly of AgNWs and Ag₂S NWs, and is a robust continuous phase for further electrical studies. In addition, we reported a protocol to determine the volume fraction and each material and the integration method to make polycaprolactone-based composites.

We used three approaches to characterize the materials. We first applied optical, SEM, and TEM imaging for the 2D dispersed phase materials before embedding them. Then, we used the SEM imaging technique to demonstrate the surfaces and exposed internal microstructures of the composites. Finally, we applied micro-CT, nano-CT, and cryo-EM to reveal the unaltered internal nanowire morphology and structure. We proved that the embedded nanowire networks are truly randomly oriented and are homogeneously embedded in the continuous phase. The nano-CT scans also helped us to link the concentration of embedded nanowires with the electrical behavior of the final composite. Furthermore, the characterization of agarose-based hydrogel composites provided

a similar perspective for the internal structures of DNA-based hydrogels, which helped us to conceive the next step of this project that uses molecular self-assembly to integrate different nanomaterials.

We also performed IV curve measurements for the AgNW-Ag₂S NW-polycaprolactone composites of different concentrations. The IV curves exhibited nonlinear behaviors, where pulses gave different current outputs. This result showed how 3D nanowire networks differentiate from the behaviors of 2D networks. As a future step for this project, one can investigate the electrical responses of the composites using multi-channel measurement, i.e. a setup with multiple inputs and outputs that is more suitable for 3D specimen characterization. One can continue to explore the neuromorphic computing capabilities of the reported composites and to seek their applications in hardware with artificial intelligence applications. Another future direction is to continue to explore different characterization techniques to reveal the unaltered internal networks of the composites. One can use a serial block face scanning electron microscope (SBFSEM) to expose and image the microstructure in-situ layer by layer and to reconstruct the 3D internal structures. Another technique is to use atom probe tomography (APT) to perform chemical composition analysis and 3D imaging on the nanowire-polymer composites.

Bibliography

- [143] Yang, Y.; Qu, Z.; Wang, Q.; Sun, X. Nonlinear Conductive Characteristics of ZnO-Coated Graphene Nanoplatelets-Carbon Nanotubes/Epoxy Resin Composites. *Polymers* **2020**, *12*, 1634.
- [144] Chen, M.; Tao, T.; Zhang, L.; Gao, W.; Li, C. Highly Conductive and Stretchable Polymer Composites Based on Graphene/MWCNT Network. *Chem. Commun.* **2013**, *49*, 1612.
- [145] Chen, Q.Y.; Gao, J.; Dai, K.; Pang, H.; Xu, J.Z.; Tang, J.H.; Li, Z.M. Nonlinear Current-Voltage Characteristics of Conductive Polyethylene Composites With Carbon Black Filled Pet Microfibrils. *Chin. J. Polym. Sci.* **2013**, *31*, 211–217.
- [146] Wang, J.; Yu, S.; Luo, S.; Chu, B.; Sun, R.; Wong, C.P. Investigation of Nonlinear I–V Behavior of CNTs Filled Polymer Composites. *Mater. Sci. Eng. B* **2016**, *206*, 55–60.
- [147] Kim, K.H. Vural, M. Islam, M.F. Single-Walled Carbon Nanotube Aerogel-Based Elastic Conductors. *Adv. Mater.* **2011**, *23*, 2865-2869.
- [148] Pal, K.; Mohan, M.M.; Foley, M.; Ahmed, W. Emerging Assembly of ZnO-Nanowires/ Graphene Dispersed Liquid Crystal for Switchable Device Modulation. *Organ. Electron.* **2018**, *56*, 291-304.
- [149] Miller-Chou, B.A.; Koenig, J.L. A Review of Polymer Dissolution. *Prog. Polym. Sci.* **2003**, *28*, 1223-1270.
- [150] Asmussen, F.; Ueberreiter, K. Velocity of Dissolution of Polymers. Part II. *Polym. Sci.* **1962**, *57*, 199-208.
- [151] Andres, L.; Menendez, M.; Gomez, D.; Martinez, A.; Bristow, N.; Kettle J.; Menendez, A.; Ruiz, B. Rapid Synthesis of Ultra-Long Silver Nanowires for Tailor-Made Transparent Conductive Electrodes: Proof of Concept in Organic Solar Cells. *Nanotechnology* **2015**, *26*, 265201.
- [152] Yang, J.; Jiang, Z. Facile Fabrication of Dendritic Silver Structures and Their Surface Enhanced Raman Spectroscopic Properties. *J. Chem. Sci.* **2015**, *127*, 173-176.
- [153] Liu, H.-S.; Pan, B.-C.; Liou, G.-S. Highly Transparent AgNW/PDMS Stretchable electrodes for Elastomeric Electrochromic Devices. *Nanoscale* **2017**, *9*, 2633-2639.
- [154] Cheng, T.; Zhang, Y.-Z.; Lai, W.-Y.; Chen, Y.; Zeng, W.-J.; Huang, W. High-Performance Stretchable Transparent Electrodes based on Silver Nanowires Synthesized via an Eco-Friendly Halogen-Free Method. *J. Mater. Chem. C.* **2014**, *2*, 10369-10376.
- [155] Yun, S.; Niu, X.; Yu, Z.; Hu, W.; Brochu, P.; Pei, Q. Compliant Silver Nanowire-Polymer Composite Electrodes for Bistable Large Strain Actuation. *Adv. Mater.* **2012**, *24*, 1321-1327.

- [156] Lee, P.; Lee, J.; Lee, H.; Yeo, J.; Hong, S.; Nam, K.H.; Lee, D.; Lee, S.S.; Ko, S.H. Highly Stretchable and Highly Conductive Metal Electrode by Very Long Metal Nanowire Percolation Networks. *Adv. Mater.* **2012**, *24*, 3326-3332.
- [157] Jung, J.; Cho, H.; Yuksel, R.; Kim, D.; Lee, H.; Kwon, J.; Lee, P.; Yeo, J.; Hong, S.; Unalan, H.E.; Han, S.; Ko, S.H. Stretchable/Flexible Silver Nanowire Electrodes for Energy Device Applications. *Nanoscale* **2019**, *11*, 20356-20378.
- [158] Lopez-Marcial, G.R.; Zeng, A.Y.; Osuna, C.; Dennis, J.; García, J.M.; O'Connell, G.D. Agarose-Based Hydrogels as Suitable Bioprinting Materials for Tissue Engineering. *ACS Biomater.* **2018**, *4*, 3610-3616.
- [159] Park, J.; Kim, T.; Kim, W. Conductive Cellulose Composites with Low Percolation Threshold for 3D Printed Electronics. *Sci. Rep.* **2017**, *7*, 3246.
- [160] Frick, N. (2011). Self-Assembled Resistive Switching Nanocomposites for Neuromorphic Computation [Doctoral dissertation, North Carolina State University, Raleigh].
- [161] Ata, D.; Rangel, A.; Nguyen, Q.; Morahan, G.; Leonard, A. Micro-CT Scan with Virtual Dissection of Left Ventricle is a Non-Destructive, Reproducible Alternative to Dissection and Weighing for Left Ventricular Size. *Sci. Rep.* **2020**, *10*, 13853.
- [162] Yan, H.; Voorhees, P.; Xin, H. Nanoscale X-Ray and Electron Tomography. *MRS Bull.* **2020**, *45*, 264-271.
- [163] Grande, J.C.; Zhou, Y. Micro/Nano-CT for Visualization of Internal Structures. *Micros. Today* 2013, *21*, 16-22.
- [164] Contreras Jaimes, A.T.; de Pablos-Martín, A.; Hurle, K.; de Souza e Silva, J.M.; Berthold, L.; Kittel, T.; Boccaccini, A.R.; Brauer, D.S. Deepening Our Understanding of Bioactive Glass Crystallization Using TEM and 3D Nano-CT. *J. Eur. Ceram. Soc.* **2021**, *41*, 4958-4969.
- [165] Friedrich, H.; Frederik, P.M.; de With, G.; Sommerdijk, N.A.J.M. Imaging of Self-Assembled Structures: Interpretation of TEM and Cryo-TEM Images. *Angew. Chem. Int. Ed.* **2010**, *49*, 7850-7858.
- [166] Frick, N. (2011). Self-Assembled Resistive Switching Nanocomposites for Neuromorphic Computation [Doctoral dissertation, North Carolina State University, Raleigh].

CHAPTER 5

DNA Hydrogel-Based Composites with Self-Assembled Percolating Networks

5.1 Introduction and background

5.1.1 Background

Self-assembly by molecular recognition is a fundamental property of soft matter that can be utilized as a building tool to construct nanoscale to macroscale materials via bottom-up approaches. Using programmed assembly of nucleic acid molecules, structural DNA nanotechnology has rapidly expanded to construct sophisticated biomaterials^[167,168,169,170,171]. Beyond self-assembly, DNA is also biocompatible and can be readily conjugated with other bio/nanomaterials including proteins and conductive polymers^[172,173,174,175]. Leveraging these capabilities, DNA-based hydrogels have drawn a lot of attention starting with basic research and moving to applications such as biomedicine, biosensing, and drug delivery^[176,177,178,179,180,181]. DNA-based hydrogels are comprised of three-dimensional networks immobilizing a liquid. The networks can be formed by one or a combination of crosslinked polymers, inorganic or organic nanomaterials, and molecular self-assemblies^[182].

5.1.2 DNA-based hydrogels

The most common strategies to form DNA-based hydrogels are through complementary strand hybridization, enzyme-catalyzed assembly, and molecular entanglement^[183]. Studies based extensively upon hybridization focused mainly on pure DNA hydrogels with three-dimensional (3D) hydrophilic networks crosslinked via complementary basepairing. These hydrogels typically employed multistrand DNA tiles to construct the multivalent, crosslinking structural members (crosslinkers) as well as the spacer units (spacers) designed to assemble and control spacing

between adhesive arms of the crosslinkers^[184-185]. DNA hydrogels contain available free volume between their polymeric chains in which other nanomaterials can be trapped, thus providing them the capacity to nonspecifically incorporate functional components. Recently, studies have described strategies for coating and crosslinking inorganic nanomaterials such as quantum dots, nanoparticles, and nanotubes with DNA to create a variety of water soluble heterostructural conjugates^[186,187,188]. Using these DNA/nanomaterial conjugates as integral building blocks of crosslinked molecular networks has led to interesting DNA hydrogel composites assembled with oligonucleotides and other nanomaterials.

5.1.3 Carbon nanotubes and gold nanoparticles

Integration of nanomaterial conjugates makes it possible to modify the hydrogel properties to engineer mechanically and electrically adjustable materials. The mechanical properties of hydrogel-based composites can be fine-tuned by adjusting the concentrations and branch architectures of initial DNA tiles and embedded nanomaterials. However, the electrical properties of hydrogel composites bearing embedded conductive nanomaterials have rarely been studied, and there is a need for a deeper understanding of DNA as a building material to assemble 3D nanocircuits with conductive nanomaterials. One such material is carbon nanotubes (CNT). CNT are known for their utility in reinforcing nanofiber networks due to their excellent mechanical strength and stiffness^[189]. They are chemically stable and have high aspect ratios that contribute to electrical percolation in nanocomposites, which makes CNT a promising material in nanoelectronics applications^[190]. However, bare CNT naturally have low solubility in aqueous solutions in the absence of surfactants or sidewall functionalization^[191]. One method to effectively solubilize CNT is via biomolecular dispersion where single-stranded DNA (ssDNA) wraps around individual nanotubes via the strong non-covalent hydrophobic interactions between CNT walls

and DNA nucleobases to form water-soluble, supramolecular complexes^[192,193,194,195]. Besides improving solubility and manageability, the DNA-CNT hybrids also combine the advantageous electrical and mechanical properties of CNT and the molecular recognition capabilities of DNA. Moreover, CNT have been a promising material for the development of nonvolatile memory with short switching times^[196]. Some CNT-based memory has been shown to operate using electromechanical interactions of nanotubes with each other under the influence of an applied voltage^[197]. For this reason, researchers have chosen CNT to build memristive structures; these are structures that display variable electrical resistance based upon their ability to remember recent current/voltage activity.

Another classic example of integrating biomolecules with nanomaterials is DNA-functionalized gold nanoparticles (AuNP). A numerous studies have researched the interaction and the bio/nano interface between ssDNA and AuNPs. These hybrids have been shown useful for many applications from biosensing and nanomedicine, to use as building blocks with which to fabricate more complicated nanostructures^[198,199,200]. The original approach to make DNA-AuNP conjugates is to bind thiolated DNA to AuNP with the formation of gold-thiolate bond^[201-202]. More recently, another strategy has been reported to adsorb nonthiolated DNA strands onto AuNP via polyadenine bases that interact strongly with the gold surface^[203]. Since this method covers AuNP surfaces quickly and effectively with unmodified ssDNA and provides an acceptable loading capacity, it was adapted in our study for synthesis of DNA-functionalized AuNP.

5.1.4 Project Overview

Here, we present the construction and analysis of a variety of DNA hydrogels, some with embedded percolating networks using DNA-wrapped CNTs and DNA-attached AuNPs as crosslinkers. We started at the molecular level by designing DNA sequences and moved up to

macroscale hydrogels realized by bottom-up fabrication. We applied the crosslinker plus spacer design, where oligonucleotides were designed to form molecular networks by sequence-directed hybridization with sticky ends on crosslinker units (i.e. DNA tiles or DNA/nanomaterial conjugates) and coupling components (i.e. spacers) to construct 3D networks (Figure 5.1). In this way, we used molecular recognition to connect and form a network with nanomaterials. We were able to improve the mechanical strength of the formed hydrogels using several strategies including adjusting the spacer length and mixing different types of crosslinkers. We also showed that the 3D structures of nanomaterials can be programmed efficiently via nucleic acid sequence, and that it is possible to direct the formation of percolating networks with DNA self-assembly. In addition, using inspiration from biological neural networks that display extraordinary signal dynamics and processing abilities, we aimed to mimic some aspects of the morphology of natural neural networks using DNA self-assembly to fabricate nanoelectronic devices with measurable function. Nonlinear electrical properties of nanocomposites that integrate DNA-modified CNT are reported. Our eventual goal is to harness molecular recognition to precisely control the configuration and connection of nanomaterials to self-assemble into controllable nanostructures, and thus to engineer, fabricate, and characterize DNA-based hydrogels for desired applications. Future DNA hydrogel composites may find impactful application as building blocks in artificial computer hardware, with architectures inspired by natural neural systems for memory and information processing applications.

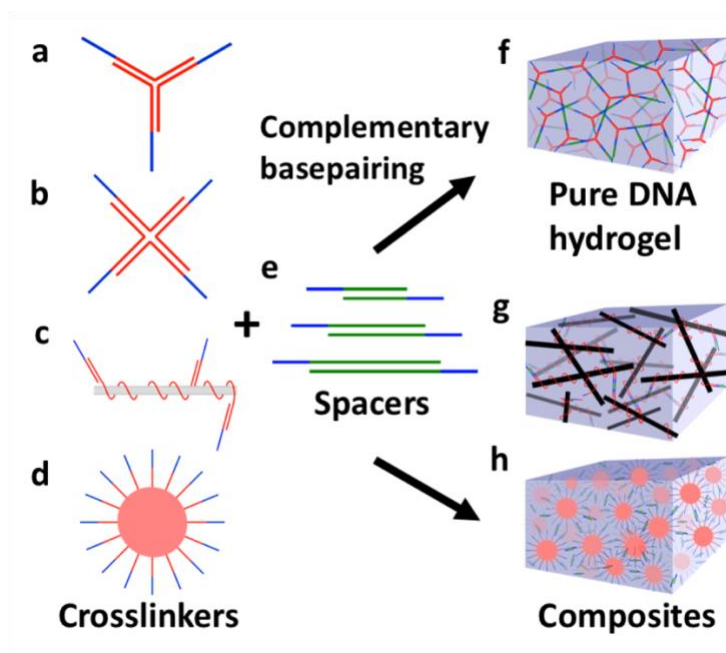


Figure 5.1 Schematic illustrations of DNA-based hydrogel formation. (a-d) Various types of crosslinkers: (a) Y-shaped DNA tile, (b) X-shaped DNA tile, (c) DNA-CNT conjugate, (d) DNA-AuNP conjugate; (e) Spacers of different lengths: Ss, Sm, and Sl; (f) Pure DNA hydrogel constructed by combining Y-shaped or X-shaped DNA tiles with spacers, (g-h) DNA hydrogel composites: (g) DNA-CNT hydrogel, and (h) DNA-AuNP hydrogel.

5.2 Design and construction of DNA hydrogels and DNA-based composites

5.2.1 Sequence design of DNA crosslinkers and spacers

We constructed DNA hydrogels by mixing crosslinker and spacer modules that associate based on DNA-DNA hybridization as shown in Figure 5.1. Four types of crosslinkers (Y-shaped DNA tiles, X-shaped DNA tiles, DNA-CNT conjugates, and DNA-AuNP conjugates) and three different lengths of spacers (Ss, Sm, and Sl; short (33 nt), medium (44 nt), and long (55 nt), respectively) were tested. With these building blocks, we produced two major types of hydrogels: pure DNA hydrogels and DNA/nanomaterial hydrogel composites. For DNA crosslinkers, we used

are listed in Table 5.1. Milli-Q deionized (DI) water (>18 M Ω .cm resistivity) was used for all experiments. In addition, Tris base (tris(hydroxymethyl)aminomethane, Fisher Scientific) and sodium chloride (NaCl, >99.5%, Sigma-Aldrich) were used to make buffer solutions. All pH values of the buffers were measured with a standard pH meter (Mettler Toledo SevenEasy™).

To construct Y-shaped DNA tiles, 10 μ L of 10 mM Y₁, Y₂, and Y₃ precursor strands for the building blocks were added to folding buffer solution (20 mM Tris-HCl (pH 7.5) and 100 mM NaCl) to obtain a final concentration of 1 mM for each strand. Then, the mixture went through a heat-annealing process where it was heated to 95°C for 5 min then cooled to room temperature over 30 min. Similarly, the X-shaped DNA tiles were assembled by mixing 8 μ L of 10 mM precursor strands X₁, X₂, X₃, and X₄ in the folding buffer solution to obtain a final concentration of 1 mM for each strand. The mixture went through the same heat-annealing process as described above.

Spacers are linear duplex formed by two ssDNAs that each contains a sticky end that is complementary to the sticky ends of crosslinkers. We used three different lengths of spacers 33 nt (Ss), 44 nt (Sm), and 55 nt (Sl). The spacer sequences were inspired by Xing, *et al.*^[194] and adapted to the other components of our system. All the spacer strands have the same sticky ends that are complementary to the sticky ends on crosslinkers. To construct spacers, 15 μ L of the two 10 mM precursor strands for the spacer was mixed in folding buffer (to obtain a final concentration of 1.5 mM for each strand. The mixture then went through the same heat-annealing process described above for DNA tiles. Spacers were also made to different concentrations to pair with different types of crosslinkers.

All the DNA sequences were examined using NUPACK online software to predict their most stable folded structures to avoid unwanted secondary structures (Figure 5.2). NUPACK is a

software suite for the design and analysis of nucleic acid structures^[206]. The final sequences offer a minimum free energy secondary structure.

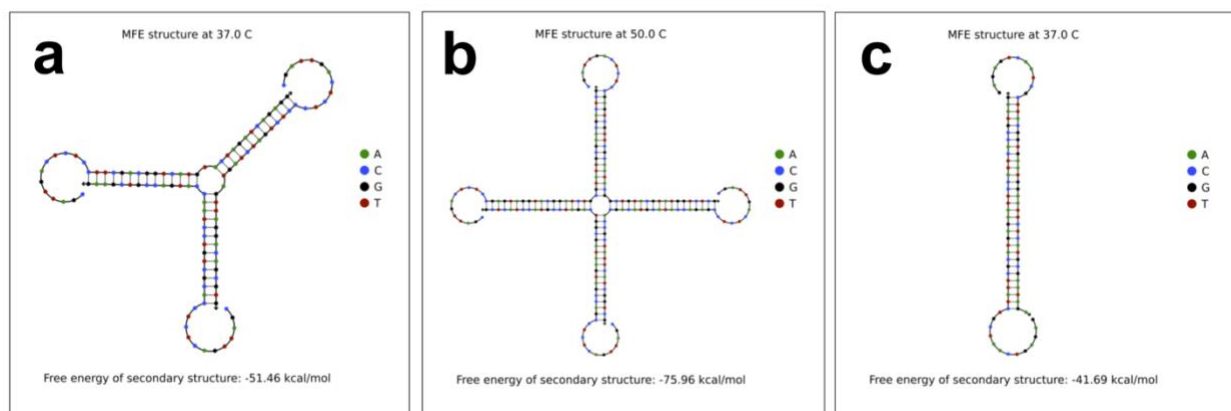


Figure 5.2 Structures of (a) Y-shaped DNA tiles, (b) X-shaped DNA tiles, and (c) spacers modeled by NUPACK software.

5.2.2 DNA-CNT conjugates

To construct DNA-CNT conjugates, we applied a DNA sequence containing multiple repeated GT units that wrap around CNTs. Specifically, we adopted Sequence C as reported by Cheng, *et al.*^[207] and modified their Sequence D with our sticky end to make it compatible with our spacers. The repeated GT units has been proved to efficiently wrap around CNTs well due to strong π - π interactions between the CNT sidewall and the nucleobase aromatic rings^[173,208]. Zheng, *et al.* also demonstrated a systematic study showing that among all DNA sequences that wrap around CNTs, $(GT)_n$ gives the highest dispersion efficiency and only requires 30 min sonication to obtain well-dispersed DNA-wrapped individual nanotubes^[182]. A longer sonication treatment breaks CNT and decreases their high aspect ratio^[209], which is a property essential to our objective of building percolating networks. Therefore, we chose to make DNA-CNT conjugates

with (GT)₂₀ repeat unit to allow a shorter sonication time. Strands of this length tightly wrap around nanotubes, while a longer DNA strand wraps around nanotubes more loosely and may also entangle multiple nanotubes^[210]. We examined both single-walled CNTs (SWNTs) and multi-walled CNTs (MWNTs) in this study. According to vendor specifications, the SWNTs have an average diameter of 0.78 nm with a median length of 1 μm. We chose these dimensions because previously reported AFM studies observed that (GT)₂₀ can form multiple wraps around SWNTs with an average diameter around 1 nm^[197]. We purchased MWNTs of much larger size with average outer diameter of 8.7–10 nm and an average length of 10 μm. The same study showed that DNA wrapping loosens as the nanotubes become larger and mostly only wraps with one turn around MWNT of greater diameters.

Both SWNTs and MWNTs were purchased from Sigma-Aldrich. HEPES, (4-(2-hydroxyethyl)-1-piperazineethanesulfonic acid), (>99.5%, Sigma-Aldrich) was also used to make buffer solutions. 120 μL HEPES (final concentration 50 mM, pH 7.6), 1.2 mg CNTs and 15 μL of 10 mM DNA strand C₁ were mixed together. The mixture was sonicated in an ice-water bath for 30 min using a 100W bath sonicator. Then, 15 μL of 10 mM DNA strand C₂ was added. The solution was incubated at room temperature overnight, then stored at 4°C. DNA modification on CNT also assists the solubilization of CNT. The dispersion of DNA-CNT conjugates in DI water is stable for weeks, while CNT without DNA modification would settle at the bottom of the container within 15 min after sonication.

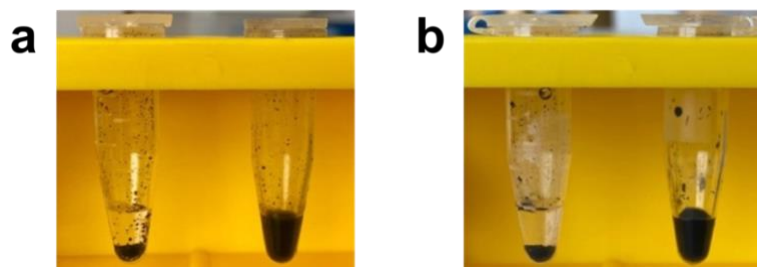


Figure 5.3 Photos of (a) SWNT and (b) MWNT dispersions in DI water without (left) and with (right) DNA modification.

5.2.3 DNA-AuNP conjugates

Lastly, we utilized DNA-AuNP conjugates as the fourth type of crosslinkers. We synthesized AuNPs with an average diameter of 13 nm using a method adapted from the standard citrate reduction procedures^[211]. For the synthesis, nitric acid (ACS reagent, Sigma-Aldrich) and hydrochloric acid (ACS reagent, Sigma-Aldrich) were used to make aqua regia. Hydrogen tetrachloroaurate (III) trihydrate (99.9%), sodium citrate tribasic dihydrate (ACS reagent, >99.0%) and sodium hydroxide (NaOH, >98%) were also purchased from Sigma-Aldrich.

First, all glassware was cleaned with aqua regia then rinsed with DI water. After the glassware was dried completely, 500 mL of 1 mM hydrogen tetrachloroaurate (III) trihydrate in DI water was prepared in a round-bottom flask and heated to a vigorous boil with stirring. Then, 50 mL of 38.8 mM sodium citrate tribasic dihydrate in DI water was added to the gold solution flask, and the reaction was allowed to proceed for 15 min. The solution turned from yellow to clear, to black, to purple, and finally to deep red (Figure 5.4). Lastly, the solution was cooled down to room temperature. Synthesized AuNP were characterized by transmission electron microscopy (TEM) as shown in Figure 5.8(a). The concentration of AuNP was estimated with UV-Vis spectrophotometer (Figure 5.5) and calculated with Beer-Lambert equation, $A = \epsilon bC$ ^[212]. A peak λ_{\max} at 519 nm

wavelength proves that these are well-formed AuNPs with an average diameter of 13 nm^[201]. UV-Vis was recorded on Thermo Scientific NanoDrop 2000c Spectrophotometer.



Figure 5.4 Photo of 13 nm AuNPs after synthesis.

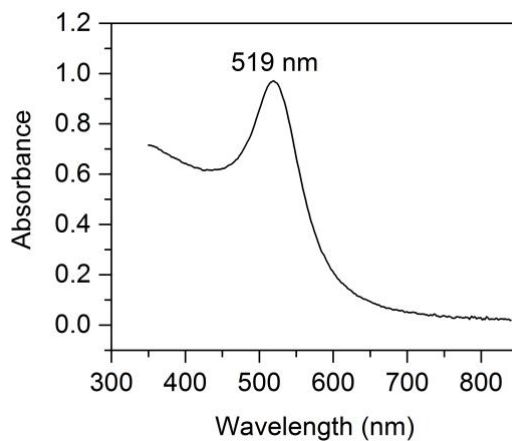


Figure 5.5 UV-Vis spectrum of as-synthesized AuNPs.

DNA-AuNP conjugates were synthesized with a previously reported method reported by Zhang, *et al.*^[213]. The conjugates were created by attaching ssDNA to the surfaces of AuNP. Briefly, 13 nm AuNPs at neutral pH adsorb DNA strands with polyadenine (A_n) as the anchoring block due to strong interaction between adenine and gold. We designed DNA sequence to contain 13-

mer of polyadenine (A₁₃) that is connected with a 12 nt sticky end. Polyadenine sequence strongly adsorbed onto AuNPs with high loading capacity. This method produced DNA-AuNP conjugates with much higher concentrations of DNA and AuNPs compared to another method prepared by polymerase-chain reaction (PCR) elongation^[172].

First, 16 μ L of DNA stock solution of sequence G (100 μ M in 5 mM HEPES buffer, pH 7.4) was added to 1.6 mL AuNP solution (10 nM). The solution was mixed by brief vortexing. Then, 32 μ L of 500 mM citrate·HCl buffer, pH 3, (final 10 mM) was added to the AuNP solution (1 μ L of buffer per 50 μ L of AuNP solution). The solution once again went through vortex mixing and was incubated at room temperature for 3 min. Then, the pH of the AuNP solution was adjusted back to neutral by adding 96 μ L of 500 mM HEPES buffer (pH 7.6, 3 μ L of buffer per 50 μ L of AuNP solution). The solution was then incubated for 5 to 10 min at room temperature. The DNA-AuNP mixture was centrifuged at 13,300 rpm for 6 min, and the supernatant was removed and discarded. The pellet was washed four times with 5 mM HEPES buffer (pH 7.6) and centrifuged to remove any unbound DNA strands. The final DNA-AuNP conjugate was redispersed in 100 μ L of 5 mM HEPES buffer (pH 7.6) for further use.

5.2.4 Construction of pure DNA hydrogels and DNA hydrogel composites

Table 5.2. Concentrations and ratios of crosslinkers and spacers to prepare for hydrogels.

Name	Concentrations of strands with sticky end in the stock solutions	Ratios of final concentrations in the hydrogels
Spacers (S)	1.5 mM	N/A
Y-shaped DNA tile (Y)	1 mM	Y:S = 2:3
X-shaped DNA tile (X)	1 mM	X:S = 1:2
DNA-CNT conjugates	1 mM	DNA-CNT:S = 2:1
DNA-AuNP conjugates	16 μ M	DNA-AuNP:S = 1:10

To construct hydrogels using the self-assembled DNA tiles or DNA/nanomaterials conjugates, and spacers, desired volumes of crosslinker and spacer stocks were combined on a piece of parafilm using the concentrations and ratios listed in Table 5.2. For example, to make a 20 μL Y-shaped DNA tiles-based hydrogel, 10 μL of Y-shaped DNA tiles stock and 10 μL of spacer stock were added on a piece of parafilm and immediately mixed. DNA hydrogels were formed within one minute. The final system was also modeled and analyzed by NUPACK software during design. Figure 5.6 below gives an example of the combination of a Y-shaped DNA tile and a spacer. The photo of hydrogels was taken with a cell phone and shown in Figure 5.7. All the DNA gel samples were immediately used and tested once they were formed.

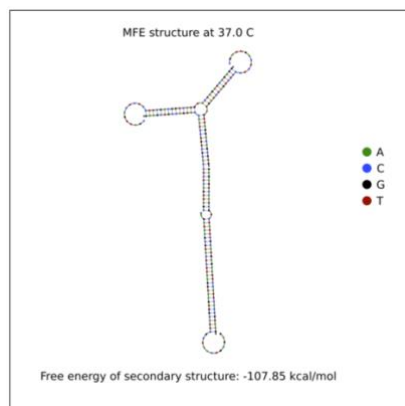


Figure 5.6 Structure composed of a Y-shaped DNA tile and a spacer modeled by NUPACK software.



Figure 5.7 Photo of pure DNA hydrogels and DNA hydrogel composites constructed by SI with (from left to right) Y-shaped DNA tiles, X-shaped DNA tiles, DNA-SWNT conjugates, DNA-MWNT conjugates, and DNA-AuNP conjugates.

5.3 Characterizations of conjugates and hydrogels

The dimensions and morphology of AuNPs, DNA-AuNP conjugates, DNA-CNT conjugates, and dehydrated DNA hydrogel composites were imaged by a transmission electron microscope FEI Talos F200X at an accelerating voltage of 200 kV. CNT samples were drop cast and dried onto 300-mesh copper grids with lacey formvar support film reinforced by a heavy coating of carbon (Ted Pella, 01883). AuNP samples were prepared on 200-mesh copper grids with a formvar film covered with a light layer of carbon (Ted Pella, 01800-F). Dimensions of the imaged samples were measured with ImageJ software.

To understand and compare the morphologies of conjugates and hydrogels, we used TEM imaging techniques to visualize AuNPs, SWNT, and MWNT conjugates with and without DNA spacers to show how the crosslinked DNA networks connect and arrange the structures of these nanomaterials.

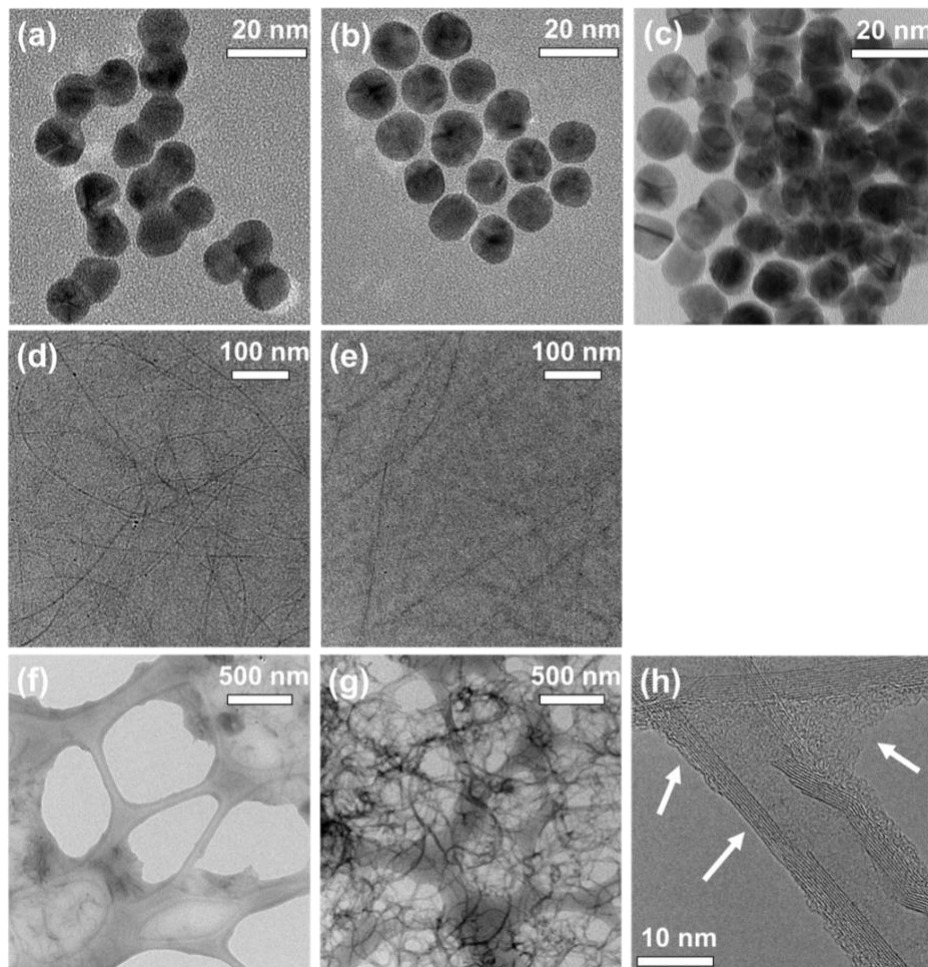


Figure 5.8 TEM images of (a) as-synthesized AuNPs, (b) DNA-AuNP conjugates, (c) DNA-AuNP hydrogel; (d) DNA-SWNT conjugates, (e) DNA-SWNT hydrogel; and (f) DNA-MWNT conjugates on lacey film, (g) DNA-MWNT hydrogel on lacey film, and (h) a zoomed-in image of DNA-MWNT hydrogel, showing areas of the CNT wall wrapped by DNA and the bare wall without DNA wrapping. DNA binding between CNT junctions is also shown.

We first imaged the original AuNPs right after synthesis, then DNA-AuNP conjugates and DNA-AuNP hydrogel. The TEM images of citrate-stabilized AuNPs demonstrate that synthesized nanoparticles were homogeneous and that their average diameter was 13.1 ± 1.8 nm (Figure 5.5 and Figure 5.8(a)). As-synthesized AuNP appeared clustered in groups of two or three with no

clear spaces between individual nanoparticles within the groups. However, the images of DNA-AuNP conjugates showed that DNA-attached AuNPs have a clear and much more uniform spacing between neighboring particles, which was measured to have an average of 0.78 nm (Figure 5.8(b)). By comparing the morphologies of AuNP clustering in Figures 5.8(a) and 5.8(b), we showed that DNA strands modified surfaces of AuNPs. Next, we constructed DNA-AuNP hydrogel by combining DNA-AuNP conjugates and SI spacers. The TEM image (Figure 5.8(c)) showed multiple layers of AuNPs on top of each other that appeared to be held together during sample collapse from drying. Comparing that with Figure 5.8(b), it is apparent that DNA spacers had linked AuNP together in a 3D structure.

To prove that DNA strands have attached on AuNP surfaces, we further characterized AuNPs and DNA-AuNP conjugates using gel electrophoresis. Gel electrophoresis (Agarose, 1%) was carried out in 0.5x TBE buffer (Tris-Borate-EDTA buffer)^[214]. First, 1g of agarose powder was added to 100 mL of 0.5x TBE buffer, and the solution was heated in the microwave for 60 seconds until it became homogeneous and transparent. Then, the agarose solution was casted in a gel tray (Bio-Rad Sub-Cell GT) until solid. To prepare for the samples, glycerol (final content 10%) was added to AuNPs and DNA-AuNP conjugate stocks, then 10 μ L of each of the stocks was loaded in a well in the agarose gel. The gel was run for 1 hour at 100V in the 0.5x TBE buffer using Bio-Rad PowerPacTM Basic Power Supply. The corresponded electric field was 9.9 V/cm. After gel electrophoresis, a cell phone was used to take a digital picture of the gel to visualize the mobilities of AuNPs and DNA-AuNP conjugate samples in the gel (Figure 5.9). Non-DNA-attached AuNP aggregated in the well and failed to enter the gel. DNA-modified AuNP did not aggregate and were able to migrate into the gel. TEM images agreed with gel electrophoresis results and demonstrated that we successfully decorated AuNP with ssDNA.

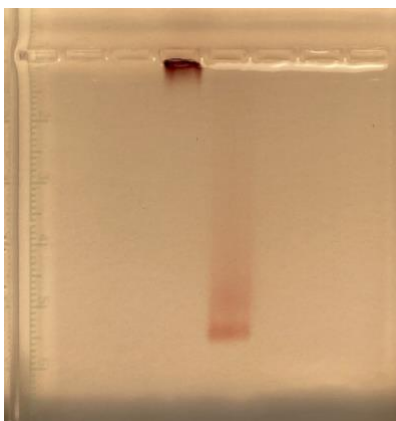


Figure 5.9 The band of pure AuNPs (left) appears violet under visible light, while the band of DNA-AuNP conjugates (right) retains the red color and shows a much better mobility.

With the same concept, we also imaged DNA-SWNT conjugates and DNA-MWNT conjugates, then took a look at hydrogels made of these conjugates with SI. The TEM images of DNA-CNT hydrogels showed that amorphous materials with hierarchical structures were formed. We can clearly see the larger-scale CNT networks as well as DNA binders on the surfaces of nanotubes especially around the junctions of CNT (Figure 5.8(g) and Figure 5.8(h)). Although differences in clustering and morphology between DNA-SWNT in conjugates versus hydrogel are not entirely distinctive using TEM characterization (Figure 5.8(d) and Figure 5.8(e)), the differences were apparent in the MWNT samples (Figure 5.8(f) and Figure 5.8(g)). DNA-MWNT conjugates appeared to gather on the lacy carbon film on the copper grids and did not appear to fill in most holes in the film. On the other hand, the dehydrated hydrogel made of DNA-MWNT conjugates with SI spacers covered over the entire lacy film (including holes in the film) with its own networks formed by the nanotubes. DNA spacers helped to connect MWNTs together into a web-like structure over a large area. When taking a closer look at individual MWNT, we observed regions of coating over the nanotube with an average thickness of 1.51 nm. Figure 5.8(h) clearly

showed that the middle area of the MWNT was not wrapped by DNA, while the areas close to MWNT junctions were coated. Figure 5.8(h) also showed thicker coating around MWNT junctions, indicating the location of spacers. These images represent a direct observation of DNA acting as a “smart” glue to bind and connect MWNT together. Overall, we successfully constructed pure DNA hydrogels and DNA hydrogel composites with nanomaterials.

5.4 Mechanical studies

5.4.1 Rheological properties of DNA hydrogels

Polymeric hydrogels generally demonstrate robust mechanical strength because of their dense, entangled, and crosslinked networks with small mesh sizes. Unlike these conventional hydrogels, pure DNA hydrogels are more thixotropic and can display poor mechanical strength^[215]. Although the mechanical properties of DNA hydrogels can be fine-tuned by adjusting the type and concentration of initial DNA tiles with different number of branches, even the toughest DNA hydrogel only exhibits a storage modulus of a few thousands Pa^[202]. Because of this property, the applications of DNA hydrogels are limited to only certain fields. To explore further enhancement of DNA hydrogels' mechanical strength, we implemented two strategies: modifying the DNA building blocks and fortifying the structure with novel nanomaterials that confer mechanical rigidity.

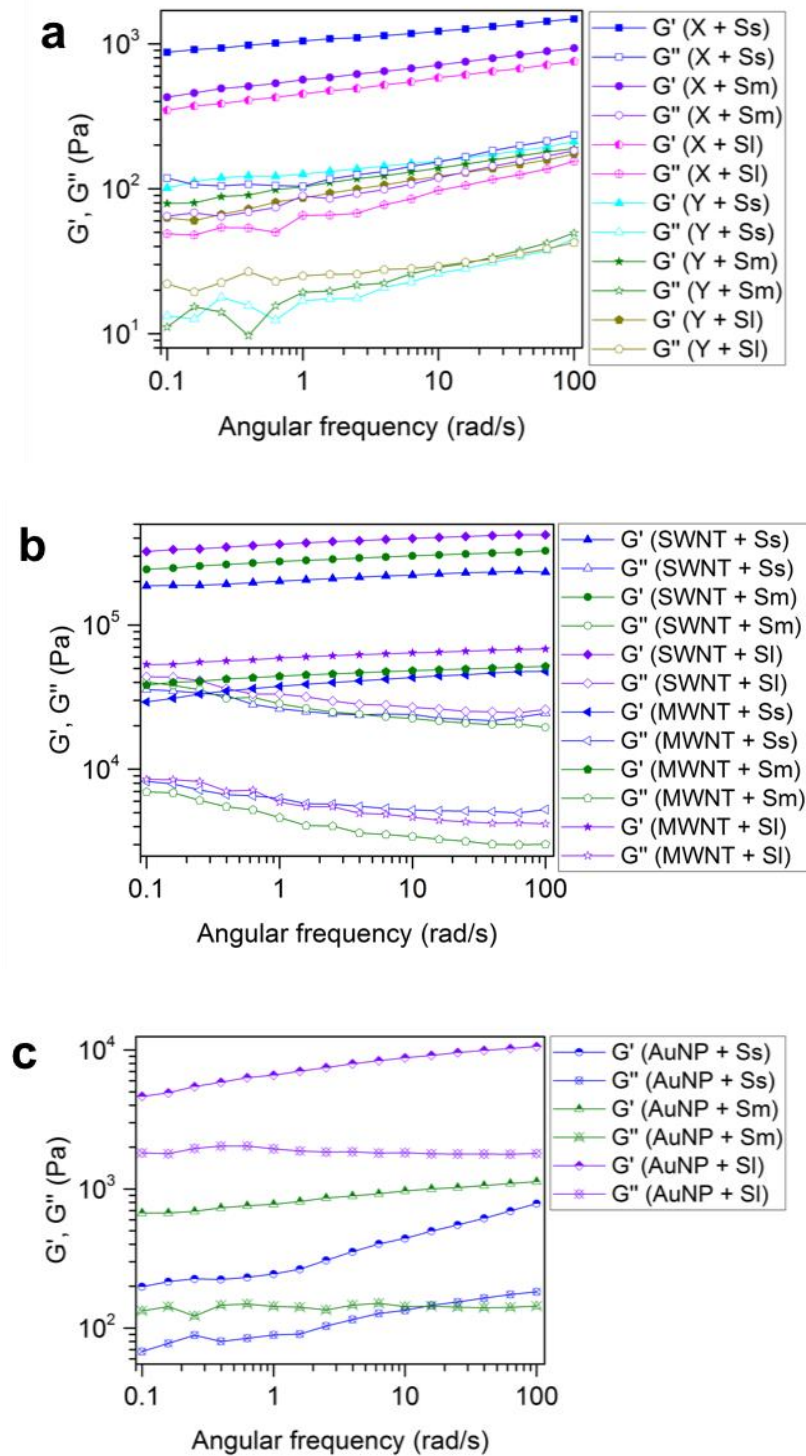


Figure 5.10. G' , G'' vs. angular frequencies showing the rheological properties of (a) pure DNA hydrogels, (b) DNA-SWNT and DNA-MWNT hydrogels, and (c) DNA-AuNP hydrogels constructed with spacers of different lengths.

We performed oscillation measurements on hydrogels formed by Y-shaped DNA tiles, X-shaped DNA tiles, DNA-SWNT conjugates, DNA-MWNT conjugates, and finally DNA-AuNP conjugates with spacers of three different lengths. The goals of this group of tests are to study the influence of length of spacers on different types of crosslinkers, as well as to compare the influence of different crosslinkers. For all tested samples, we see a higher storage modulus (G') than loss modulus (G'') across tested angular frequencies as shown in Figure 5.10 demonstrating solid-like behavior, which is typically observed for hydrogels constructed with DNA^[216-217].

As Figure 5.10(a) shows, when constructing pure DNA hydrogels with the same crosslinkers (X or Y), using shorter spacers gives more solid-like hydrogels as indicated by higher storage modulus. X-shaped DNA tiles also construct more solid-like hydrogels than Y-shaped DNA tiles with all types of spacers. However, when using conjugates as crosslinkers (see below), longer spacers construct more solid-like hydrogels, opposite to the behavior observed from pure DNA hydrogels. The mechanical strengths of pure hydrogels are also improved by integrating nanomaterials. With the same spacers (SI), DNA-SWNT conjugates also construct more solid-like hydrogels than DNA-MWNT conjugates, and both DNA-CNT conjugates make more solid-like hydrogels than DNA-AuNP conjugates (Figure 5.10).

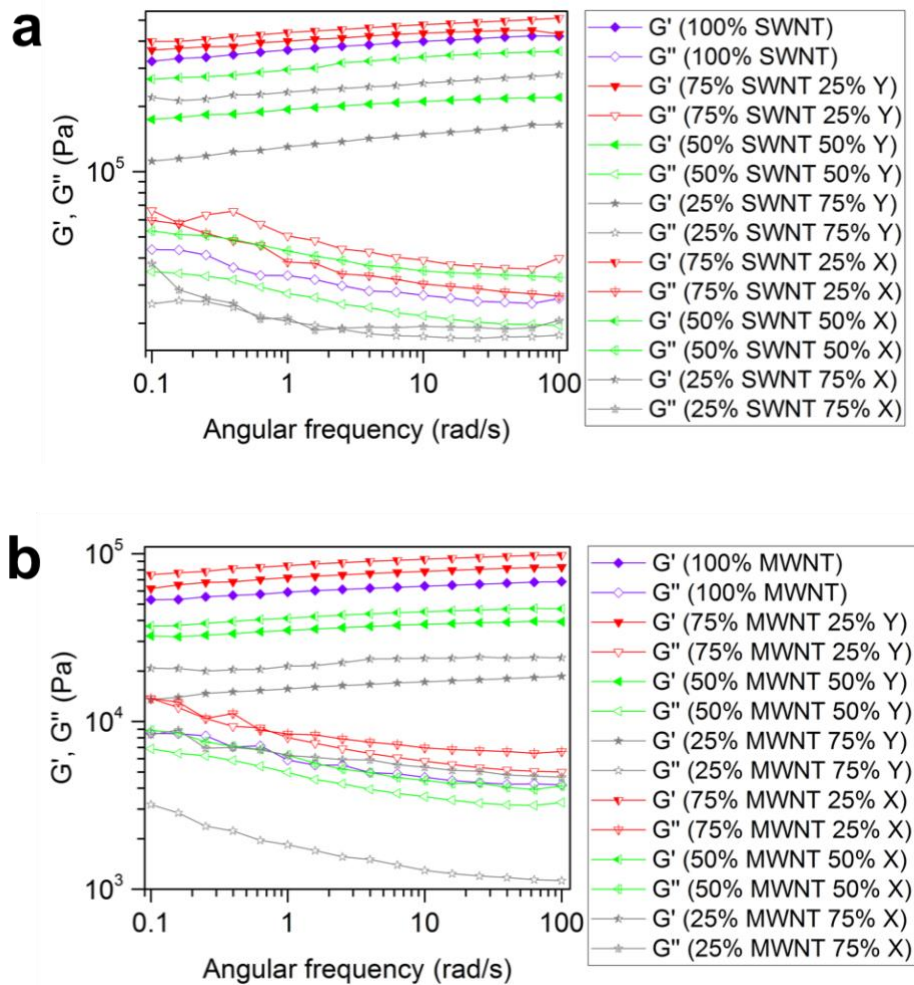


Figure 5.11 G' , G'' vs. angular frequencies showing the rheological properties of (a) hydrogel composites constructed with DNA-SWNT conjugates, X- (or Y-) shaped DNA tiles, and SI; and (b) hydrogel composites constructed with DNA-MWNT conjugates, X- (or Y-) shaped DNA tiles, and SI.

Our next set of tests was to use mixed crosslinkers, combining DNA-CNT conjugates and DNA tiles. The objective of this test is to show the influence of different crosslinker compositions and see how mixed crosslinkers of different length scales change the mechanical properties of the final hydrogels. Specifically, we substituted 25%, 50%, and 75% of the DNA-CNT conjugates

from the previous test with X-, or Y-shaped DNA tiles while keeping the total concentration of sticky ends from all crosslinkers the same. Only long spacer (SI) was used for these mixed crosslinker tests. The oscillatory measurements showed that hydrogels constructed using SI contained crosslinker mixture of 75% DNA-CNT conjugates and 25% DNA tiles exhibited the highest values of G' . This composition formed hydrogels with G' above 50 kPa, over 100-fold higher than G' of pure hydrogels. It is followed by using SI with 100% DNA-CNT conjugates as crosslinkers. Then, the mechanical strength dropped even further when using SI with 50% DNA-CNT conjugates and 50% DNA tiles crosslinkers, and hydrogels constructed by SI with 25% DNA-CNT conjugates and 75% DNA tiles had the lowest storage modulus. All DNA hydrogel composites still had higher mechanical strengths than pure DNA hydrogels. Moreover, using DNA-SWNT conjugates always gave more solid-like hydrogels than using DNA-MWNT conjugates in the above compositions, and using X-shaped DNA tiles resulted in more solid-like hydrogels than using Y-shaped DNA tiles in these compositions.

We would like to construct hydrogels of reasonable mechanical strength where the crosslinked networks can effectively prevent diffusion of the nanomaterials, and thus to achieve hydrogels with confined architecture for further applications. Having a higher storage modulus than loss modulus from oscillation frequency tests indicated that we indeed made hydrogels with solid-like properties. When using the same DNA tiles as crosslinkers, we observed that shorter spacers constructed hydrogels of higher mechanical strengths as they are able to build a denser network. The situation is reversed and longer spacers constructed more solid-like hydrogels when using DNA/nanomaterial conjugates as crosslinker. This is because CNTs and AuNPs we used are much larger in scale compared to DNA molecules, thus having longer spacers helped to build more

or more stable bridges between nanomaterial/crosslinker components. Therefore, we used SI for all electrical studies and structural characterization analysis.

CNTs are well known for their mechanical reinforcement applications. Consistent with previous observations in other composites, we observed a huge increase in storage modulus with hybrid DNA-CNT hydrogels compared to pure DNA hydrogels. When using one type of crosslinkers, DNA-SWNT conjugates constructed the most solid-like hydrogels, followed by using DNA-MWNT conjugates, DNA-AuNP conjugates, X-shaped DNA tiles, and finally Y-shaped DNA tiles. We believe that we observed higher storage modulus from hydrogels constructed with DNA-SWNT conjugates than hydrogels constructed with DNA-MWNT conjugates because DNA wraps around SWNTs more tightly with more turns^[218]. TEM images (Figure 5.8) also showed that DNA coats on SWNTs much better than on MWNTs. As the average diameter of CNTs increases from SWNTs (0.78 nm) to MWNTs (~9 nm), (GT)₂₀ loses its strong binding around the nanotubes, which resulted in a decrease in mechanical performance of hydrogels made with these conjugates. This result shows the importance of crosslinked DNA as the binding material to connect nanomaterials and to build networks. Furthermore, hydrogels constructed with both types of DNA-CNT conjugates crosslinkers showed higher mechanical strength than hydrogels constructed with DNA-AuNP conjugates because the high aspect ratios of CNTs are inherently in favor of providing reinforcement to composites compared to sphere-shaped materials.

We further investigated and rationally improved the mechanical properties of hybrid hydrogels by combining DNA/nanomaterial conjugates and DNA tiles as crosslinkers. Since CNTs and AuNPs are in much larger scales than DNA molecules, there are available spaces between individual nanotubes and nanoparticles in the hydrogels, where there is no DNA filling besides the DNA network associated with binding strands and spacers. These hydrogels have the capacity to

integrate more materials that can fill in the spaces. Therefore, we used different compositions of DNA/nanomaterial conjugates and DNA tiles to construct hydrogels in which crosslinkers come in different scales. When we used DNA tiles to make up to 25% of crosslinkers and DNA-CNT conjugates for the rest, the resulted hydrogels are even more solid-like than when using 100% DNA-CNT conjugates as crosslinkers. This is because substituting some of the DNA-CNT conjugates with a much smaller type of crosslinkers helped to fill in the open spaces between CNTs, and thus made a denser hydrogel. However, DNA molecules are significantly weaker than CNTs, so we observed a decrease in mechanical strength when substituting more DNA-CNT conjugates with DNA tiles.

To better present the influence of crosslinker type on the overall rheological properties of the hydrogels, Figure 5.12 was made to show the storage modulus measured at 100 rad/s (Figure 5.12(a)) and at 0.1 rad/s (Figure 5.12(b)) of hydrogels made with different types of crosslinkers. In summary, we demonstrated adjusting the mechanical properties of hybrid hydrogels by combining different compositions of crosslinkers, and achieved the most solid-like hydrogel when using DNA-CNT conjugates as 75% of crosslinkers and X-shaped DNA tiles for the rest 25% of crosslinkers.

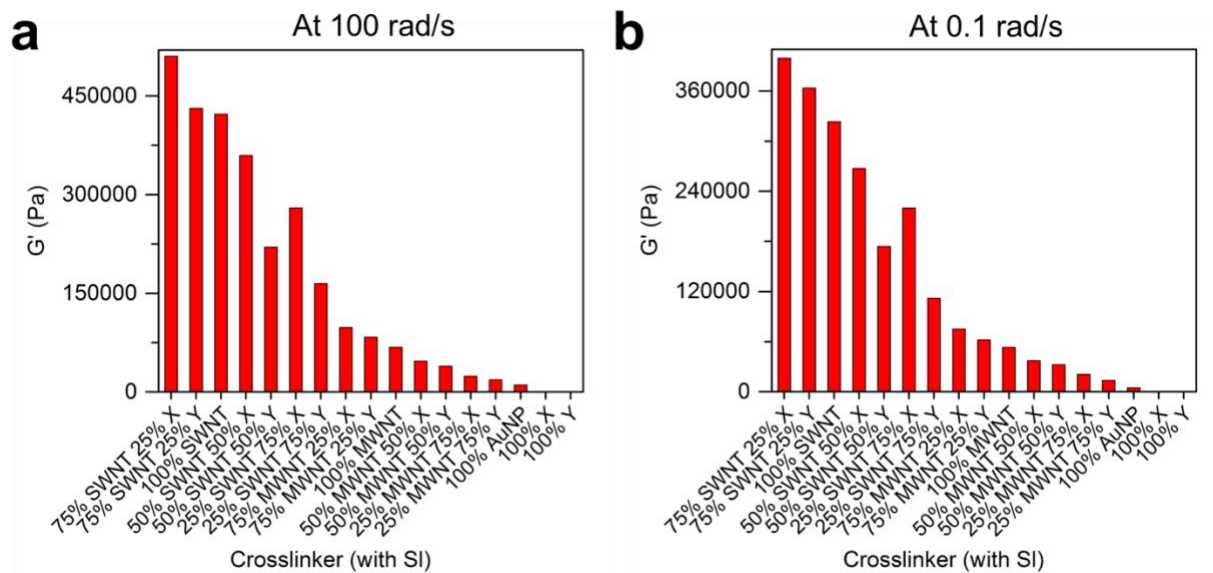


Figure 5.12 Comparison of G' of different types of hydrogels, measured at (a) 100 rad/s and (b) 0.1 rad/s.

5.4.2 Microrheological properties of DNA hydrogels

Our viscoelastic samples are at the low end that is measurable with rheology and are also at the high end that can be measured with microrheology. Therefore, we further investigated the mechanical properties of the hydrogels with microrheology, especially with the multiple particle tracking (MPT) method. MPT is a passive microrheology technique that simultaneously tracks multiple micron-sized particles (beads) in the sample using recorded video microscopy^[219].

Here, the viscoelasticity of DNA-CNT conjugate and DNA-CNT hydrogel was studied with MPT using an inverted fluorescence microscope. The Brownian motion of the tracer particles, green fluorescent polystyrene microspheres, was tracked. Before the measurement, the tracer particles were embedded inside the samples by adding them to the crosslinker stock. After a sample is loaded, a video of these fluorescent particles was monitored and recorded. Movies of the fluctuating particles were further analyzed by a custom MPT routine written in Python based on a

widely used particle tracking algorithm^[211]. The program is able to exact trajectories of individual tracer particles from the recorded movies, where the trajectory maps show the displacements of the centers of individual particles that are simultaneously tracked in the focal plane of the microscope. From the trajectories of particle centers, individual time-lag averaged mean-square displacements (MSD) were computed. MSD characterizes the dynamics and mobility of the particles and shows the amplitude of the particle's motion. Therefore, MSD reflects the mechanical properties of the sample that the particles are embedded in.

We adapted a method reported by Oelschlaeger *et al.* to conduct MPT^[220]. First, 2.36 mL of FluoSphere polystyrene beads (1 μm diameters, orange (540/560), Invitrogen by Thermo Fisher) were washed by DI water with a repeat process of centrifugation and redispersion to remove any chemical residuals in the stock of bead solution. Then, the bead stock solution was centrifuged at 13.4 rpm to take out extra water, and the pellet of beads was added to a 60 μL sample to achieve a volume fraction around 0.02%. The sample was then loaded into one cell of an eight-well plate (Lab-Tek II chambered #1.5 German Coverglass System) to be monitored by the confocal laser scanning microscopy (Leica SP8 CLSM) in an $127 \times 127 \mu\text{m}$ field of view, at a rate of 40 frames/s. Displacements of the centers of particles from the recorded videos were analyzed by a customized program adapted from the MPT algorithm Trackpy^[221], which is based on the widely used Crocker and Grier tracking algorithm.

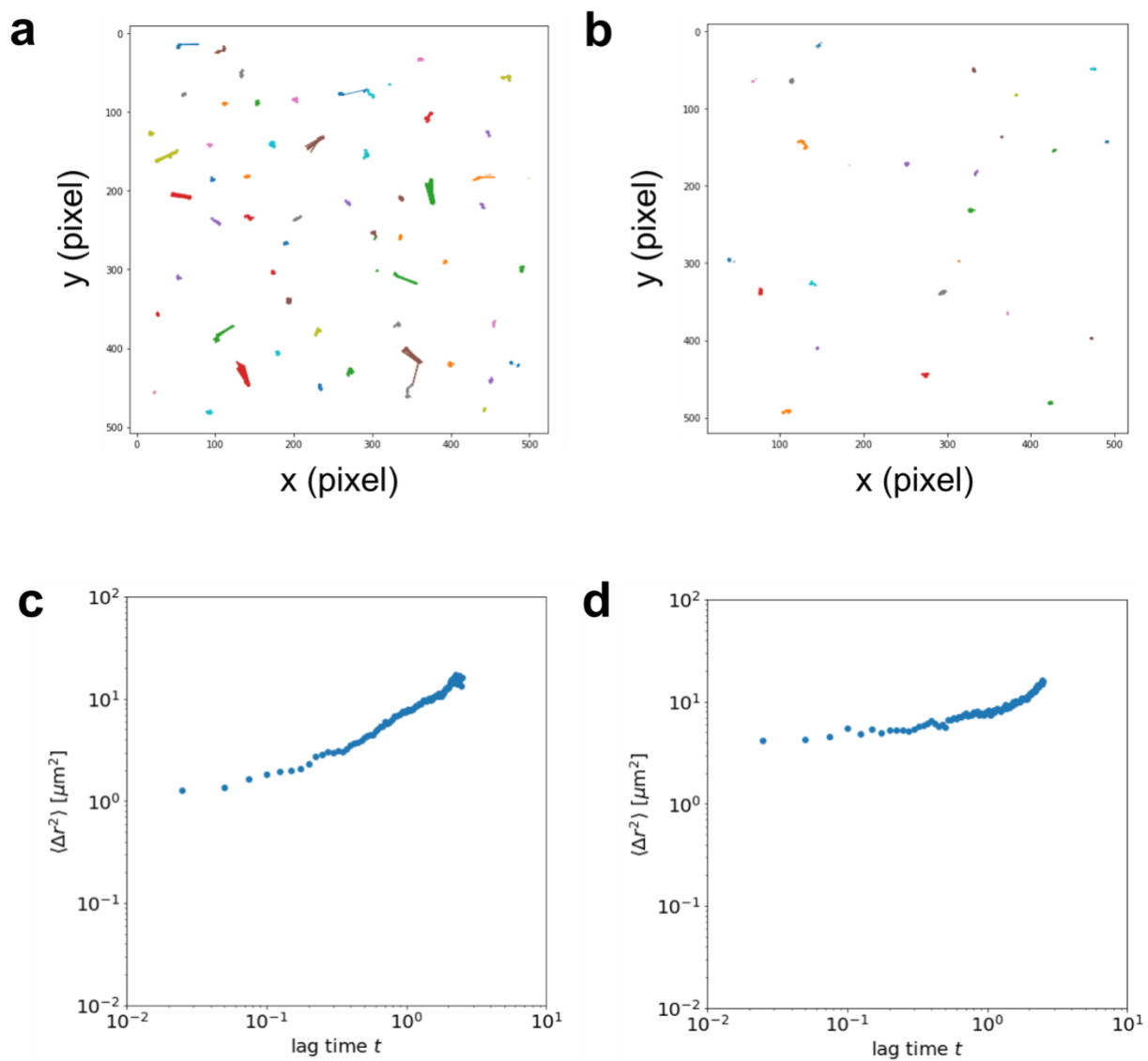


Figure 5.13 Trajectory maps of (a) DNA-SWNT conjugates and (b) DNA-SWNT hydrogel. Average MSD vs. lag time of (c) DNA-SWNT conjugates, with a fitted slope of 0.683, and (d) DNA-SWNT hydrogel, with a fitted slope of 0.327.

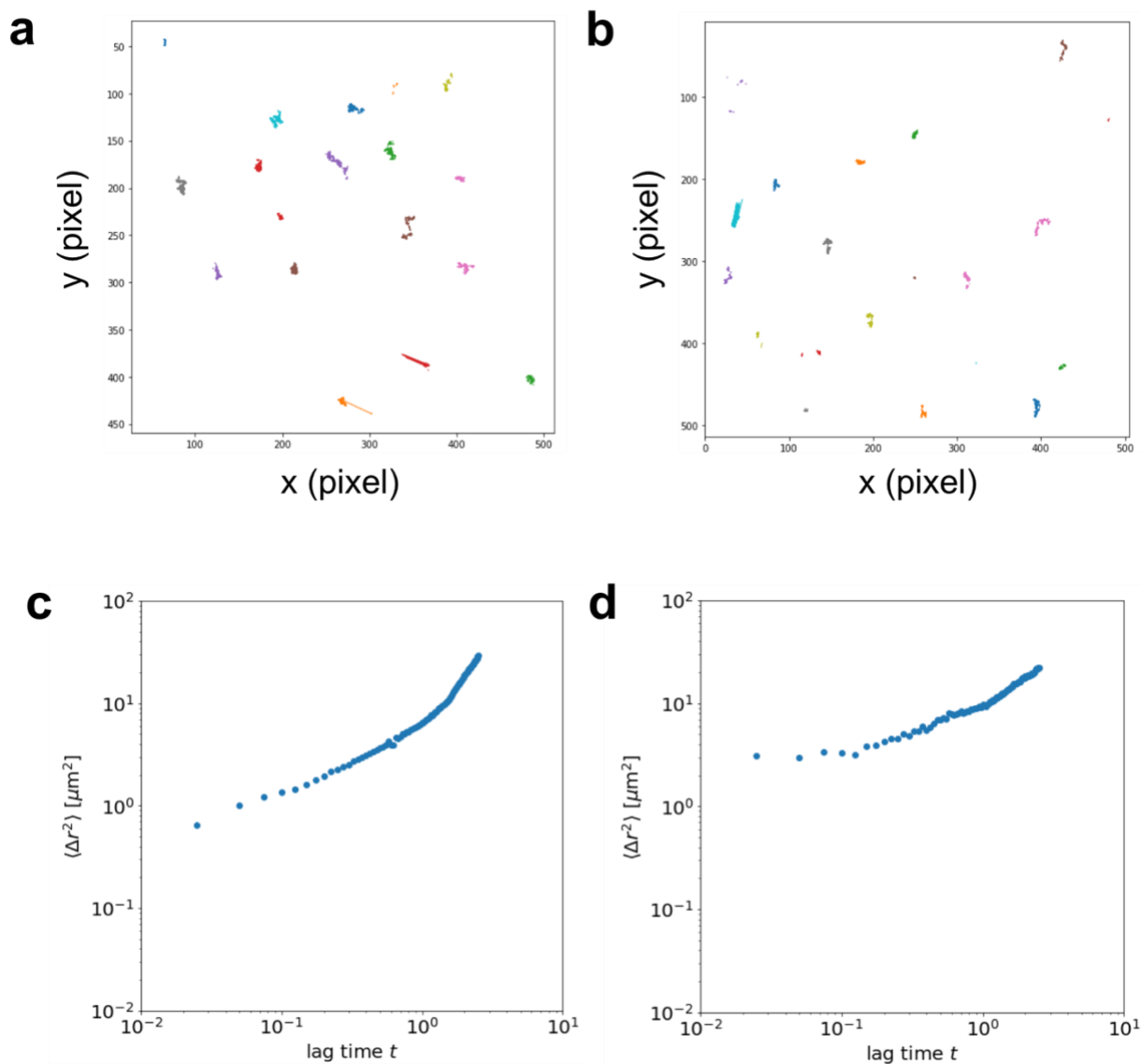


Figure 5.14 Trajectory maps of (a) DNA-MWNT conjugates and (b) DNA-MWNT hydrogel. Average MSD vs. lag time of (c) DNA-MWNT conjugates, with a fitted slope of 0.911, and (d) DNA-MWNT hydrogel, with a fitted slope of 0.558.

We used MPT to analyze two types of samples: (1) DNA-CNT conjugates and (2) DNA-CNT hydrogels comprised of the conjugates and the longest spacers. The objective of this study is to compare the mobility of fluorescent particles in order to investigate the microstructure of the

samples that they are embedded in. We used both SWNT and MWNT samples for this set of study. The first output of MPT are trajectories of different particles in the 2D plane that is in focus during video recording. They are individually measured, and the trajectories of the particles are illustrated with different colors in Figure 5.13(a)(b) and Figure 5.14 (a)(b) to track the movement of the particles. By comparing (a) and (b) in both Figure 5.13 and Figure 5.14, we can directly observe a decrease in mobility of the particles as DNA spacers are added to the crosslinkers. It is especially obvious in the SWNT sample, showing that adding spacers to the crosslinkers gives a greater reinforcement on the elastic properties when using SWNT. This result echoes with the measurement oscillation frequency test that DNA-SWNT hydrogel is more solid-like than DNA-MWNT hydrogel and MWNT samples give rise to more liquid-like properties due to their flexible backbone.

After getting the trajectory maps, the particles are analyzed as a group, and an averaged quantity, MSD, is calculated. We then used the program to plot the ensemble average of MSD versus lag time for the particles that are in focus during video recording, as shown in Figure 5.13(c) and (d), as well as Figure 5.14 (c) and (d). From the SWNT samples, the fitted slope of $\langle \text{MSD} \rangle$ decreased from 0.683 given by the DNA-SWNT conjugates to 0.327 given by the DNA-SWNT hydrogel. And the slope dropped from 0.911 given by the DNA-MWNT conjugates to 0.558 given by the DNA-MWNT hydrogel. In both cases, we also observed a slower rate of growth of $\langle \text{MSD} \rangle$ over lag time after adding spacers to the conjugates and forming a hydrogel. A decreased slope and growth rate indicate that the elastic properties of the materials are reinforced after adding spacers, and that the material becomes more viscous. In addition, a smaller slope from the SWNT samples also indicates that SWNT-based gels are more viscous than the MWNT-based gels. These observations agree with the rheological results that the DNA-SWNT hydrogel is more solid-like

than DNA-MWNT hydrogel. Overall, the MPT analysis also implies that a reinforced network is formed after adding DNA spacers to the crosslinkers.

5.5 Electrical studies

In order to minimize undesired complications due to ionic conduction associated with performing electrical measurements on nanocircuits embedded within hydrogels, we performed two-dimensional measurements of dehydrated hydrogels instead. We used two-terminal current-voltage (IV) characterization setup with parallel line-shaped gold electrodes fabricated via thin film vapor deposition by Dr. Eric Vetter from Dali Sun Lab. As shown in Figure 5.15, the gold microelectrodes of parallel lines were fabricated with defined widths and gap distances (spacings) that are either 100 μm or 200 μm . To perform IV curve measurement, the microelectrodes were wire bonded to a commercial BGA board that is connected to a socket board in a Faraday cage (Hewlett Packard Test Fixture Analyzer 16058A) connected to a 2 channel (medium power) source/monitor unit module (Agilent Technologies E5272A).

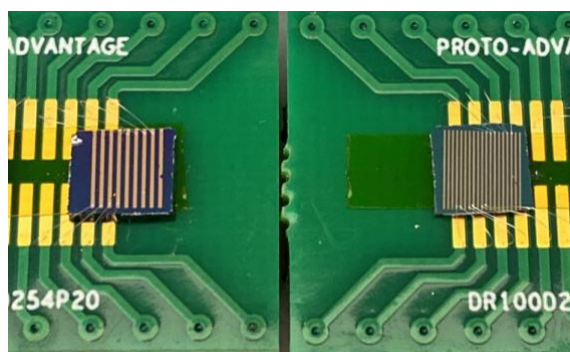


Figure 5.15 Gold electrodes of 200 μm spacings (left) and 100 μm spacings (right) for electrical characterization.

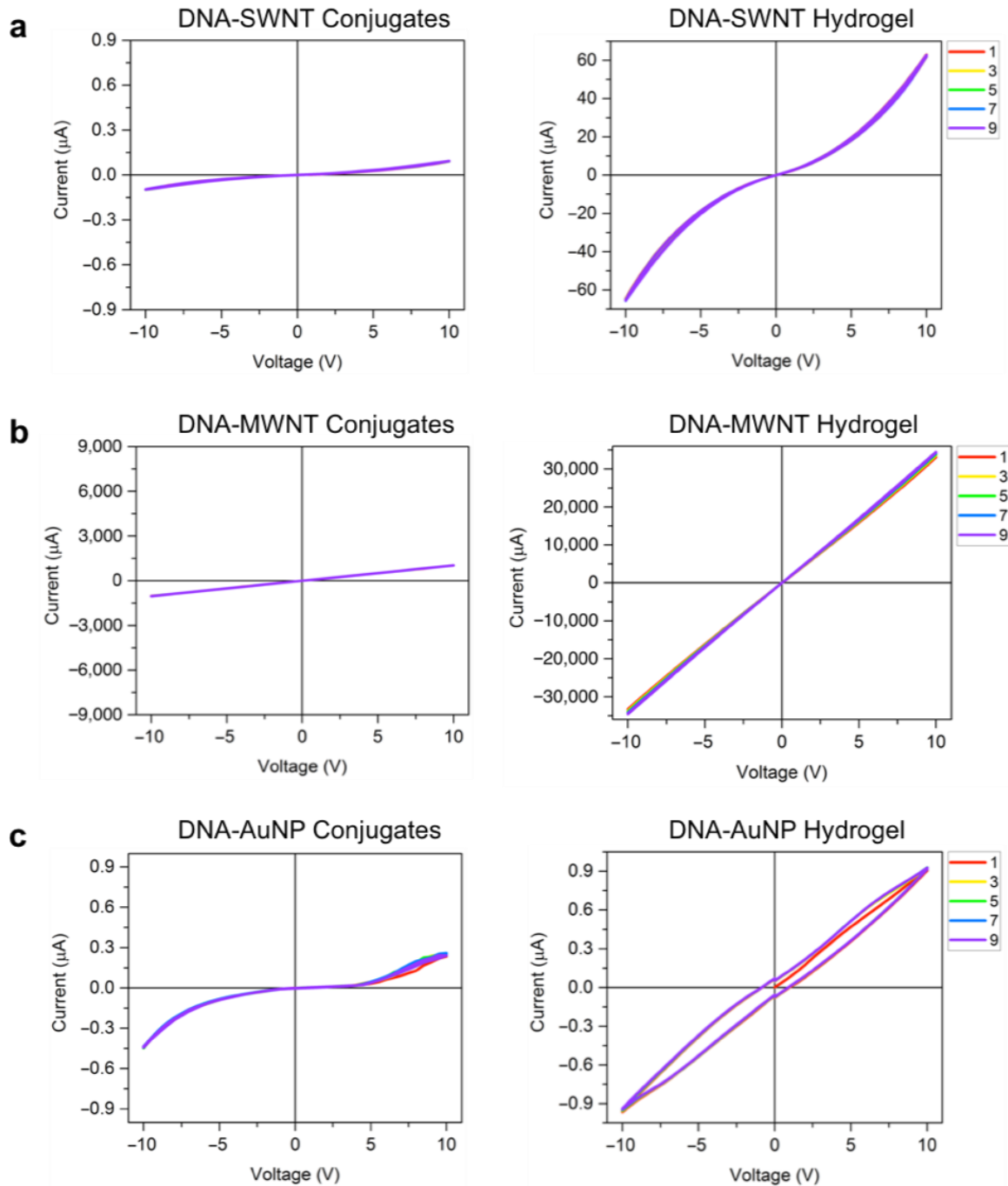


Figure 5.16 IV curves of dehydrated samples (a) DNA-SWNT conjugates (left) vs. DNA-SWNT hydrogel (right), (b) DNA-MWNT conjugates (left) vs. DNA-MWNT hydrogel (right), (c) DNA-AuNP conjugates (left) vs. DNA-AuNP hydrogel (right) measured across gold electrodes with 200 μm spacings. Legend shows pulse number.

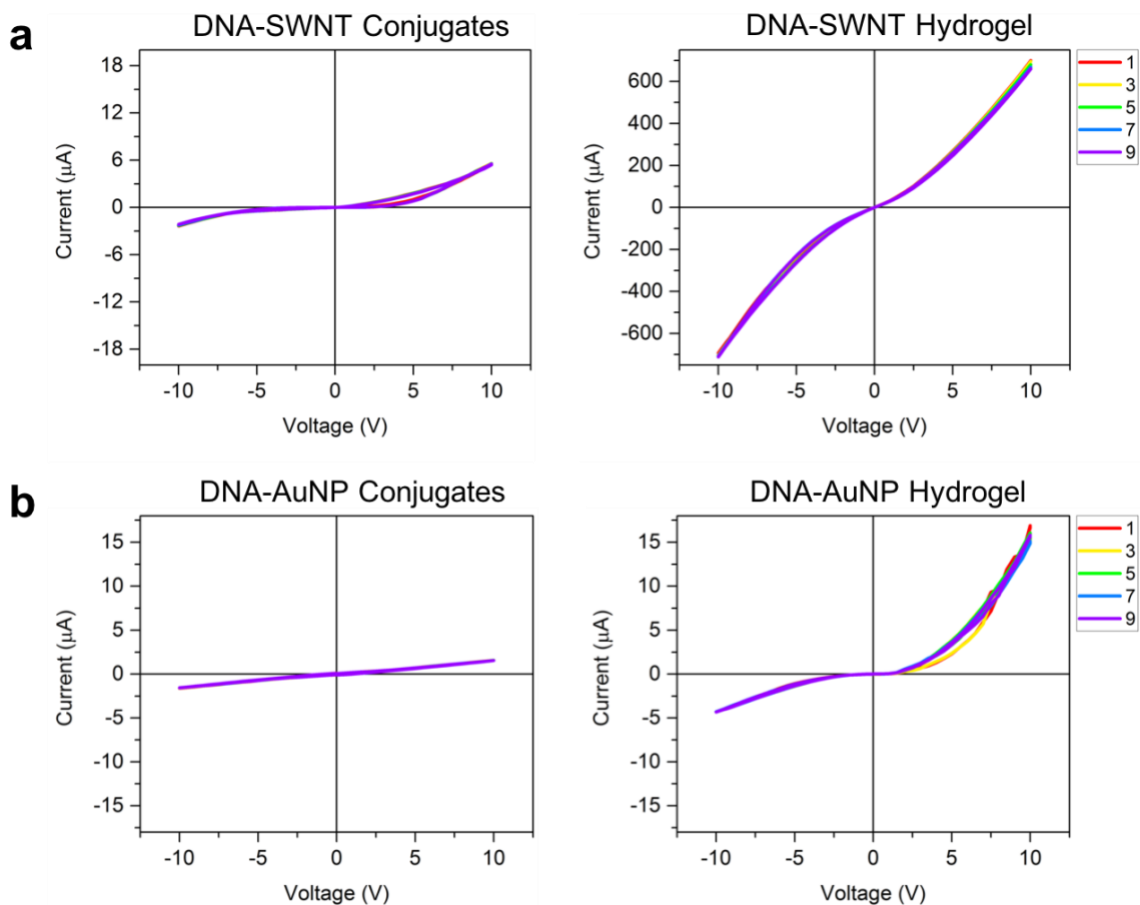


Figure 5.17 IV curves of dehydrated samples (a) DNA-SWNT conjugates (left) vs. DNA-SWNT hydrogel (right), (b) DNA-AuNP conjugates (left) vs. DNA-AuNP hydrogel (right) measured across gold electrodes with 100 μm spacings. Legend shows pulse number.

The hydrogel was placed across the gap between microelectrodes and then dried completely before IV curves were recorded. IV characterization allows the measurement of small conductivity as a response to an applied voltage. During the test, the current was measured during 10 consecutive pulses of 10V. The goal of IV characterization is to investigate whether or not DNA crosslinking creates more organized or clumpy networks based on the changes in conductivity after adding spacers to the conjugates.

As shown in Figure 5.16 and Figure 5.17, dehydrated samples of DNA-SWNT conjugates and DNA-SWNT hydrogel both showed nonlinear behaviors. With the same applied voltage pulses, the measured current increased greatly in the hydrogel samples with spacers compared to DNA-SWNT conjugates—over a 650-fold increase when measured across 200 μm spacings and 130-fold increase in the positive pulses measured across 100 μm spacings. Since MWNT are highly conductive, they showed a wire-like behavior with a much higher conductivity compared to the SWNT samples. In the MWNT case, adding DNA spacers also increased the conductivity of DNA-MWNT conjugates by 45-fold, see Figure 5.16(b). When testing with DNA-AuNP samples with electrodes of 200 μm spacings, current increased 4-fold after adding spacers to the conjugates and forming gel-like networks, as shown in Figure 5.16(c). And current increased around 11-fold in the positive pulses when measured with electrodes of 100 μm spacings, while the DNA-AuNP hydrogel sample gave very asymmetric IV curves. These electrical measurements demonstrate that modification and organization of nanomaterials using DNA strands can be used to control the electrical behavior of the percolating networks and can change the conductivity of the composites by using DNA self-assembly to connect the nanomaterials.

Studies on conductivity of DNA mostly agree that DNA is not a good conductor and does not contribute to conductivity in the composites when conductive nanomaterials present^[209]. However, DNA has been seen has a good candidate to self-organize nanocircuits into a complex system. Therefore, besides mechanical reinforcement, another objective of integrating nanomaterials into the hydrogel composites is to modify the electrical behavior and add functionality to the hydrogels. For this reason, we used semiconducting SWNT when making DNA-SWNT conjugates. In the previous electrical studies of single SWNT on parallel gold electrodes^[222], the IV curves show a saturation of conductance at high voltages. We did not observe

such a saturation from IV characterization of SWNT networks from conjugates and hydrogels (Figure 5.16(a), Figure 5.17(a)).

Circuits built with AuNP have a lower conductivity compared to the ones created with CNT, since the nanosphere structure does not have the advantage in reaching long-range percolation like nanotubes of much greater aspect ratios do. For the same reason, adding spacers to DNA-AuNP conjugates also does not result in as much of an enhancement in conductivity. This result showed that the shape of nanomaterials needs to be considered when designing the hydrogels to ensure the assembled circuits have desired performance. Increased control of the architectural characteristics of percolation paths formed by CNT and AuNP (i.e., length-scale, clumpiness, subcircuit structures, etc.) will encourage further investigation of these embedded networks for potential applications in neuromorphic and error-tolerant computing.

5.6 Conclusions and future directions

We designed and built pure DNA hydrogels as well as composites using DNA/nanomaterial conjugates crosslinkers, DNA tiles crosslinkers, and linear DNA spacers. We characterized the nanomaterial networks in the composites and examined their mechanical and electrical behaviors. We found that shorter spacers form more solid-like hydrogels when combined with pure DNA crosslinkers while longer spacers construct more solid-like hydrogels when assembled with DNA/nanomaterial crosslinkers. We obtained hydrogel composites with significantly higher mechanical strength by combining DNA-CNT conjugates and up to 25% DNA tiles as crosslinkers. In addition, dried networks from both DNA-SWNT and DNA-AuNP hybrids show nonlinear electrical behaviors. By comparing the conductivities of dehydrated networks from conjugates and hydrogels, we showed the ability of DNA self-assembly in integrating and

connecting percolating networks with nanotubes and nanoparticles. These initial examples of biomolecular functionality by design suggest that the basic concepts of DNA self-assembly can effectively be used to create more complicated materials. Potentially, crosslinkers such as DNA-wrapped CNT can be used to create more sophisticated conjugates and nanostructures. We can design DNA to realize control in nanoelectronics morphology through connection and arrangement of nanomaterials.

These materials have potential for applications in 3D integrated circuits and hardware with shorter production time, lower cost, lower power consumption, and higher energy efficiency. Eventually, electronic hardware utilizing 3D integration and assembled using DNA nanotechnology may achieve computing capabilities in certain operations beyond the performance currently achieved by circuits fabricated using traditional lithography techniques. The nanocircuits created with our self-assembly approach can either be further deposited onto a silicon substrate or stored in the solution. Although further deposition onto a substrate will break the 3D structures and connections, it has the advantage of being less volatile. On the other hand, storing the constructed nanocircuits in the solution can retain the randomness and programmed structures, which may potentially allow them to serve better for unconventional computing research.

One future step of this project is to further investigate the influence of dimensions and aspect ratios of the nanomaterials integrated into the hydrogel system on the electrical and mechanical properties of the hydrogel. Besides nanotubes and nanoparticles, one can also study a different shape of nanomaterials such as nanosheets (example: silicon carbide nanosheets). It would also be interesting to see what will be the limitations on the dimensions of the materials that can be effectively integrated into a DNA-based hydrogel system. Another potential approach in the future is to design DNA to specifically connect onto certain locations of the nanomaterials to

realize the extremely precise control of crosslinked network. Besides, one can also introduce additional techniques to the mechanical and electrical measurements, such as using a Maxwell model to get the relaxation time, performing a temperature sweep, and conducting multi-terminal measurements on electrical characterization.

Bibliography

- [167] Winfree, E.; Liu, F.; Wenzler, L.A.; Seeman, N.C. Design and self-Assembly of Two-Dimensional DNA Crystals. *Nature* **1998**, *394*, 539-544; DOI:10.1038/28998.
- [168] Rothmund, P.W.K. Folding DNA to Create Nanoscale Shapes and Patterns. *Nature* **2006**, *440*, 297-302; DOI:10.1038/nature04586.
- [169] Douglas, S.M.; Dietz, H.; Liedl, T.; Högberg, B.; Graf, F.; Shih, W.M. Self-Assembly of DNA into Nanoscale Three-Dimensional Shapes. *Nature* **2009**, *459*, 414-418; DOI:10.1038/nature08016.
- [170] Marchi, A.N.; Saaem, I.; Vogen, B.N.; Brown, S.; LaBean, T.H. Toward Larger DNA Origami, *Nano Lett.* **2014**, *14*, 5740-5747; DOI:10.1021/nl502626s.
- [171] Wagenbauer, K.F.; Sigl, C.; Dietz, H. Gigadalton-Scale Shape-Programmable DNA Assemblies. *Nature* **2017**, *552*, 78-83. DOI:10.1038/nature24651.
- [172] Yan, H.; Park, S.H.; Finkelstein, G.; Reif, J.H.; LaBean, T.H. DNA-Templated Self-Assembly of Protein Arrays and Highly Conductive Nanowires. *Science* **2003**, *301*, 1882-1884; *JSTOR*, www.jstor.org/stable/3835179.
- [173] Knudsen, J.B.; Liu, L.; Bank Kodal, A.L.; Madsen, M.; Li, Q.; Song, J.; Woehrstein, J.B.; Wickham, S.F.J.; Strauss, M.T.; Schueder, F.; Vinther, J.; Krissanaprasit, A.; Gudnason, D.; Abbotsford Smith, A.A.; Ogaki, R.; Zelikin, A.N.; Besenbacher, F.; Birkedal, V.; Yin, P.; Shih, W.M.; Jungmann, R.; Dong, M.; Gothelf, K.V. Routing of Individual Polymers in Designed Patterns. *Nat. Nanotechnol.* **2015**, *10*, 892-898; DOI:10.1038/nnano.2015.190.
- [174] Krissanaprasit, A.; Madsen, M.; Knudsen, J.B.; Gudnason, D.; Surareungchai, W.; Birkedal, V.; Gothelf, K.V. Programmed Switching of Single Polymer Conformation on DNA Origami. *ACS Nano* **2016**, *10*, 2243-2250; DOI:10.1021/acsnano.5b06894.
- [175] Madsen, M.; Christensen, R.S.; Krissanaprasit, A.; Bakke, M.R.; Riber, C.F.; Nielsen, K.S.; Zelikin, A.N.; Gothelf, K.V. Preparation, Single-Molecule Manipulation, and Energy Transfer Investigation of a Polyfluorene-Graft-DNA Polymer. *Chem. Eur. J.* **2017**, *23*, 10511-10515; DOI:10.1002/chem.201702780.
- [176] Shahbazi, M.A.; Bauleth-Ramos, T.; Santos, H.A. DNA Hydrogel Assemblies: Bridging Synthesis Principles to Biomedical Applications. *Adv. Therap.* **2018**, *1*, 1800042; DOI:10.1002/adtp.201800042.
- [177] Li, F.; Lyu, D.; Liu, S.; Guo, W. DNA Hydrogels and Microgels for Biosensing and Biomedical Applications. *Adv. Mater.* **2020**, *32*, 1806538; DOI:10.1002/adma.201806538.

- [178] Lee, J.B.; Peng, S.; Yang, D.; Roh, Y.H.; Funabashi, H.; Park, N.; Rice, E.J.; Chen, L.; Long, R.; Wu, M.; Luo, D. A Mechanical Metamaterial Made from a DNA Hydrogel. *Nat. Nanotechnol.* **2012**, *7*, 816-820; DOI:10.1038/nnano.2012.211.
- [179] Liu, H.; Cao, T.; Xu, Y.; Dong, Y.; Liu, D. Tuning the Mechanical Properties of a DNA Hydrogel in Three Phases Based on ATP Aptamer. *Int. J. Mol. Sci.* **2018**, *19*, 1633. DOI:10.3390/ijms19061633.
- [180] Khajouei, S.; Ravan, H.; Ebrahimi, A. DNA Hydrogel-Empowered Biosensing. *Adv. Colloid Interface Sci.* **2020**, *275*, 102060; DOI:10.1016/j.cis.2019.102060.
- [181] Thelu, H.V.P.; Atchimnaidu, S.; Perumal, D.; Harikrishnan, K.S.; Vijayan, S.; Varghese, R. Self-Assembly of an Aptamer-Decorated, DNA-Protein Hybrid Nanogel: A Biocompatible Nanocarrier for Targeted Cancer Therapy. *ACS Appl. Bio Mater.* **2019**, *2*, 5227-5234; DOI:10.1021/acsabm.9b00323.
- [182] Eguchi, Y.; Kato, T.; Tanaka, T.; Maruyama, T. A DNA-Gold Nanoparticle Hybrid Hydrogel Network Prepared by Enzymatic Reaction. *Chem. Commun.* **2017**, *53*, 5802-5805; DOI:10.1039/C7CC02435E.
- [183] Gačanin, J.; Synatschke, C.V.; Weil, T. Biomedical Applications of DNA-Based Hydrogels. *Adv. Funct. Mater.* **2020**, *30*, 1906253; DOI:10.1002/adfm.201906253.
- [184] Cheng, E.; Xing, Y.; Chen, P.; Yang, Y.; Sun, Y.; Zhou, D.; Xu, L.; Fan, Q.; Liu, D. A pH-Triggered, Fast-Responding DNA Hydrogel. *Angew. Chem. Int.* **2009**, *48*, 7660-7663; DOI:10.1002/anie.200902538.
- [185] Li, C.; Faulkner-Jones, A.; Dun, A.R.; Jin, J.; Chen, P.; Xing, Y.; Yang, Z.; Li, Z.; Shu, W.; Liu, D.; Duncan, R.R. Rapid Formation of a Supramolecular Polypeptide-DNA Hydrogel for In Situ Three-Dimensional Multilayer Bioprinting. *Angew. Chem. Int.* **2015**, *54*, 3957-3961; DOI:10.1002/anie.201411383.
- [186] Zhou, D.; Ying, L.; Hong, X.; Hall, E.A.; Abell, C.; Klenerman, D. A Compact Functional Quantum Dot-DNA Conjugate: Preparation, Hybridization, and Specific Label-Free DNA Detection. *Langmuir* **2008**, *24*, 1659-1664; DOI:10.1021/la703583u.
- [187] Hurst, S.J.; Lytton-Jean, A.K.R.; Mirkin, C.A. Maximizing DNA Loading on a Range of Gold Nanoparticle Sizes. *Anal. Chem.* **2006**, *78*, 8313-8318; DOI:10.1021/ac0613582.
- [188] Li, Z.; Wu, Z.; Li, K. The High Dispersion of DNA-Multiwalled Carbon Nanotubes and Their Properties. *Anal. Biochem.* **2009**, *387*, 267-270; DOI:10.1016/j.ab.2009.01.043.
- [189] Hu, Y.; Domínguez, C.M.; Bauer, J.; Weigel, S.; Schipperges, A.; Oelschlaeger, C.; Willenbacher, N.; Keppler, S.; Bastmeyer, M.; Heißler, S.; Wöll, C.; Scharnweber, T.; Rabe, K.S.; Niemeyer, C.M. Carbon-Nanotube Reinforcement of DNA-Silica Nanocomposites Yields Programmable and Cell-Instructive Biocoatings. *Nat. Comm.* **2019**, *10*, 1-14; DOI:10.1038/s41467-019-13381-1.

- [190] Kyrylyuk, A.V.; Hermant, M.C.; Schilling, T.; Klumperman, B.; Koning, C.E.; van der Schoot, P. Controlling Electrical Percolation in Multicomponent Carbon Nanotube Dispersions. *Nat. Nanotechnol.* **2011**, *6*, 364–369; DOI:10.1038/nano.2011.40.
- [191] Vardharajula, S.; Ali, S.Z.; Tiwari, P.M.; Eroğlu, E.; Vig, K.; Dennis, V.A.; Singh, S.R. Functionalized Carbon Nanotubes: Biomedical Applications. *Int. J. Nanomedicine.* **2012**, *7*, 5361–5374; DOI:10.2147/IJN.S35832.
- [192] Nakashima, N.; Okuzono, S.; Murakami, H.; Nakai, T.; Yoshikawa, K. DNA Dissolves Single-Walled Carbon Nanotubes in Water. *Chem. Lett.* **2003**, *5*, 456-457; DOI:10.1246/cl.2003.456.
- [193] Zheng, M.; Jagota, A.; Semke, E.D.; Diner, B.A.; Mclean, R.S.; Lustig, S.R.; Richardson, R.E.; Tassi, N.G. DNA-Assisted Dispersion and Separation of Carbon Nanotubes. *Nat. Mater.* **2003**, *2*, 338-342. DOI:10.1038/nmat877.
- [194] Dovbeshko, G.I.; Repnytska, O.P.; Obraztsova, E.D.; Shtogun, Y.V. DNA Interaction with Single-Walled Carbon Nanotubes: A SEIRA Study. *Chem. Phys. Lett.* **2003**, *372*, 432-437; DOI:10.1016/S0009-2614(03)00429-9.
- [195] Chen, Y.; Liu, H.; Ye, T.; Kim, J.; Mao, C. DNA-Directed Assembly of Single-Wall Carbon Nanotubes. *J. Am. Chem. Soc.* **2007**, *129*, 8696-8697; DOI:10.1021/ja072838t.
- [196] Rueckes, T.; Kim, K.; Joselevich, E.; Tseng, G.Y.; Cheung, C.-L.; Lieber, C.M. Carbon Nanotube-Based Nonvolatile Random Access Memory for Molecular Computing. *Science* **2000**, *289*, 94-97; DOI:10.1126/science.289.5476.94.
- [197] Kang, J.W.; Lee, J.H.; Lee, H.J.; Hwang, H.J. A Study on Carbon Nanotube Bridge as a Electromechanical Memory Device. *Physica E Low Dimens. Syst. Nanostruct.* **2005**, *27*, 332-340; DOI:10.1016/j.physe.2004.12.009.
- [198] Giljohann, D.A.; Seferos, D.S.; Daniel, W.L.; Massich, M.D.; Patel, P.C.; Mirkin, C.A. Gold Nanoparticles for Biology and Medicine. *Angew. Chem. Int. Ed.* **2010**, *49*, 3280-3294; DOI:10.1002/anie.200904359.
- [199] Li, D.; Song, S.; Fan, C. Target-Responsive Structural Switching for Nucleic Acid-Based Sensors. *Acc. Chem. Res.* **2010**, *43*, 631-641; DOI:10.1021/ar900245u.
- [200] Lin, C.; Liu, Y.; Yan, H. Designer DNA Nanoarchitectures. *Biochemistry* **2009**, *48*, 1663-1674; DOI:10.1021/bi802324w.
- [201] Mirkin, C.A.; Letsinger, R.L.; Mucic, R.C.; Storhoff, J.J. A DNA-Based Method for Rationally Assembling Nanoparticles into Macroscopic Materials. *Nature* **1996**, *382*, 607–609; DOI:10.1038/382607a0.

- [202] Alivisatos, A.P.; Johnsson, K.P.; Peng, X.; Wilson, T.E.; Loweth, C.J.; Bruchez, M.P.; Schultz, P.G. Organization of 'Nanocrystal Molecules' Using DNA. *Nature* **1996**, *382*, 609–611; DOI:10.1038/382609a0.
- [203] Storhoff, J.J.; Elghanian, R.; Mirkin, C.A.; Letsinger, R.L. Sequence-Dependent Stability of DNA-Modified Gold Nanoparticles. *Langmuir* **2002**, *18*, 6666-6670; DOI:10.1021/la0202428.
- [204] Xing, Y.; Cheng, E.; Yang, Y.; Chen, P.; Zhang, T.; Sun, Y.; Yang, Z.; Liu, D. Self-Assembled DNA Hydrogels with Designable Thermal and Enzymatic Responsiveness. *Adv. Mater.* **2011**, *23*, 1117-1121; DOI:10.1002/adma.201003343.
- [205] Um, S.H.; Lee, J.B.; Park, N.; Kwon, S.Y.; Umbach, C.C., Luo, D. Enzyme-Catalysed Assembly of DNA Hydrogel. *Nat. Mater.* **2006**, *5*, 797-801; DOI:10.1038/nmat1741.
- [206] Zadeh, J. N.; Steenberg, C. D.; Bois, J. S.; Wolfe, B. R.; Pierce, M. B.; Khan, A. R.; Dirks, R. M.; Pierce, N. A. NUPACK: Analysis and Design of Nucleic Acid Systems. *J. Comput. Chem.* **2011**, *32*, 170–173; DOI:10.1002/jcc.21596.
- [207] Cheng, E.; Li, Y.; Yang, Z.; Deng, Z.; Liu, D. DNA-SWNT Hybrid Hydrogel. *Chem. Commun.* **2011**, *47*, 5545-5547; DOI:10.1039/c1cc11028d.
- [208] Zheng, M.; Jagota, A.; Strano, M.S.; Santos, A.P.; Barone, P.; Chou, S.G.; Diner, B.A.; Dresselhaus, M.S., Mclean, R.S.; Onoa, G.B.; Samsonidze, G.G.; Semke, E.D.; Usrey, M.; Walls, D.J. Structure-Based Carbon Nanotube Sorting by Sequence-Dependent DNA Assembly. *Science* **2003**, *302*, 1545-1548; *JSTOR*, www.jstor.org/stable/3835781.
- [209] Lahiji, R.R.; Dolash, D.D.; Bergstrom, D.E.; Reifengerger, R. Oligodeoxyribonucleotide Association with Single-Walled Carbon Nanotubes Studied by SPM. *Small* **2007**, *3*, 1912-1920; DOI:10.1002/sml.200700184.
- [210] Yang, Q.-H.; Wang, Q.; Gale, N.; Oton, C.J.; Cui, L.; Nandhakumar, I.S.; Zhu, Z.; Tang, Z.; Brown, T.; Loh, W.H. Loosening the DNA Wrapping Around Single-Walled Carbon Nanotubes by Increasing the Strand Length. *Nanotechnology* **2009**, *20*, 195603; DOI:10.1088/0957-4484/20/19/195603.
- [211] Hill, H.D.; Mirkin, C.A. The Bio-Barcode Assay for the Detection of Protein and Nucleic Acid Targets using DTT-Induced Ligand Exchange. *Nat. Protoc.* **2006**, *1*, 324-36. DOI:10.1038/nprot.2006.51.
- [212] Haiss, W.; Thanh, N.T.K.; Aveyard, J.; Fernig, D.G. Determination of Size and Concentration of Gold Nanoparticles from UV-Vis Spectra. *Anal. Chem.* **2007**, *79*, 4215-4221; DOI:10.1021/ac0702084.
- [213] Zhang, X.; Liu, B.; Dave, N.; Servos, M.R.; Liu, J. Instantaneous Attachment of an Ultrahigh Density of Nonthiolated DNA to Gold Nanoparticles and Its Applications. *Langmuir* **2012**, *28*, 17053-17060; DOI:10.1021/la3035424.

- [214] Pellegrino, T.; Sperling, R.A.; Alivisatos, A.P.; Parak, W.J. Gel Electrophoresis of Gold-DNA Nanoconjugates. *J. Biomed. Biotechnol.* **2007**, *2007*, 26796; DOI:10.1155/2007/2679.
- [215] Li, F.; Tang, J.; Geng, J.; Luo, D.; Yang, D. Polymeric DNA Hydrogel: Design, Synthesis and Applications. *Prog. Polym. Sci.* **2019**, *98*, 101163; DOI:10.1016/j.progpolymsci.2019.101163.
- [216] Nöll, T.; Schönherr, H.; Wesner, D.; Schopferer, M.; Paululat, T.; Nöll, G. Construction of Three-Dimensional DNA Hydrogels from Linear Building Blocks. *Angew. Chem. Int. Ed.* **2014**, *53*, 8328-8332; DOI:10.1002/anie.201402497.
- [217] Jiang, H.; Pan, V.; Vivek, S.; Weeks, E.R.; Ke, Y. Programmable DNA Hydrogels Assembled from Multidomain DNA Strands. *Chem. Bio. Chem.* **2016**, *17*, 1156-1162; DOI:10.1002/cbic.201500686.
- [218] Campbell, J.F.; Tessmer, I.; Thorp, H.H.; Erie, D.A. Atomic Force Microscopy Studies of DNA-Wrapped Carbon Nanotube Structure and Binding to Quantum Dots. *J. Am. Chem. Soc.* **2008**, *130*, 10648-10655. DOI:10.1021/ja801720c.
- [219] Crocker, J.C.; Grier, D.G. Methods of Digital Video Microscopy for Colloidal Studies. *J. Colloid Interface Sci.* **1996**, *179*, 298-310. DOI:10.1006/jcis.1996.0217.
- [220] Oelschlaeger, C.; Bossler, F.; Willenbacher, N. Synthesis, Structural and Micromechanical Properties of 3D Hyaluronic Acid-Based Cryogel Scaffolds. *Biomacromolecules.* **2016**, *17*, 580-589; DOI:10.1021/acs.biomac.5b01529.
- [221] Allan, D.B.; Caswell, T.; Keim, N.C.; van der Wel, C.M. Trackpy: Trackpy v0.4.1. *Zenodo*, **2018**, DOI:10.5281/zenodo.1226458.
- [222] Gómez-Navarro, C.; De Pablo, P.J.; Gómez-Herrero, J. Electrical Properties of Long Molecules: Single-Walled Carbon Nanotubes and DNA. *Int. J. Nanotechnol.* **2005**, *2*, 90-102; DOI:10.1504/IJNT.2005.006976.